The First Results of Observations of the Transient Pulsar SAX J2103.5+4545 by the INTEGRAL Observatory

A. A. Lutovinov[1,2]*, S. V. Molkov[1], and M. G. Revnivtsev[1,2]

[1]*Space Research Institute, Russian Academy of Sciences, Profsoyuznaya ul. 84/32, Moscow, 117810 Russia*
[2]*Max-Planck-Institut für Astrophysik, Karl-Schwarzschild-Str. 1, Postfach 1317, D-85741 Garching, Germany*
Received May 8, 2003

Abstract—We present the preliminary results of our analysis of the observations of the X-ray pulsar SAX J2103.5+4545 by the INTEGRAL Observatory in December 2002. We mapped this region of the sky in a wide energy range, from 3 to 200 keV. The detection of the source is shown to be significant up to energies of ∼100 keV. The hard X-ray flux in the energy range 15−100 keV is variable and presumably depends on the orbital phase. We show that the shape of the pulsar spectrum and its parameters derived from 18−150-keV IBIS data are compatible with the RXTE observations of the source. © 2003 MAIK "Nauka/Interperiodica".

Key words: *pulsars, neutron stars, and X-ray sources.*

INTRODUCTION

The transient X-ray pulsar SAX J2103.5+4545 was discovered by the BeppoSAX observatory during its outburst of 1997 (Hulleman *et al.* 1998). The RXTE observations of the source during the next outburst in 1999 showed that, apart from a pulsation period of ∼358 s associated with the neutron star's rotation, the system has another type of periodicity attributable to the orbital motion of a compact object. Based on these observations, Baykal *et al.* (2000) found that the pulsar is a member of a binary system; its companion, the compact object ($e \simeq 0.4$), has a highly elliptical orbit with a period of ∼12$^{\rm d}$68.

The source's spectrum, described by a simple power law with a slope of ∼1.3 and a cutoff at high energies (Hulleman *et al.* 1998; Baykal *et al.* 2002), is typical of X-ray pulsars. Furthermore, it exhibits a fluorescent iron line at ∼6.4 keV, while the spectrum itself is modified in the soft energy range by interstellar absorption with an atomic hydrogen column density of $N_{\rm H} = 3.8 \times 10^{22}$ atoms cm^{-2}.

Analysis of the light curves for the source shows that its intensity is highly variable within one orbital cycle and peaks near the periastron (Baykal *et al.* 2000). Such behavior of light curves is typical of binary systems with relatively high eccentricities and high-mass companions, early-type (O−B) stars. However, despite the assumption made by Hulleman *et al.* (1998) that the B-type star HD 200709 is a possible companion, it has not yet been confirmed.

It should be noted that, despite the observed variability of the pulsar, both on time scales of the orbital cycle and on time scales of several hundred days, its spectral parameters are relatively stable (Baykal *et al.* 2002). This stability makes it possible to compare RXTE results with the results obtained by other observatories, in particular, by the INTEGRAL observatory.

According to observations with the All-Sky Monitor (ASM) of the RXTE observatory, the source has been relatively bright in recent years, continuing to show outburst activity. Interestingly, in the last several months, the constant component of this radiation had a clear tendency to increase. Here, based on publicly accessible observations of the INTEGRAL observatory, we study the hard radiation from the pulsar SAX J2103.5+4545.

ANALYSIS OF THE OBSERVATIONS

INTEGRAL. The INTEGRAL international gamma-ray observatory was launched into a high-apogee orbit by a Russian PROTON rocket from the Baikonur cosmodrome on October 17, 2002. It includes instruments to study cosmic sources over a wide energy range of 3−10 000 keV: (1) the IBIS telescope, which consists of two detectors, the ISGRI and the PICSIT, sensitive to photons in the energy ranges 15−200 and 170−10 000 keV, respectively, and which allows sources to be localized with an accuracy up to 30 arcsec; (2) the SPI spectrometer, which operates in the energy range 15−8000 keV

*E-mail: `aal@hea.iki.rssi.ru`

and is designed for fine spectroscopy with an energy resolution of $E/\delta E \simeq 500$ (at 1 MeV); and (3) the JEM-X X-ray monitor with an operating energy range of 3−35 keV. All of the INTEGRAL telescopes operate on the principle of a coded aperture. The fields of view of the IBIS and JEM-X telescopes, whose data were used here, are as follows: for IBIS, the total field of view is $29° \times 29°$, and the fully coded field is $9° \times 9°$; for JEM-X, the fully coded field is $4°.8$ in diameter. The observatory, its instruments, and the observing techniques were discussed in detail by Winkler (1996, 1999).

In this paper, we used the publicly accessible calibration observations of the Cyg X-1 region performed by INTEGRAL in December 2002 (revolutions 23 and 25, intervals UT 2002-12-21 09:14:29 − 2002-12-23 20:41:11 and UT 2002-12-28 11:53:17−2002-12-29 21:42:10, respectively). Since the calibration of the INTEGRAL instruments has not yet been finished, we cannot perform a comprehensive analysis of the data from all instruments. Therefore, in the subsequent analysis, we focus our attention on the data from the ISGRI detector of the IBIS telescope, which has the largest effective area. The data from the JEM-X monitor were used only for imaging in the soft energy range.

To analyze the data, we used the standard IDAS 1.0 software package that was put at our disposal by the INTEGRAL Science Data Center (ISDC, http://isdc.unige.ch). Version 1.0 of the IDAS package does not allow us to perform a spectral and temporal analysis of the source's radiation in full. Therefore, for a preliminary spectral analysis of the data obtained for the pulsar SAX J2103.5+4545, we used a large set of observations for the Crab Nebula in February 2003 (revolutions 39−45). Taking into account the strong dependence of the recorded count rate of sources (including the Crab Nebula) on their position on the detector (especially in the low-energy ISGRI channels), in the subsequent analysis of the light curves and spectra, we used only the observations in which the source SAX J2103.5+4545 was inside the fully coded IBIS field, where the recorded flux from the Crab Nebula is relatively constant (below, we took it to be 150 and 147 counts s^{-1} in the energy ranges 15−40 and 40−100 keV, respectively). Only the images of the region containing the pulsar that were constructed from the complete series of observations in the above periods constitute an exception. Thus, the usable time for ISGRI imaging was ∼260 ks; for temporal and spectral analyses, it was ∼55 ks. It should be noted that because of the much smaller field of view of the JEM-X monitor, its total exposure time during the observation of the pulsar SAX J2103.5+4545 was close to the latter value.

RXTE. To compare the INTEGRAL spectra with previous observations of the pulsar SAX J2103.5+4545, we used data from the RXTE observatory (Bradt *et al.* 1993), which repeatedly observed this source in 1997−2002. In addition, to analyze the behavior of the pulsar in the soft X-ray (1.3−12 keV) energy range during the INTEGRAL observations, we also used observations from the All-Sky Monitor (ASM) of the RXTE observatory (http://xte.mit.edu/ASM_lc.html).

The main instruments of the RXTE observatory are the PCA and HEXTE spectrometers, which jointly cover the energy range 3−250 keV. The PCA spectrometer is a system of five proportional gas (xenon/methane) counters. The PCA field of view is limited by a collimator with a transmission radius of 1°. The PCA working range is 3−20 keV, the effective area at energies of 6−7 keV is ∼6400 cm², and the energy resolution at these energies is ∼18%. The HEXTE spectrometer is a system of two independent packages of four NaI(Tl)/CsI(Na) phoswich detectors sweeping with an interval of 16 s for the observation of background areas at distances of 1°.5 from the source. At any given time, the source can be observed only by one of the two detector packages; thus, the effective area of the HEXTE detectors is ∼700 cm². The working energy range of the spectrometer is ∼15−250 keV.

To construct an average spectrum of the source from the RXTE data, we used ∼190 observations carried out during 1997−2000. The effective exposure time of the observations used is ∼560 ks. Since the shape of the source's spectrum changes only slightly with its flux (see Baykal *et al.* 2002), we averaged all of the observational data.

To process the RXTE data, we used the standard FTOOLS/LHEASOFT 5.2 software package.

RESULTS
Sky Maps

Figure 1 shows the maps of the sky containing the pulsar SAX J2103.5+4545 that were obtained by the JEM-X monitor and the ISGRI detector of the IBIS telescope in the energy ranges 3−10, 15−40, 40−100, and 100−200 keV, respectively. We clearly see from these maps that the source is significantly detected up to energies of ∼100 keV. Apart from the object under study, three known sources of this region of the sky fell within the IBIS field of view during the observations, and were significantly detected: the black-hole candidate Cyg X-1, the low-mass binary system Cyg X-2, and the binary system Cyg X-3 (the latter also fell within the JEM-X field of view). Note that Cyg X-1 and Cyg X-3 remain fairly bright even in the hardest energy range.
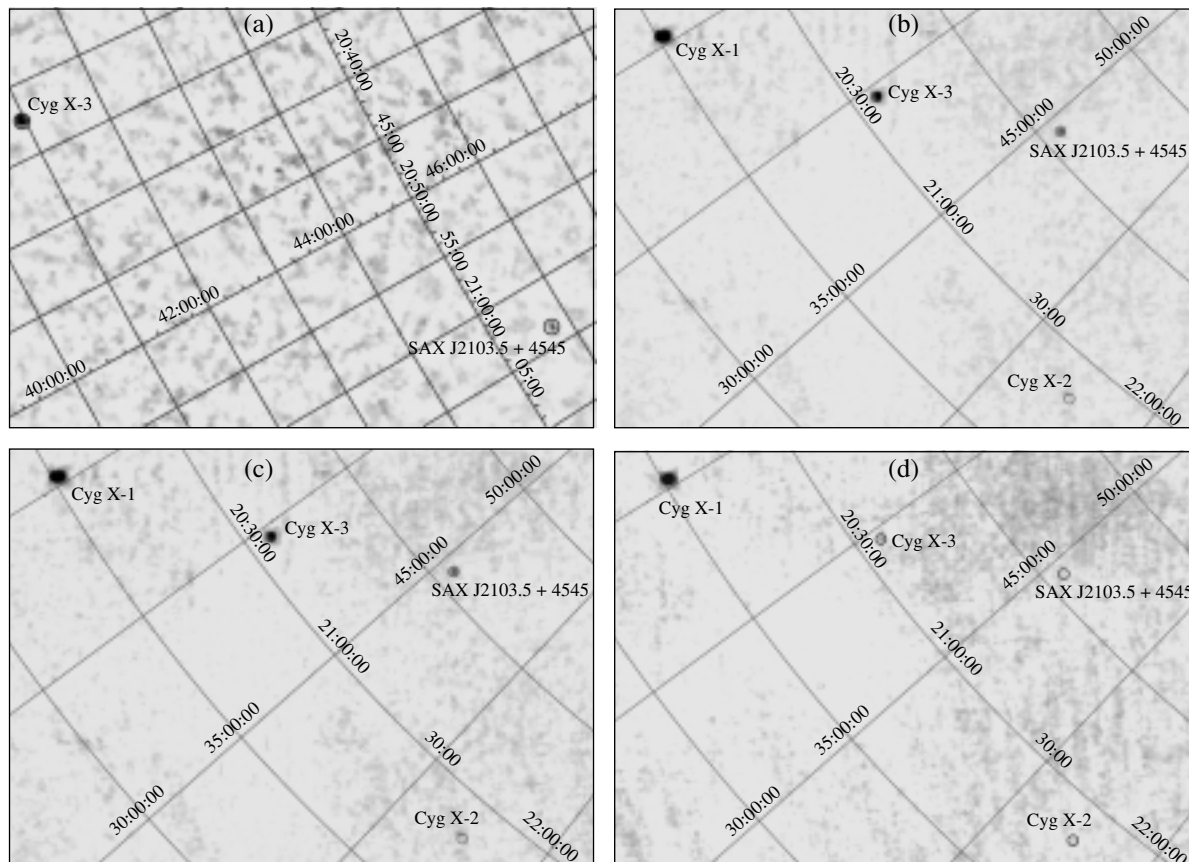
Fig. 1. Image of the sky region with the pulsar SAX J2103.5+4545, reconstructed from the INTEGRAL observations in December 2002: (a) the JEM-X image in the energy range 3−10 keV; (b, c ,d) the IBIS images in the energy ranges 15−40, 40−100, and 100−200 keV, respectively.

The Light Curves

As was noted in the Introduction, the pulsar's intensity strongly depends on the orbital phase, peaking near the periastron (Baykal *et al.* 2000). The INTEGRAL observations of the source indicate that a similar pattern is found in the hard X-ray and gamma-ray ranges. Figure 2 shows the IBIS light curves of the pulsar in the energy ranges 15−40 and 40−100 keV, which we arbitrarily call the hard X-ray and gamma-ray ranges, respectively. To more easily compare our light curves with those from Baykal *et al.* (2000), we plotted orbital phases along the horizontal axis together with time (the binary parameters were taken from the same paper). We see that the observed flux from the system in both energy ranges is at a maximum (∼60 and ∼30−40 mCrab, respectively) near an orbital phase of 0.5; subsequently, it begins to decline, reaches ∼10−20 mCrab in the energy range 15−40 keV, and falls almost to zero in the energy range 40−100 keV at phases 0.1−0.2. Unfortunately, we could not record the light curve of the pulsar in more detail during the complete orbital cycle, because

INTEGRAL performed calibration observations of empty fields between December 23 and 28, 2002.

The Spectrum

To characterize the spectrum of SAX J2103.5+ 4545, we used the ratio of the source's fluxes measured in different energy ranges to the fluxes recorded by the ISGRI detector of the IBIS telescope from the Crab Nebula in the same energy ranges. Analysis of the set of observations for the Crab Nebula shows that this method of studying sources allows the shapes of their spectra to be roughly estimated. In this case, however, because of the imperfect first calibrations of the instrument, the various systematic uncertainties are of great importance. The observed amplitude of the systematic uncertainties in determining the source's flux in different energy ranges can reach 10−20%. It is important to note that, as was said above, both in the observations of the source under study and in the calibration observations of the Crab Nebula, we used only the observations in which the sources were within the fully coded field of the telescope.
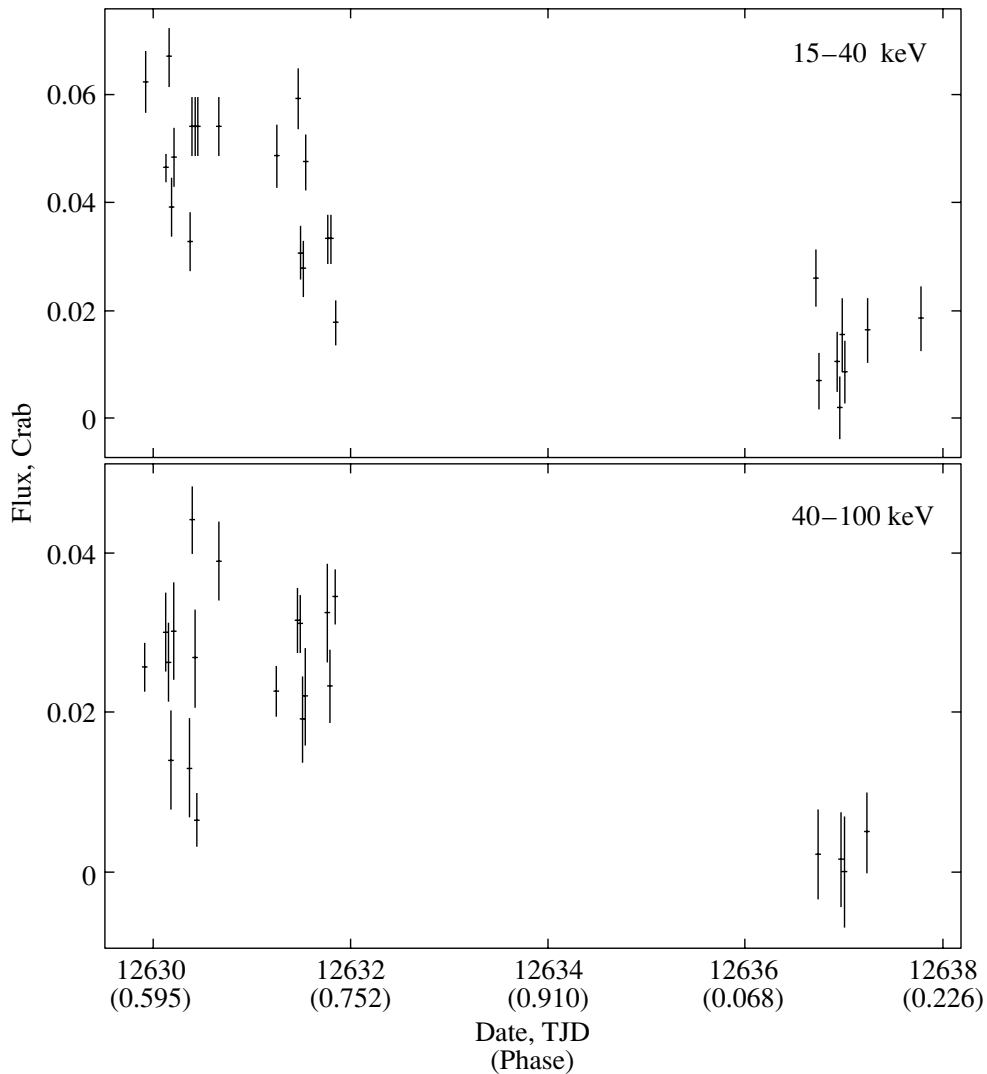
Fig. 2. The ISGRI light curves of the pulsar SAX J2103.5+4545 in the energy ranges 15−40 and 40−100 keV. Each point corresponds to one telescope pointing with a characteristic exposure time of ∼2200 s.

Using the known shape of the spectrum for the Crab Nebula, we can recalculate the flux from the source concerned to units of photons cm^{-2} s^{-1} in each energy range and then fit the spectrum obtained by various models. The ratio of the spectrum for the pulsar SAX J2103.5+4545 to the spectrum for the Crab Nebula is shown in Fig. 3. Because of the complexity of the described procedure and its large systematic uncertainties, the χ^2 value for these fits cannot be considered an adequate characteristic of the quality of the applied model.

To describe the spectrum of the source, we used two simple models: a simple power-law energy dependence of the photon flux $(dN/dE \propto E^{-\Gamma})$ and a power-law energy dependence of the photon flux with an exponential cutoff $(dN/dE \propto E^{-\Gamma} \exp(-(E -$

$E_{cut})/E_{fold}))$, which is a typical model for the spectra of accreting X-ray pulsars. The latter model fit was successfully used to describe the broadband spectrum of the source SAX J2103.5+4545 during its outbursts in 1997 and 1999 (Baykal *et al.* 2002).

The best-fit parameters of the source's spectrum for the models described above are given in the table. It should be noted that, when fitting the spectrum, we included the systematic uncertainties in the source's fluxes in different energy channels at a 15% level. Since no information about the source's spectrum at energies below 18 keV is available, we fixed several parameters pertaining to this energy range at the values obtained by the RXTE observatory during the bright state of SAX J2103.5+4545 (Baykal *et al.* 2002). The spectrum of the source obtained
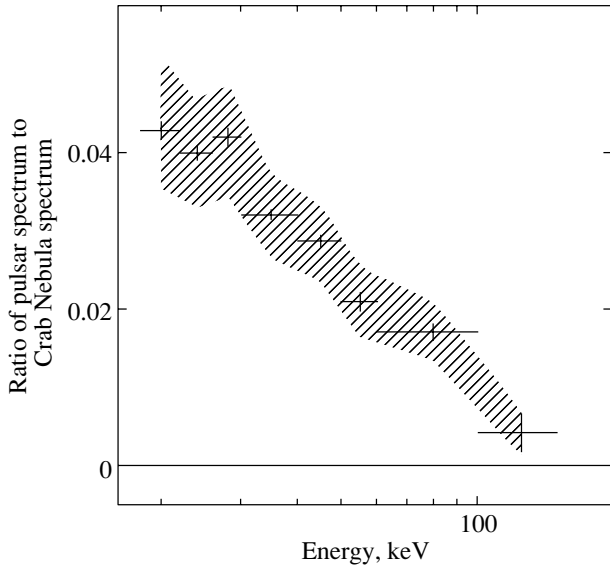
Fig. 3. The ratio of the spectrum of the pulsar SAX J2103.5+4545 to the spectrum of the Crab Nebula (IBIS data). The hatched region indicates the domain of possible (statistical and systematic) uncertainties in the values obtained.
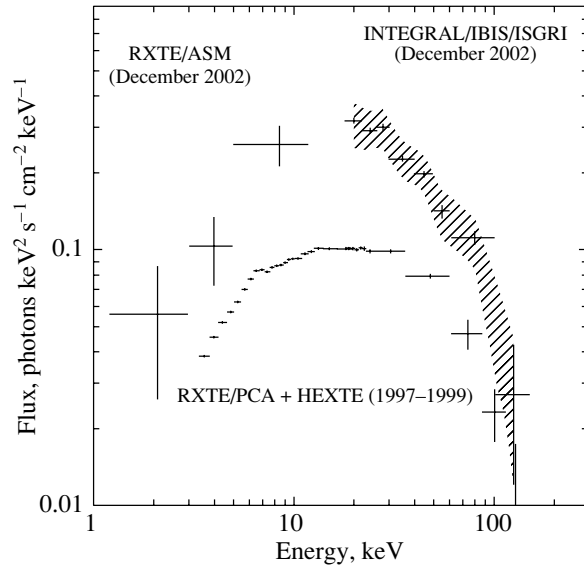

Fig. 4. The INTEGRAL and RXTE spectra of the X-ray pulsar SAX J2103.5+4545 (the normalization of the RXTE spectrum is arbitrary). The hatched region around the IBIS spectrum indicates the domain of possible (statistical and systematic) uncertainties in the values obtained. The IBIS spectrum was supplemented below 15 keV with the simultaneous ASM/RXTE observations.

from the ISGRI data of the IBIS telescope is shown in Fig. 4. To extend it to energies below 15 keV, we used the simultaneous ASM observations in three energy channels.

To compare our results with the archival observa-

tions of the pulsar SAX J2103.5+4545, Fig. 4 also shows the source's typical spectrum in its bright state (PCA and HEXTE data of the RXTE observatory, arbitrary normalization of the spectrum). We see that our spectrum construction technique allows us to satisfactorily restore the spectrum of the source under study from the IBIS data. In this case, its best-fit parameters, particularly, the exponential spectral cutoff parameter, agree well with the RXTE results.

Best-fit parameters for the spectrum of the pulsar SAX J2103.5+4545, as derived from IBIS (18−150 keV) data

Power law ($dN/dE \propto E^{-\Gamma}$)	
Photon index Γ	2.8 ± 0.3
Flux, 18−150 keV, 10^{-10} erg cm^{-2} s^{-1}	6.2
χ^2(d.o.f.)	12.2(6)
$dN/dE \propto E^{-\Gamma} \exp(-(E - E_{cut})/E_{fold})$	
Photon index Γ	1.3[a]
Cutoff energy E_{cut}, keV	7.8[a]
Spectral cutoff parameter E_{fold}, keV	26 ± 1
Flux, 18−150 keV, 10^{-10} erg cm^{-2} s^{-1}	5.7
χ^2(d.o.f.)	5.2(6)

[a] Since no spectral information is available at energies below 18 keV, the parameters pertaining to this energy range were fixed at the values given by Baykal *et al.* (2002).

CONCLUSIONS

The transient pulsar SAX J2103.5+4545 fell within the INTEGRAL field of view during the calibration observations of the Cyg X-1 region in December 2002. Our analysis has shown that the source is detected by the IBIS telescope up to energies of ∼100 keV; the shape of the source's spectrum derived from the INTEGRAL data agrees well with the its RXTE observations. The spectrum of the pulsar in the energy range 18−100 keV can be described either by a power law with a slope of ∼2.8 or by a power-law energy dependence of the photon flux with an exponential cutoff, which was used to fit the RXTE spectrum of the source. The spectral cutoff parameter $E_{fold} = 26 \pm 1$ keV agrees well with the RXTE results, $E_{fold} = 27.1 \pm 0.9$ keV (Baykal *et al.* 2002).

Despite the moderately long exposure time of the source's observations (less than half of the orbital cycle was covered), we managed to restore the light curve of the source and to show that its flux in the energy range 15−100 keV is variable. The flux from the source both at soft energies (ASM/RXTE) and at hard energies (INTEGRAL/IBIS) probably peaks near the periastron.

Including the INTEGRAL observations of the pulsar SAX J2103.5+4545 obtained during regular scanning of the Galactic plane in the subsequent analysis will allow us to increase the usable observing time, to cover more completely the orbital cycle, and to search for the cyclotron feature in the spectrum of the source. The latter, according to the estimates by Baykal *et al.* (2002), must be at ∼140 keV, which corresponds to a neutron-star surface magnetic field of 1.2×10^{13} G.

ACKNOWLEDGMENTS

REFERENCES

1. A. Baykal, M. Stark, and J. Swank, Astrophys. J. Lett. **544**, L129 (2000).

2. A. Baykal, M. Stark, and J. Swank, Astrophys. J. **569**, 903 (2002).

3. H. Bradt, R. Rothschild, and J. Swank, Astron. Astrophys., Suppl. Ser. **97**, 355 (1993).

4. F. Hulleman, J. in't Zand, and J. Heise, Astron. Astrophys. **337**, L25 (1998).

5. C. Winkler, Astron. Astrophys., Suppl. Ser. **120**, 637 (1996).

6. C. Winkler, Astrophys. Lett. Comm. **39**, 309 (1999).

Translated by G. Rudnitskiĭ

RXTE Observations of the Transient Sources IGR J17091−3624 and IGR J18539+0727

A. A. Lutovinov[1,2*] and M. G. Revnivtsev[1,2]

[1]*Space Research Institute, Russian Academy of Sciences, Profsoyuznaya ul. 84/32, Moscow, 117810 Russia*
[2]*Max-Planck-Institut für Astrophysik, Karl-Schwarzschild-Str. 1, Postfach 1317, D-85741 Garching, Germany*
Received June 9, 2003

Abstract—We present the results of our analysis of the RXTE observations for two transient sources, IGR J17091−3624 and IGR J18539+0727, in April 2003. The derived energy spectra of the sources and the power-density spectra of their light curves make it possible to classify them as low/hard-state X-ray binaries. The parameters of the power spectrum for IGR J18539+0727 lead us to tentatively conclude that the compact object in this binary is a black hole. © 2003 MAIK "Nauka/Interperiodica".

Key words: *transient sources, black holes.*

INTRODUCTION

The sources IGR J17091−3624 and IGR J18539+0727 were discovered by the INTEGRAL observatory during a deep survey of the central radian of the Galaxy and regular scanning of the Galactic plane in April 2003 (Kuulkers *et al.* 2003; Lutovinov *et al.* 2003a).

The first source was detected on April 14 by the IBIS telescope of the INTEGRAL observatory in the energy range 40−100 keV with a flux of 20 mCrab. In the softer energy range 15−40 keV, the upper limit on the X-ray flux was 10 mCrab. The subsequent observations of this region of the sky on April 15−16 showed that the source's flux increased to 40 and 25 mCrab in the energy ranges 15−40 and 40−100 keV, respectively, suggesting a possible softening of the source's spectrum (Kuulkers *et al.* 2003). Analysis of archival data from the TTM telescope of the Roentgen observatory on the Kvant module of the Mir orbiting station and the WFC telescope of the BeppoSAX observatory showed that during 1994−2001, the source was significantly detected at the same position several times (Revnivtsev *et al.* 2003; J. in't Zand *et al.* 2003). VLA radio observations of the sky region around the source after the discovery of IGR J17091−3624 in April 2003 (Rupen *et al.* 2003) revealed a possible radio counterpart.

Several days later, on April 17−18, the second source was discovered during regular scanning of the Galactic plane and deep observations of the microquasar GRS 1915+105. The observed flux from it was 20 mCrab in the energy ranges 15−40 and 40−100 keV (Lutovinov *et al.* 2003a). To try to understand the nature of the newly discovered sources, they were almost immediately observed from the RXTE observatory, which has high sensitivity in the soft energy range (3−20 keV) and large capabilities for spectral and temporal analyses of the objects under study. In this paper, we present the results of these observations.

ANALYSIS OF THE OBSERVATIONS AND RESULTS

The sources IGR J17091−3624 and IGR J18539+0727 were observed by the RXTE observatory (Bradt *et al.* 1993) on April 20.5 and 26.1, 2003, respectively. The effective exposure time of the observations was 2 and 3.2 ks, respectively. The RXTE/PCA data were processed by using the standard FTOOLS/ LHEASOFT 5.2 software package. The L7_240 model was used to simulate the RXTE/PCA instrumental background. To increase the sensitivity at energies above 10−15 keV, we used the data from all the PCA anode layers in our analysis. Since the sources are faint, they are not detectable by the HEXTE spectrometer (15−250 keV). The standard XSPEC package (http://xspec.gsfc.nasa.gov) was used for spectral fitting.

The PCA spectrometer collects X-ray photons from an area of 1 square degree without being able to distinguish background X-ray photons from photons of the source proper. When studying sources located in the Galactic plane, the Galactic ridge emission can significantly contribute to the observed
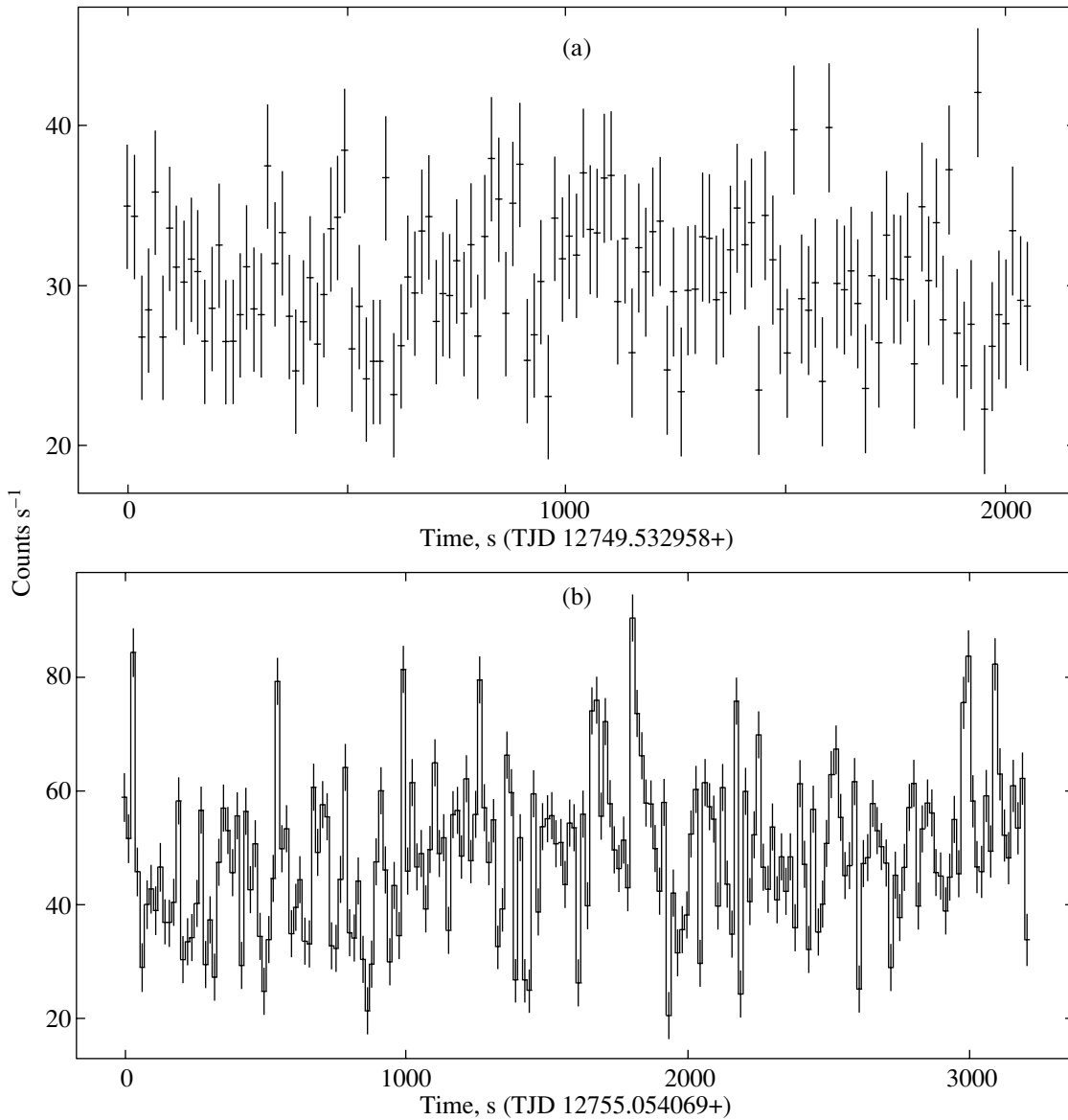
---

*E-mail: aal@hea.iki.rssi.ru

Fig. 1. The RXTE 3−20-keV light curves of the sources (a) IGR J17091−3624 and (b) IGR J18539+0727. Each point corresponds to a time bin of 16 s. The estimated contribution of the Galactic ridge emission was subtracted. Time, in seconds from the beginning of the observation (given for each observation in TJD), is along the horizontal axis.

flux. In the Galactic-center region, at a Galactic latitude of ∼2°, where the source IGR J17091−3624 is located, the flux of the Galactic ridge emission within the PCA field of view is ∼0.5-0.6 mCrab in the energy range 3−20 keV (see Valinia and Marshall 1998; Revnivtsev 2003). The observed flux from IGR J17091−3624 in the same energy range is ∼4 mCrab; i.e., it is only a factor of ∼8 higher than the background flux from the Galactic ridge. Therefore, we should be very cautious when performing the spectral analysis and take into account the contribution from the emission lines that are present in the background spectrum to the observed spectrum of the source. At an angular distance of

∼40° from the Galactic center, at which the source IGR J18539+0727 is located, the contribution of the Galactic ridge emission is much smaller (∼2−5% of the source's flux).

IGR J17091−3624. The light curve of the source for the entire observation of April 20, 2003, is shown in Fig. 1a. As follows from this figure, its intensity throughout the observation was relatively constant at a level of ∼4 mCrab (the contribution from the Galactic ridge emission to the RXTE/PCA flux was subtracted). Since the source is faint, the uncertainty in its fractional rms is large: the fractional rms in the 0.01−10-Hz frequency band measured from the
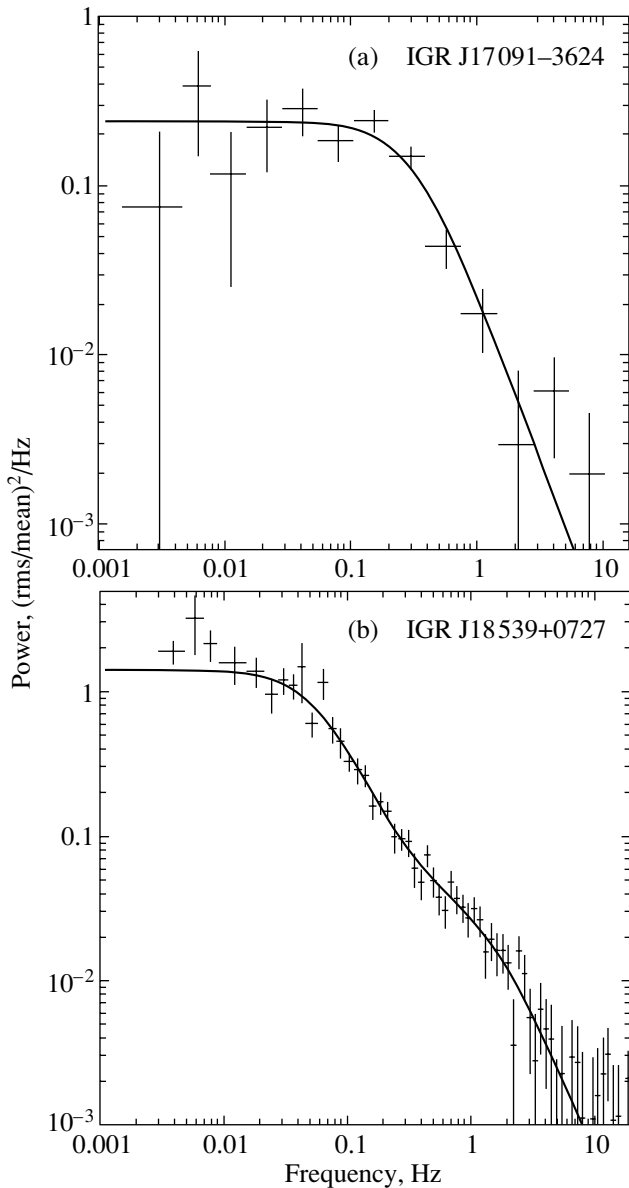
Fig. 2. The power-density spectra of (a) IGR J17091−3624 and (b) IGR J18539+0727. The solid lines represent band-limited noise model fits. One- and two-component models were used for IGR J17091−3624 and IGR J18539+0727, respectively.

Fig. 3. (a) The spectrum of IGR J17091−3624. The dots with error bars (1σ) indicate the observed spectrum; the solid curve represents the model of the observed RXTE/PCA spectrum contributed by the source proper and the model of the ridge emission background (dashed curve). (b) The spectrum of IGR J18539+0727. The dots with error bars (1σ) indicate the observed spectrum; the solid curve represents the best-fit model. The ridge emission background was disregarded, because its contribution was small.

light curve is $27 \pm 3\%$ (when calculating the rms, we corrected it for the contribution of the Galactic ridge emission to the RXTE/PCA flux). In the power-density spectrum (Fig. 2a), we found no features associated with quasi-periodic flux oscillations, and, in general, it is well described by the standard model of band-limited noise commonly observed in X-ray binary systems in the low/hard spectral state (see, e.g., Sunyaev and Revnivtsev, 2000). When the power-density spectrum is described by a function of the form $dP \propto 1/(1 + (f/f_0)^2)df$, the derived characteristic cutoff frequency is $f_0 = 0.31 \pm 0.04$ Hz.

Figure 3a presents the energy spectrum of the source IGR J17091−3624 averaged over the whole observation, in units of keV^2 s^{-1} cm^{-2} keV^{-1}. The solid line indicates the model power-law energy dependence of the photon flux ($dN/dE \propto E^{-\Gamma}$) with the iron emission line at 6.4 keV that best fits the data obtained. The dashed line illustrates the estimated contribution of the Galactic ridge emission based on the measurements by Revnivtsev (2003). As we see from Fig. 3a, the relatively large contribution of the

Galactic ridge emission to the PCA spectrum does not allow us to reliably measure the parameters of the observed emission line. It may completely owe its origin to the effect of background photons. The spectral best-fit parameters are given in the table.

IGR J18539+0727. The light curve of the source IGR J18539+0727 in the energy range 3−20 keV is shown in Fig. 1b. This source is brighter than the above source, and its large aperiodic flux variability is clearly seen. For clarity, we connected the points in the figure by a histogram.

Figure 2b shows the power-density spectrum of the light curve for the source. As in IGR J17091−3624, it can be well fitted by the standard model used to describe the variability of X-ray binary systems in the hard/low spectral state. The higher sensitivity compared to IGR J17091−3624 allowed us to detect a second band-limited noise component. Fitting these two components by a model of the form $dP_{1,2} \propto 1/(1 + (f/f_{1,2})^2)df$ yields the cutoff frequencies $f_1 = (5.3 \pm 0.5) \times 10^{-2}$ Hz and $f_2 = 1.3 \pm 0.2$ Hz. The fractional rms attributable to the low- and high-frequency components is ∼39% and ∼46%, respectively. The total rms of the source in the broad frequency range 0.005−20 Hz is $45 \pm 2\%$.

Figure 3b presents the energy spectrum of the source averaged over all observations. Since IGR J18539+0727 is much farther from the Galactic center than IGR J17091−3624 and lies more than half a degree further from the Galactic plane, the contribution of the Galactic ridge emission to the total PCA flux is insignificant. As was said above, it is ∼2−5% of the total flux. To fit the spectrum of the source, we used the same model as in the previous case: a power-law decrease of the photon flux density modified by neutral photoabsorption at low energies. The presence of an emission (fluorescent) line in the spectrum may be due to the reflection of the hard X-radiation of inner accretion-flow regions from an optically thick, cold accretion disk (see, e.g., Basko *et al.* 1974). However, since the source is faint and the exposure time of the observations being analyzed is short, our sensitivity to the presence of the reflected/reprocessed component proper (continuum) is greatly limited. The upper limit on the possible presence of the reflected continuum (the *pexrav* model of the XSPEC package, Magdziarz and Zdziarski 1995) is $\Omega/2\pi < 0.3$, where Ω is the solid angle shadowed by the reflecting surface. The power-law best-fit parameters for the spectrum of the source are given in the table.

DISCUSSION

Over the several months that have elapsed since the beginning of its in-orbit operation, the INTEGRAL observatory has discovered several new sources with similar properties; these sources may be arbitrarily called weak hard transients: IGR J17091−3624 (Kuulkers *et al.* 2003), IGR J18539+0727 (Lutovinov *et al.* 2003a), IGR J18325 −0756 (Lutovinov *et al.* 2003b), IGR 17597−2201 (Lutovinov *et al.* 2003c), and IGR J18483−0311 (Chernyakova *et al.* 2003). In this case, the term "hard" means that all these sources, despite their low fluxes, were significantly detected by INTEGRAL in the hard energy range 40−100 keV. In this paper, we studied the spectral and temporal characteristics of two of these sources, IGR J17091−3624 and IGR J18539+0727, observed by RXTE in the energy range 3−20 keV several days after their discovery by INTEGRAL. The spectra of the sources are well described by a power-law decrease of the photon flux with energy $(dN(E) \propto E^{-\Gamma} dE)$. Because of the proximity of IGR J17091−3624 to the Galactic center and the appreciable influence of Galactic ridge emission, which contains a number of lines near 6−7 keV, the lines in its spectrum cannot be studied. However, the fluorescent line of neutral iron at energy ∼6.4 keV is clearly detectable in the spectrum of IGR J18539+0727 (Fig. 3b, the table). This fluorescent line is commonly observed in binary systems in their hard spectral state, and its origin is associated with the reflection of the hard X-ray radiation of inner accretion-flow regions from an optically thick accretion disk (see, e.g., Basko *et al.* 1974; Gilfanov *et al.* 1999).

Both sources exhibit a large variability on time scales from several tenths of a second to several tens of seconds. The parameters of the energy and power-density spectra for the sources allow them to be reliably classified as X-ray binary systems in the low/hard spectral state. The significant radio activity of IGR J17091−3624 (Rupen *et al.* 2003) is an indirect, although ambiguous confirmation of this classification (Fender and Hendry 2000). The parameters of the power-density spectra for the sources have long been the subject of discussion in connection with the possibility of determining from them the nature of the compact object (Wijnands and van der Klis 1999; Sunyaev and Revnivtsev 2000). It has been shown many times that the light curves of X-ray binary systems with neutron stars in the low spectral state contain predominantly higher-frequency variability than do binary systems with black holes. The power-density spectra at high frequencies allow us to introduce a stringent criterion for distinguishing between neutron stars and black holes. However, as yet there are no such stringent criteria for distinguishing between neutron stars and black holes

Best-fit parameters for the spectra of IGR J17091−3624 and IGR J18539+0727

Parameter	IGR J17091−3624[a]	IGR J18539+0727
Absorption column density $N_H L$, 10^{22} cm^{-2}	<1	1.5 ± 0.4
Photon index Γ	1.43 ± 0.03	1.47 ± 0.05
Emission-line energy, keV	—[b]	6.4 ± 0.1
Linewidth, keV	—[b]	<0.3
Equivalent width EW, eV	—[b]	135 ± 25
Flux (3−25 keV), 10^{-10} erg s^{-1} cm^{-2}	1.0	1.8

[a] When fitting the spectrum of IGR J17091−3624, we subtracted the contribution of the Galactic ridge emission background. The background was normalized to a 3−20-keV flux of ∼1.9×10^{-11} erg s^{-1} cm^{-2}/(the PCA field of view), which roughly corresponds to the results by Revnivtsev (2003).

[b] Because of the Galactic ridge emission, we cannot say with confidence whether the emission line is present near 6−7 keV in the source's spectrum.

using the parameters of the power-density spectra at low frequencies. Studies indicate that neutron stars usually (predominantly) have no power-density spectra with a lower cutoff frequency below ∼0.1 Hz (Wijnands and van der Klis 1999). In our case, the power-density spectrum of IGR J18539+0727 has a characteristic cutoff frequency much lower than this empirical boundary. Therefore, we may assume with confidence that IGR J18539+0727 is a black-hole candidate. The characteristics of the other source (IGR J17091−3624) do not allow us to unambiguously make this assumption, although the significant radio flux detected from it (Rupen et al. 2003) together with the observed hard X-ray radiation can be an argument for this assumption (Fender 2001). Nevertheless, to ultimately elucidate the nature of the compact object in the above systems requires further observations, primarily an optical identification of the companion stars and a measurement of the mass functions for the systems.

REFERENCES

1. M. Basko, R. Sunyaev, and L. Titarchuk, Astron. Astrophys. **31**, 249 (1974).
2. H. Bradt, R. Rothschild, and J. Swank, Astron. Astrophys., Suppl. Ser. **97**, 355 (1993).
3. M. Chernyakova, A. Lutovinov, F. Capitanio, et al., Astron. Telegr. **157** (2003).
4. R. Fender, Mon. Not. R. Astron. Soc. **322**, 31 (2001).
5. R. Fender and M. Hendry, Mon. Not. R. Astron. Soc. **317**, 1 (2000).
6. M. Gilfanov, E. Churazov, and M. Revnivtsev, Astron. Astrophys. **352**, 182 (1999).
7. E. Kuulkers, A. Lutovinov, A. Parmar, et al., Astron. Telegr. **149** (2003).
8. A. Lutovinov, J. Rodriguez, N. Produit, et al., Astron. Telegr. **151** (2003a).
9. A. Lutovinov, S. Shaw, L. Foschini, et al., Astron. Telegr. **154** (2003b).
10. A. Lutovinov, R. Walter, G. Belanger, et al., Astron. Telegr. **155** (2003c).
11. P. Magdziarz and A. Zdziarski, Mon. Not. R. Astron. Soc. **273**, 837 (1995).
12. M. Revnivtsev, Astron. Astrophys. (2003, in press); astro-ph/0304351.
13. M. Revnivtsev, M. Gilfanov, E. Churazov, and R. Sunyaev, Astron. Telegr. **150** (2003).
14. M. Rupen, A. Mioduszewski, and V. Dhawan, Astron. Telegr. **152** (2003).
15. R. Sunyaev and M. Revnivtsev, Astron. Astrophys. **358**, 617 (2000).
16. A. Valinia and F. Marshall, Astrophys. J. **505**, 134 (1998).
17. R. Wijnands and M. van der Klis, Astrophys. J. **514**, 939 (1999).
18. J. in't Zand, J. Heise, P. Lowes, et al., Astron. Telegramm **160** (2003).

Translated by G. Rudnitskiĭ

Gravitational Collapse and Equilibrium Conditions
of a Toroidal Vortex with Thermal Pressure

K. Yu. Bliokh[1] and V. M. Kontorovich[1,2*]

[1]*Institute of Radio Astronomy, National Academy of Sciences of Ukraine, Krasnoznamennaya ul. 4, Kharkov, 61002 Ukraine*
[2]*Karazin National University, pl. Svobody 4, Kharkov, 61077 Ukraine*
Received May 14, 2003

Abstract—We found the equilibrium conditions for a self-gravitating toroidal vortex by taking thermal pressure into account. These conditions are shown to significantly differ from those for a disk or a sphere. The evolution of a thin vortex turns it into a compact vortex that loses mechanical stability for low masses at a polytropic index $\gamma < 4/3$ but retains stability for sufficiently high masses and densities determined by the velocity circulation in the vortex. © *2003 MAIK "Nauka/Interperiodica"*.

Key words: *self-gravitating toroidal vortex, equilibrium conditions, gravitational collapse.*

INTRODUCTION

Obviously, the physical stability conditions for a self-gravitating vortex torus (Fig. 1) fundamentally differ from those for a disk. First of all, the constancy of the circulation $\Gamma = 2\pi r v$ in the vortex results in maximum velocity at the smallest (inner) radius of the torus, and the condition imposed by it on the angular velocity $\Omega(r) = \Gamma/2\pi r^2$ results in the absence of epicyclic frequency $[\nu(r)]^2 = \dfrac{1}{r^3}\dfrac{d}{dr}\left[r^2\Omega(r)\right]^2$ in the main approximation. Whereas during the rotation of a disk or a sphere, the detaching particles escape from the equator (to form an additional disk in the case of a sphere), the particles in a toroidal vortex detach at the minimum radius and escape to form a one-sided jet[1] even in the absence of a magnetic field (Bliokh and Kontorovich 2003; Shatskiĭ and Kardashev 2002; Spivey 2000; Ansorg *et al.* 2002). In addition to the detachment due to particle collisions in the vortex torus, which is facilitated by the self-intersecting trajectories in the effective potential of the vortex (Bliokh and Kontorovich 2003), the particles can be effectively accelerated along the torus axis by the induction field in the case of a magnetized torus (Shatskiĭ and Kardashev 2002).

The discovery of obscuring tori (see the review by Antonucci 1993) and their direct observation both in galactic (Risaliti *et al.* 2003) and stellar objects (see Bogovalov and Khangulyan (2002) for references) makes the problem of studying gravitating toroidal vortices particularly relevant. As far as we know, this problem has not been considered until recently (for references, see Bliokh and Kontorovich (2003), who made the first attempt). In this paper, we extend our results to finite temperatures and take into account the effects of thermal pressure. As we will see below, this will affect the equilibrium and collapse conditions.

EQUATIONS OF MOTION

Previously, based on Hamiltonian dynamics, we derived the equations that described the evolution of

---

*E-mail: `vkont@ira.kharkov.ua`

[1]The excitation of a unidirectional flow by a magnetized rotating torus was considered by Bisnovatyi-Kogan (1989) as a possible formation mechanism of cosmic jets (Ustyugova *et al.* 2000). For a qualitative association of one-sided jets changing direction with rotating binary galactic nuclei, see Zhuravlev and Komberg (1999).
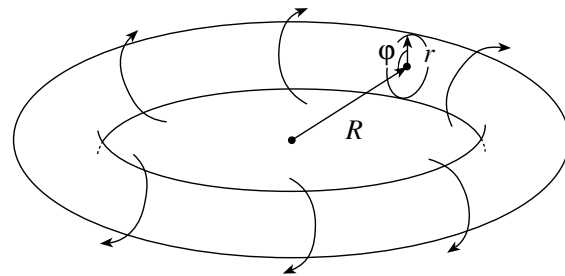

Fig. 1. A thin toroidal vortex. The arrows indicate the directions of the streamlines that produce the velocity circulation.

a thin self-gravitating toroidal vortex:

$$\ddot{r} = \frac{p_\varphi^2}{M^2 r^3} - G\frac{M}{\pi R r}, \quad \ddot{R} = -G\frac{M}{\pi R^2}\ln\frac{\alpha r}{R}. \quad (1)$$

Here, r and R are the small and large radii of the torus, M is the total vortex mass, G is the gravitational constant, $\alpha \sim 1$ is a numeric factor, and $p_\varphi = Mr^2\dot{\varphi} = $ const is the angular momentum of the matter (φ is the cyclic rotation coordinate at the small radius).

To introduce the thermal pressure forces into the equations of motion (1), we note that the virtual work done by the external forces against the pressure force is

$$\delta A = -\delta E = p\delta V, \quad (2)$$

where p is the pressure in the vortex, and V is the vortex volume (below, we disregard the distribution of matter and pressure at the small torus radius while ignoring the factors of the order of unity in the formulas). Since the torus volume is $V = 2\pi^2 r^2 R$, we obtain from (2)

$$-\delta E = 4\pi^2 rRp\delta r + 2\pi^2 r^2 p\delta R. \quad (3)$$

Hence, we find the forces acting along the r and R coordinates $F_r = -\delta E/\delta r$ and $F_R = -\delta E/\delta R$ and, accordingly, the additional terms in the pressure forces in (1):

$$\ddot{r} = \frac{p_\varphi^2}{M^2 r^3} - G\frac{M}{\pi R r} + \frac{p}{M}4\pi^2 Rr, \quad (4)$$

$$\ddot{R} = -G\frac{M}{\pi R^2}ln\frac{\alpha r}{R} + \frac{p}{M}2\pi^2 r^2.$$

To relate the pressure to the vortex parameters, we must invoke the equation of state for the matter and the vortex evolution. We assume that the gas is perfect and that the compression (expansion) is polytropic. Introducing the initial temperature of the matter T_0, the initial vortex parameters r_0 and R_0, and the mass of one gas particle m_0, we then obtain

$$p = \frac{p_0 V_0^\gamma}{V^\gamma} = \frac{MT_0}{m_0}\frac{(2\pi^2 r_0^2 R_0)^{\gamma-1}}{(2\pi^2 r^2 R)^\gamma}.$$

Substituting this expression into (4), we obtain instead of (1)

$$\ddot{r} = \frac{p_\varphi^2}{M^2 r^3} - G\frac{M}{\pi R r} + \frac{T_0}{m_0}\frac{2(r_0^2 R_0)^{\gamma-1}}{r^{2\gamma-1}R^{\gamma-1}}, \quad (5)$$

$$\ddot{R} = -G\frac{M}{\pi R^2}ln\frac{\alpha r}{R} + \frac{T_0}{m_0}\frac{(r_0^2 R_0)^{\gamma-1}}{r^{2\gamma-2}R^\gamma}.$$
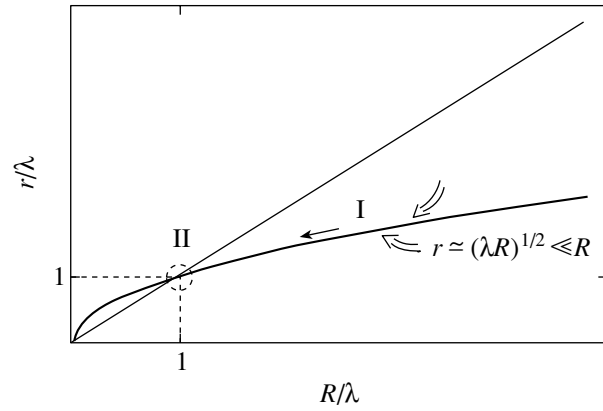
Fig. 2. Schematic evolution of a vortex without thermal pressure (Bliokh and Kontorovich 2003).

EQUILIBRIUM CONDITIONS

As previously, we assume that for a thin torus ($r \ll R$), the evolution (Fig. 2) at the small radius is much faster than it is at the large radius, and that a quasi-equilibrium state in r is initially established. This state is determined by the fact that the force on the right-hand side of the first equation (5) vanishes:

$$\frac{p_\varphi^2}{M^2 r^3} - G\frac{M}{\pi R r} + \frac{T_0}{m_0}\frac{2(r_0^2 R_0)^{\gamma-1}}{r^{2\gamma-1}R^{\gamma-1}} = 0. \quad (6)$$

This equation is not solvable directly, and implicitly specifies the relation $r(R)$. However, if we introduce the linear mass per unit length of the torus ring $\chi = M/2\pi R$, the mean density $\rho = M/2\pi^2 r^2 R$, and the velocity circulation $\Gamma = 2\pi p_\varphi/M$ and consider (6) as the equation for the linear Jeans mass $\chi(\rho)$, then an explicit expression follows from it:

$$\chi(\rho) = \frac{T_0}{2Gm_0}\frac{\rho^{\gamma-1}}{\rho_0^{\gamma-1}}\left\{1 + \sqrt{1 + \xi\rho^{3-2\gamma}\Gamma^2}\right\}, \quad (7)$$

$$\text{where} \quad \xi = \frac{G}{2\pi}\left(\frac{m_0\rho_0^{\gamma-1}}{T_0}\right)^2.$$

Since $\chi = \pi r^2\rho$, it is convenient to consider formula (7) in the same way as the formula for the small vortex radius in the equilibrium conditions at the first evolutionary stage.

Equating $\chi(\rho) = \chi$ and inverting relation (7) yields an equation for the equilibrium density at the specified linear mass χ and velocity circulation Γ. Without analyzing $\chi(\rho)$ for reasons of space, we note that an equilibrium solution always exists (Fig. 3) if the density does not exceed ρ_*:

$$\rho < \rho_* = (f_*/2)^{\frac{1}{\gamma-1}}, \quad (8')$$
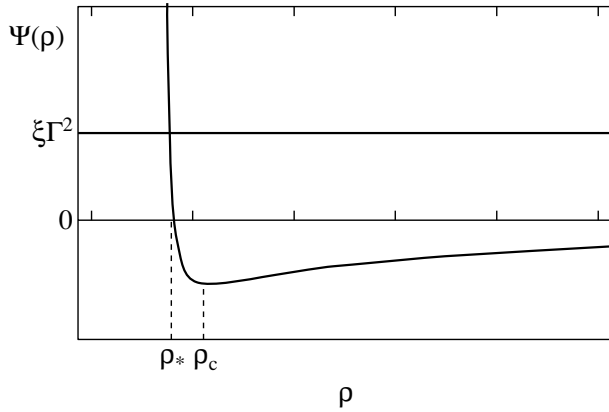
Fig. 3. The right-hand side of Eq. (8) for a thin toroidal vortex versus its density.

where $f_* = \nu\chi$ is proportional to the linear mass of the vortex, $\nu = 2G\left(m_0\rho_0^{\gamma-1}/T_0\right)$.

In this case, the equilibrium density satisfies the transcendental equation

$$\xi\Gamma^2 = \frac{f_*\left(f_* - 2\rho^{\gamma-1}\right)}{\rho}, \qquad (8)$$

whose right-hand side degenerates into a hyperbola for $\gamma = 1$ or into a hyperbola shifted in the vertical axis for $\gamma = 2$.

Once the local equilibrium (6) has been established, the vortex will slowly evolve at the large radius R with the conservation of the relation $r(R)$. If the force on the right-hand side of the second equation (5) is assumed to be negative, then the contraction will continue until this force vanishes:

$$-G\frac{M}{\pi R^2}ln\frac{\alpha r}{R} + \frac{T_0}{m_0}\frac{\left(r_0^2 R_0\right)^{\gamma-1}}{r^{2\gamma-2}R^\gamma} = 0. \qquad (9)$$

If the thermal pressure forces are small compared to the centrifugal forces, then the first two terms in (6) compete, and the thermal pressure is also low compared to the gravitational forces. In this case, we obtain the square-root dependence $r \sim \sqrt{R}$ considered previously (Bliokh and Kontorovich 2003). The contraction at the large radius gradually overtakes the contraction at the small radius, and there comes a time when they become of the same order of magnitude, $r \sim R$. This order-of-magnitude relation also corresponds to equilibrium (9): in this region, the gravitational force is balanced by an arbitrarily weak thermal pressure, because the logarithm is small. If, however, the thermal pressure forces are large compared to the centrifugal forces, then the last two terms in (6) compete. As can be easily seen, their balance corresponds to the equilibrium condition (9), where

$\ln(\alpha r/R) \sim 1$. Obviously, this case also corresponds to $r \sim R$.

Thus, irrespective of the thermal pressure, the vortex equilibrium is established in the region where both torus radii become of the same order of magnitude: $r \sim R$. Using dependence (6), we obtain the following equation for the equilibrium parameters:

$$\frac{p_\varphi^2}{M^2 R^3} - G\frac{M}{\pi R^2} + \frac{T_0}{m_0}\frac{2\left(r_0^2 R_0\right)^{\gamma-1}}{R^{3\gamma-2}} = 0. \qquad (10)$$

This equation defines the characteristic radius R of a compact vortex that came to an equilibrium: the balance between the compressing gravitational forces and the extending centrifugal and thermal pressure forces.[2]

Equation (10), like (6), is not explicitly solvable for R. We may consider two limiting cases. When the pressure forces are small (the first term is much larger than the third term), we come to the equilibrium between the gravitational and centrifugal forces considered previously (Bliokh and Kontorovich 2003). In this case,

$$R \sim \frac{p_\varphi^2}{GM^3}. \qquad (11)$$

In the opposite limit, when the centrifugal forces are small (the first term in (10) is much smaller than the third term), we come to the equilibrium between the gravitational and pressure forces:

$$R^{3\gamma-4} \sim \frac{T_0\left(r_0^2 R_0\right)^{\gamma-1}}{GMm_0} \sim \frac{T_0 V_0^{\gamma-1}}{GMm_0}. \qquad (12)$$

The limiting value of (11) is obtained for the parameters that satisfy

$$\frac{T_0 V_0^{\gamma-1}}{m_0}\frac{G^{3\gamma-5}M^{9\gamma-13}}{p_\varphi^{6\gamma-8}} \ll 1, \qquad (13)$$

while the limiting value of (12) is obtained for the inverse inequality.

---

[2]Actually, in the region $r \sim R$, the initial approximation of a thin ring torus and the separation of evolution scales in r and R becomes invalid. Here, we must consider a single compact object that resembles the Hill vortex rather than the Maxwell vortex. This can be easily done by analogy with our previous study (Bliokh and Kontorovich 2003) by including the pressure forces for a spheroidal vortex, as above. However, in this case, we obtain an equation that differs from (6) only by factors of the order of unity, which are anyway unimportant in our rough analysis. Therefore, we omit here these calculations.

ANALYSIS OF THE EQUILIBRIUM CONDITIONS: EQUILIBRIUM AND NONEQUILIBRIUM JEANS MASSES

In the equilibrium equation (10), we change from the radius R and the angular momentum p_φ to the density $\rho \sim M/R^3$ and the circulation $\Gamma = p_\varphi/M$. Equation (10) then transforms into an equation for the generalized Jeans mass $M(\rho)$:

$$GM^{4/3} - \frac{T_0}{m_0}\frac{\rho^{\gamma-4/3}}{\rho_0^{\gamma-1}}M^{2/3} - \Gamma^2\rho^{1/3} = 0, \quad (14)$$

where we omit the dimensionless factors of the order of unity, which will be restored below. Solving the equation yields $M^{2/3}(\rho)$:

$$\nu M^{2/3}(\rho) = \rho^{\gamma-4/3}\left[1 + \sqrt{1 + \xi\rho^{3-2\gamma}\Gamma^2}\right],$$

where $\nu = \dfrac{2Gm_0\rho_0^{\gamma-1}}{T_0}, \xi = 4G\left(\dfrac{m_0\rho_0^{\gamma-1}}{T_0}\right)^2$.

The equilibrium states are defined by the equality $M = M(\rho)$, where M is the vortex mass. Let us analyze the function $M^{2/3}(\rho)$ and ascertain whether stable equilibrium states can exist.

The equation $dM^{2/3}(\rho)/d\rho = 0$ with $\gamma < 4/3$ gives only one extremum (minimum) of the function $M(\rho)$:

$$\rho_c^{3-2\gamma} = 36\left(\gamma - \frac{4}{3}\right)\left(\gamma - \frac{5}{3}\right)\bigg/\xi\Gamma^2. \quad (15)$$

For $\gamma > 5/3$, there is also a positive root, but it is redundant, as can be seen from the derivation of formula (15) (see Appendix A). The value of $M_c^{2/3} \equiv M^{2/3}(\rho_c)$ for $\gamma < 4/3$ is

$$M_c^{2/3} = \frac{T_0}{2Gm_0}\frac{\rho_c^{\gamma-4/3}}{\rho_0^{\gamma-1}} \quad (16)$$

$$\times \left[1 + \sqrt{1 + 36\left(\gamma - \frac{4}{3}\right)\left(\gamma - \frac{5}{3}\right)}\right].$$

Note that for $\gamma \to 4/3$ $\rho_c \to 0$, and to calculate $M_c^{2/3}$, we must evaluate the indeterminate form $\lim_{x\to0+} x^{-x} = 1$. As a result, for $\gamma \to 4/3$, $M_c^{2/3} \to T_0/Gm_0\rho_0^{\gamma-1}$. As we see, whereas for $\gamma > 4/3$, the function $M^{2/3}(\rho)$ monotonically decreases with increasing density and there is a solution that describes an equilibrium vortex for any mass, for $\gamma \leq 4/3$, a gap in masses emerges. The equilibrium is possible only for masses larger than some critical mass (16). For $\gamma < 4/3$, this critical mass depends on the circulation Γ.
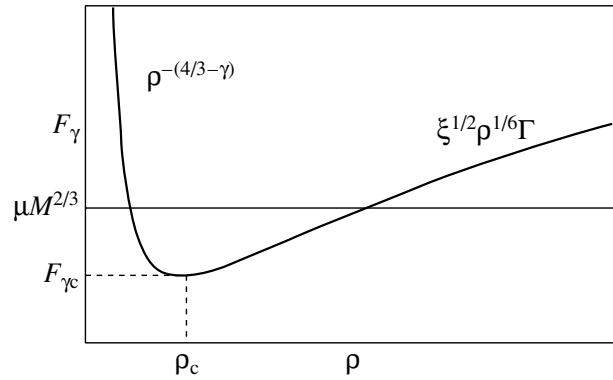
Fig. 4. Critical Jeans mass versus torus density for a polytropic index $\gamma < 4/3$. The ascending branch F_γ ($\rho > \rho_c$) is stable and is determined by the circulation Γ.

Here, we see a significant difference from the gravitational contraction of a nonrotating body, for which no stable equilibrium states are known to exist for $\gamma < 4/3$.

For vortex masses higher than the critical mass M_c that corresponds to the minimum of $M(\rho)$, there are two solutions (Fig. 4). One of them is unstable at densities lower than ρ_c and corresponds to the intersection of the descending branch of the function $M(\rho)$ by the level of a given mass M. It is similar to the collapse of a nonrotating mass: the Jeans mass decreases with increasing density, causing the contraction to continue.

In contrast, at densities higher than ρ_c, a stable state is realized: the Jeans mass increases as it contracts, and no collapse takes place. This equilibrium state is essentially determined precisely by the rotation of matter in the vortex: the asymptotics of $M^{2/3}(\rho)$ at high densities is $M^{2/3}(\rho) \propto \Gamma\rho^{1/6}$ ($\rho \to \infty$).

OBTAINING THE RESULTS FROM EVALUATION CONSIDERATIONS AND OTHER APPROACHES

Here, as in our previous paper (Bliokh and Kontorovich 2003), we made good use of the approach of classical Hamiltonian mechanics to solve the problem of the evolution of a toroidal vortex. In this section, we show that the results obtained from the mechanical model can also be obtained from dimension and similarity considerations. In addition, in Appendix B, we show that the hydrodynamic allowance for the thermal pressure yields the same results.

Let us first return to a cold system and consider the final evolutionary stage, when the small and large vortex radii become equal in order of magnitude. In this

case, the number of defining parameters decreases to the extent that the characteristic radius R can be determined from the dimension considerations alone. Indeed, such parameters are the conserved mass M and circulation Γ (or angular momentum $p_\varphi = M\Gamma$) as well as the gravitational constant G that determines the interaction mechanism (self-gravitation). From these quantities, we can construct only one quantity with the dimension of length, which can be naturally identified with the Jeans length

$$\lambda = \frac{\Gamma^2}{GM}. \qquad (17)$$

Formula (17) is identical to the expression for the equilibrium radius of a compact cold vortex (Bliokh and Kontorovich (2003), formula (23)) if Γ is taken to mean the circulation divided by 2π.

Let us now turn to the early evolutionary stage of a cold vortex, when it is a thin ($r \ll R$) torus with the local quasi-equilibrium dependence $r = r(R)$. The latter can be derived from the balance between the gravitational (GM/R) and centrifugal ($p_\varphi^2/2Mr^2$) energies:

$$r^2 \sim \frac{\Gamma^2}{GM}R = \lambda R. \qquad (18)$$

Thus, $\tilde{\lambda} = \sqrt{\lambda R}$ acts as the Jeans scale for the small radius. Formula (18) is again identical, to within a factor of about unity, to that derived previously (Bliokh and Kontorovich (2003), formula (14)). The square-root dependence $r \sim \sqrt{\lambda R}$ is related to the corresponding coordinate dependences: $\propto 1/R$ for gravitation and $\propto 1/r^2$ for centrifugal energy. As R decreases, $r \to R$, and we observe the transition to the final evolutionary stage, $\tilde{\lambda} \to \lambda$, in accordance with what was said above.[3]

Let us now take into account the thermal motion in the problem under consideration. Restricting our analysis to the late evolutionary stage, when only one scale with the dimension of length is available, we substitute in (17)

$$v^2 \to v^2 + v_T^2, \qquad (19)$$

where v is the regular velocity, and v_T is the thermal velocity. Since $\Gamma^2 = R^2 v^2$, the following change will occur in λ:

$$\lambda \to \frac{\Gamma^2 + R^2 v_T^2}{GM}. \qquad (20)$$

---

[3]Note that the inner radius (the radius of the hole of a compact vortex torus that is the difference between the quantities of the same order of R) cannot determined by such a rough analysis. Meanwhile, its knowledge is of crucial importance in solving the problem of jet formation and torus collapse.

The equilibrium equation $R = \lambda$ now transforms into an equation for R that, after substituting the equations of state for an ideal gas $v_T^2 \propto T$ and a polytropic process $T \propto \rho^{\gamma-1}$ into (20), is identical (to within factors of about unity) to Eq. (10). We also see that for given circulation and temperature, there is a lower limit on the equilibrium mass:

$$M_J \geq \frac{2\Gamma v_T}{G}. \qquad (21)$$

The equilibrium condition for a toroidal vortex is derived from hydrodynamic equations in Appendix B. In our derivation, we use an analogy with the Jeans dispersion relation for heavy sound:

$$\omega^2 = (kv_T)^2 - \omega_J^2, \quad \omega_J^2 = 4\pi G\rho_0, \qquad (22)$$

by extending it to the case where there is a regular motion at velocity v:

$$\omega^2 = k^2 \left(v_T^2 + v^2\right) - \omega_J^2. \qquad (23)$$

Since such generalizations have long been used for a disk (Pikel'ner 1976; Saslaw 1985; Tassoul 1978), we immediately note the difference. The disk geometry changes ω_J by a factor of $\sqrt{2}$; in addition, the dispersion relation for a disk contains an epicyclic frequency. In our case, this frequency is absent, as was noted in the Introduction. Note also that the dispersion relation (23) contains no term linear in v (responsible for the Doppler effect), because the radial oscillations in the torus tube under consideration (see Appendix B) and the regular velocity are orthogonal to each other.

CONCLUSIONS

In the case under consideration, there are no epicyclic oscillations, because the velocity circulation is constant, which, together with the coordinate independence of the density, significantly simplifies the problem and makes possible the closed analytical study of it presented here. The possible appearance of jets that carry away the angular momentum must result in the continuation of contraction and collapse even in situations that are stable from the viewpoint of our analysis.

The relativistic generalizations of the problem under discussion, as well as our study, can be useful in astrophysical applications (from young stellar objects and supernovae to active galactic nuclei) in which self-gravitation and rotation are important. It may also be important to take into account the orbital rotation of the torus and the presence of a central mass, the influence of which was ignored in this paper (see Bliokh and Kontorovich (2003) for remarks).

APPENDIX A

FINDING THE EXTREMUM OF THE FUNCTION $M(\rho)$

Let us determine the derivative $dM^{2/3}(\rho)/d\rho$ from (14) and set it equal to zero:

$$\frac{dM^{2/3}(\rho)}{d\rho}$$

$$= \left(\gamma - \frac{4}{3}\right)\rho^{\gamma-\frac{4}{3}-1}\left(1 + \sqrt{1 + \xi\Gamma^2\rho^{3-2\gamma}}\right)$$

$$+ \rho^{\gamma-\frac{4}{3}}\frac{\xi\Gamma^2(3-2\gamma)\rho^{3-2\gamma-1}}{2\sqrt{1+\xi\Gamma^2\rho^{3-2\gamma}}} = 0.$$

Canceling by $\rho^{\gamma-\frac{4}{3}-1}$ and gathering the terms, we obtain

$$-2\left(\gamma - \frac{4}{3}\right)\sqrt{1 + \xi\Gamma^2\rho^{3-2\gamma}} = 2\left(\gamma - \frac{4}{3}\right)$$

$$+ \frac{1}{3}\xi\Gamma^2\rho^{3-2\gamma}.$$

We see that for $\gamma > 4/3$, the equality is impossible, because the signs of the right- and left-hand sides differ. Let us introduce $z \equiv \rho^{3-2\gamma}$. For $\gamma < 4/3$, the equality is possible if $2\left(\gamma - \frac{4}{3}\right) + \frac{1}{3}\xi\Gamma^2 z > 0$. After squaring, we find the solution

$$z_{\mathrm{c}} = \frac{36(\gamma - 4/3)(\gamma - 5/3)}{\xi\Gamma^2},$$

which we can use for $4/3 > \gamma > 4/3 - \xi\Gamma^2 z/2$, according to the above conclusion. As can be easily verified, the derived value of z_{c} satisfies the required inequality.

APPENDIX B

A HYDRODYNAMIC APPROACH TO THE PROBLEM

Let us first derive the dispersion relation for acoustic waves in a thin self-gravitating gaseous ring by replacing it by a cylinder with periodic boundary conditions at its ends. The basic equations are the hydrodynamic equations in a self-consistent gravitational field:

$$\frac{\partial \mathbf{v}}{\partial t} + (\mathbf{v}\nabla)\mathbf{v} = -\frac{1}{\rho}\nabla p - \nabla\phi, \qquad (B1)$$

$$\frac{\partial \rho}{\partial t} + \mathrm{div}\rho\mathbf{v} = 0, \quad \Delta\phi = 4\pi G\rho.$$

We assume the unperturbed density ρ_0 to be independent of the coordinates; i.e., we ignore the effect of the unperturbed potential ϕ_0, which seems quite justified for a thin torus. For purely radial modes, we then obtain the equation

$$\frac{\partial}{\partial r}\frac{1}{r}\frac{\partial}{\partial r}(r\tilde{v}_r) + \frac{\omega^2 + \omega_J^2}{c_{\mathrm{s}}^2}\tilde{v}_r = 0. \qquad (B2)$$

Here, $\tilde{v}_r$ is the perturbed radial velocity, ω is the oscillation frequency, $\omega_J = \sqrt{4\pi G\rho_0}$ is the Jeans frequency, and c_{s} is the speed of sound. Ther substitution $\dfrac{\sqrt{\omega^2 + \omega_J^2}}{c_{\mathrm{s}}}r \to z$ reduces Eq. (B2) to the Bessel equation

$$z^2\frac{\partial^2 v}{\partial z^2} + z\frac{\partial v}{\partial z} + (z^2 - 1)v = 0$$

for $v(z) = \tilde{v}_r(r(z))$. The solution $J_1(z)$ corresponds to the zero boundary conditions on the cylinder if the following condition is satisfied:

$$\frac{\sqrt{\omega^2 + \omega_J^2}}{c_{\mathrm{s}}}r_0 = j_1,$$

where j_1 is the first zero of the function $J_1(z)$, and r_0 is the cylinder radius. Thus, the dispersion relation is

$$\omega^2 = \frac{c_{\mathrm{s}}^2}{r_0^2}j_1^2 - \omega_J^2. \qquad (B3)$$

We have omitted the mode index for the frequency; obviously, we can also choose another oscillation mode. However, because of the inequalities for the eigenvalues of the Sturm–Liouville problem, only the contribution of the fundamental nodeless mode is important in studying the stability.

The dispersion relation (B3) includes the finite temperature, but without the vortex motion of matter in the torus. In contrast, the equilibrium conditions at the small radius in a thin vortex obtained previously,

$$r = \sqrt{\frac{\pi p_\varphi^2 R}{GM^3}}, \qquad (B4)$$

include only the regular vortex motion. To take into account the two factors, we note that condition (B4) can be rewritten as

$$\frac{2\Gamma^2}{\pi r^4} - \omega_J^2 = 0. \qquad (B5)$$

Thus, comparing (B5) and (B6), we can easily write the equilibrium condition $\omega^2 = 0$ with thermal pressure in the general case of interest to us:

$$\frac{2\Gamma^2}{\pi r^4} + \frac{c_{\mathrm{s}}^2}{r^2}j_1^2 - \omega_J^2 = 0. \qquad (B6)$$

The corresponding "dispersion" relation contains ω^2 instead of zero on the right-hand side. Therefore, the

negativity of the left-hand side of (B6) corresponds to the instability ($\omega^2 < 0$).

If we express ω_J^2 in terms of the vortex mass and radii, then, after several simple transformations, we can derive an expression for the equilibrium small radius of the torus:

$$r^2 = \frac{4\Gamma^2/\pi^3}{\frac{GM}{\pi R} - 2c_s^2 j_1^2}. \tag{B7}$$

Since $c_s = c_s(T)$, for isothermal compression, (B7) is the final expression for the quasi-equilibrium small radius that acts as the Jeans scale. We see that an allowance for finite temperature causes an increase in the Jeans scale (which tends to ∞ as $2\pi c_s^2 J_1^2 \to GM/R$) and, accordingly, a deviation from the square-root dependence $r \propto \sqrt{R}$ that arises at $T = 0$. Since, in general, c_s indirectly depends on r, (B7) is not the solution for $r(R)$, but must itself be considered as an equation. Multiplying (B7) by $2\pi^2 R\rho$, we obtain an equation for the Jeans mass $\chi(\rho)$ per unit length of a thin torus $\chi \equiv M/2\pi R$ that describes the first evolutionary stage of the vortex; for its solution, see in (7) at $\nu = \dfrac{2G}{\zeta\sigma\tau}$, $\xi = \dfrac{32G}{(\pi\zeta\sigma\tau)^2}$, where $\sigma = \dfrac{c_s^2}{T}$ and $\tau = \dfrac{T}{\rho^{\gamma-1}}$.

To within factors of about unity, formulas (B6) and (B7) are identical to the local equilibrium condition (6) when the equation of state for an ideal gas $c_s^2 \propto T$ and a polytropic process $T \propto \rho^{\gamma-1}$ are substituted into them. If we set $r = \epsilon R$ ($\epsilon < 1$), then (B6) will naturally lead us to the equilibrium condition (10) and solution (14) for the Jeans mass of a compact vortex at

$$\mu = (2/\pi)^{1/3} G/\kappa, \quad \xi = 8G/(\kappa\epsilon\pi)^2, \tag{B8}$$
$$\kappa = \zeta c_s^2 \rho^{1-\gamma}.$$

Thus, both the mechanical and hydrodynamic approaches to the problem under consideration yield identical (within the accuracy under discussion) equations and results.

REFERENCES

1. M. Ansorg, A. Kleinwachter, and R. Meinel, gr-qc/0211040 (2002).
2. R. Antonucci, Ann. Rev. Astron. Astrophys. **31**, 473 (1993).
3. G. S. Bisnovatyi-Kogan, *Physical Aspects of the Stellar Evolution Theory* (Nauka, Moscow, 1989) [in Russian].
4. K. F. Bliokh and V. M. Kontorovich, Zh. Éksp. Teor. Fiz. **123**, 1123 (2003) [JETP **96**, 985 (2003)].
5. S. V. Bogovalov and D. V. Khangoulian, astro-ph/0209269 (2002).
6. B. Carter and J. B. Hartle, *Gravitation in Astrophysics*, NATO ASI Series **156** (1986).
7. *The Origin and Evolution of Galaxies and Stars*, Ed. by S. B. Pikel'ner (Nauka, Moscow, 1976).
8. F. Pomplio, S. M. Harun-ar-Rashid, and M. Roos, astro-ph/0008475 (2000).
9. G. Risaliti, L. Woltjer, and M. Salvati, astro-ph/0301522 (2003).
10. W. C. Saslaw, *Gravitational Physics of Stellar and Galactic Systems* (Cambridge Univ. Press, Cambridge, 1985; Mir, Moscow, 1989).
11. A. A. Shatskiĭ and N. S. Kardashev, Astron. Zh. **79**, 708 (2002) [Astron. Rep. **46**, 639 (2002)].
12. R. J. Spivey, astro-ph/0004051 (2000).
13. J.-L. Tassoul, *Theory of Rotating Stars* (Princeton Univ. Press, Princeton, 1978; Mir, Moscow, 1982).
14. G. V. Ustyugova, R. V. E. Lavelace, M. M. Romanova, *et al.*, Astrophys. J. **541**, L21 (2000).
15. Ya. B. Zel'dovich and I. D. Novikov, *Theory of Gravitation and Stellar Evolution* (Nauka, Moscow, 1971).
16. V. I. Zhuravlev and B. V. Komberg, Astron. Zh. **76**, 163 (1999) [Astron. Rep. **43**, 135 (1999)].

Translated by G. Rudnitskiĭ

The H₂O Maser Toward IRAS 06308+0402

M. I. Pashchenko[1*], E. E. Lekht[2**], and A. M. Tolmachev[3]

[1]*Sternberg Astronomical Institute, Universitetskii pr. 13, Moscow, 119992 Russia*

[2]*Instituto Nacional de Astrofísica, Óptica y Electrónica, Luis Enrique Erro No. 1, Apdo Postal 51 y 216, 72840 Tonantzintla, Puebla, México*

[3]*Pushchino Radio Astronomy Observatory, Astrospace Center, Lebedev Institute of Physics, Russian Academy of Sciences, Pushchino, Moscow oblast, 142290 Russia*

Abstract—We present the monitoring results for the H₂O maser toward the infrared source IRAS 06308+0402 associated with a dense cold molecular cloud. The observations were carried out with the 22-m radio telescope at the Pushchino Radio Astronomy Observatory (Russia) during 1992−2003. The H₂O maser was discovered in May 1992 (Pashchenko 1992) during a survey of IRAS sources associated with dense cold clouds with bipolar molecular outflows. The H₂O spectrum contains many emission features, suggesting the fragmentation of the envelope around a young star. The star has a low peculiar velocity relative to the CO molecular cloud ($\sim$2.2 km s^{-1}). We found a cyclic variability of the total maser flux with a period from 1.8 to 3.1 yr. © *2003 MAIK "Nauka/Interperiodica"*.

Key words: *interstellar medium, gaseous nebulae, stars—structure and evolution.*

INTRODUCTION

H₂O and OH masers in regions of active star formation can be associated with compact far-infrared sources (Wynn-Williams *et al.* 1972; Evans *et al.* 1979) located in dense cold clouds. Because of the strong absorption in the cloud, the protostar is unobservable in the visible wavelength range. The stellar emission is absorbed by gas and dust and is reradiated in the far infrared with a thermal spectrum. Thus, for example, the source IRAS 06308+0402 radiates intensely in the far infrared, where its flux density is 602 Jy at 80 μm and 948 Jy at 100 μm. The molecular cloud associated with it has a temperature of $\sim$40 K and is observed in the CO radio line at a radial velocity of 15.8 km s^{-1} (Wilking *et al.* 1989). There is weak emission at 2 and 6 cm (Wilking *et al.* 1989). The distance to IRAS 06308+0402 is estimated to be 1.6 kpc (Turner 1976). The source is associated with a bipolar outflow. All of the above facts suggest that IRAS 06308+0402 is very young object.

An attempt to detect the H₂O maser emission was made by Palla *et al.* (1991). They found no emission in the 1.35-cm line with a flux higher than 3.5 Jy. In May 1992, an H₂O maser emission source that coincided in position with IRAS 06308+0402 was detected during a survey of IRAS sources (Pashchenko

1992). Its spectrum consisted of two emission peaks. The main peak had a radial velocity of 17 km s^{-1} and a flux density of about 50 Jy. This maser has been monitored in the 1.35-cm line since 1992. Xiang and Turner (1995) also observed the H₂O maser emission. Their measurements showed that the maser is at an angular distance of 1′ from IRAS 06308+0402 and is associated with a bipolar molecular outflow.

In this paper, we present the results of our monitoring of the H₂O maser toward IRAS 06308+0402 during 1992−2003.

OBSERVATIONS AND DATA PRESENTATION

We observed the H₂O maser emission toward the source IRAS 06308+0402 ($\alpha_{1950} = 06^h30^m52\overset{s}{.}7$, $\delta_{1950} = 4°02'27''$) with the 22-m RT-22 (Pushchino) radio telescope from May 1992 through January 2003. The mean interval between our observations was about 2.2 months. The noise temperature of the system with a cooled input FET amplifier was 150−230 K. In 2000, the radiometer was upgraded, which allowed us to decrease the system noise temperature to 100−130 K. We analyzed the signal spectrum with 96-channel and, from July 1997 onward, 128-channel filter-bank spectrum analyzers with a resolution of 7.5 kHz (0.101 km s^{-1} in radial velocity in the 1.35-cm line). For a point source with unpolarized emission, an antenna temperature of 1 K corresponds

*E-mail: `pachenko@sai.msu.ru`

**E-mail: `lekht@sai.msu.ru;lekht@inaoep.mx`
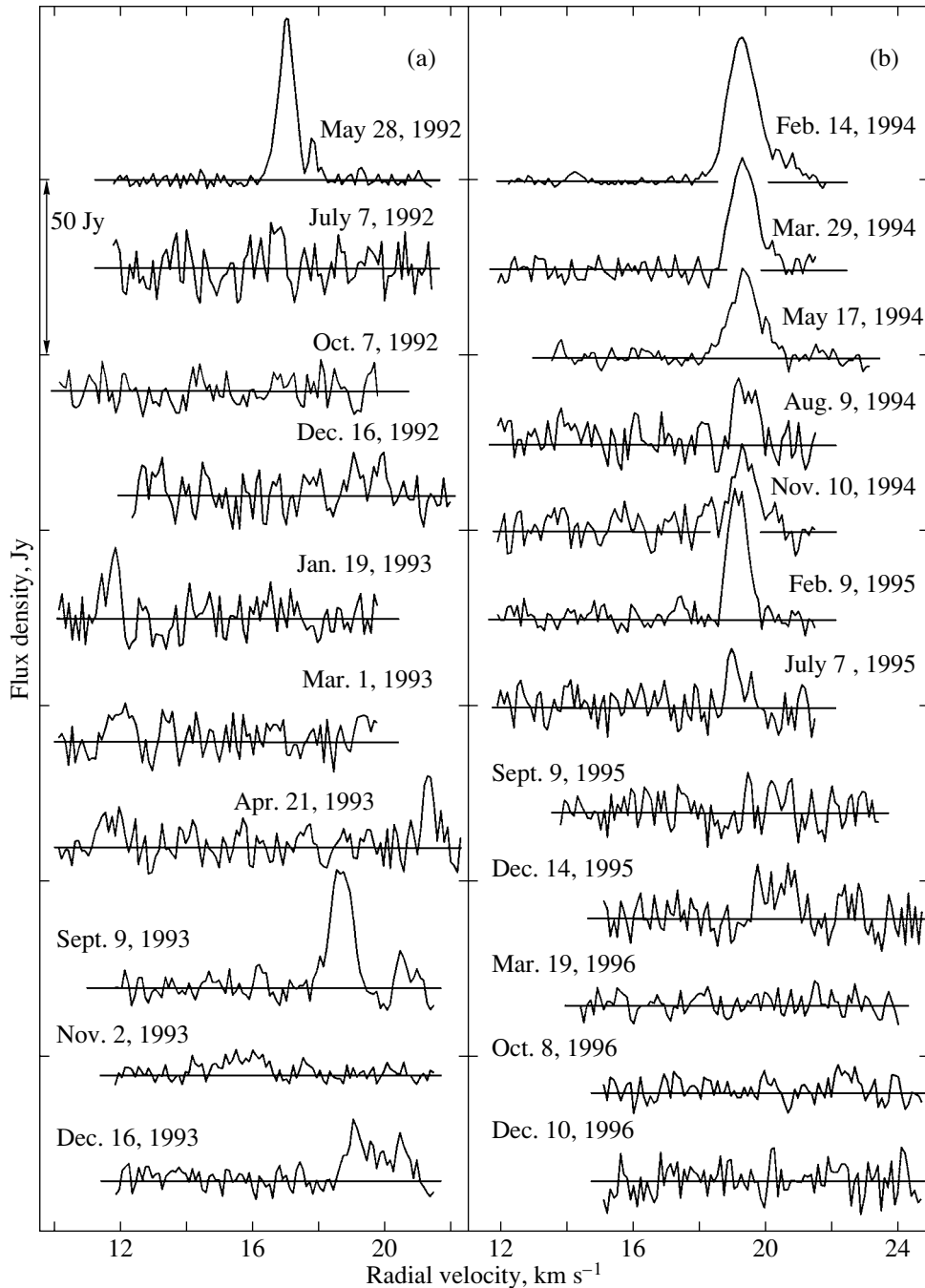
Fig. 1. Spectra of the H_2O maser emission toward the infrared source IRAS 06308+0402 obtained in 1992−2003. The vertical arrows indicate the scale in janskys. Velocity with respect to the Local Standard of Rest is along the horizontal axis.

to a flux density of 25 Jy. Figure 1 presents a catalog of H_2O spectra. The spectra with the smallest fluctuations are averages of several records obtained during one observing day. For the spectra of Figs. 1b and 1c, we performed averaging over separate time intervals and over the entire period 1997−2003. The results of this procedure are shown in Fig. 2. The arrows indicate the components that we managed to separate in the average spectra. In addition, we

separated individual spectral components in the single spectra of the period 1992−1996. The H_2O spectra in the form of individual components and their evolution are presented in Fig. 3. We see that they are distributed in the spectrum more or less uniformly over the range 11.7−24 km s^{-1}, while the strongest emission appeared in the central part of this range, at radial velocities of 17 and 18.6−19.2 km s^{-1}. In
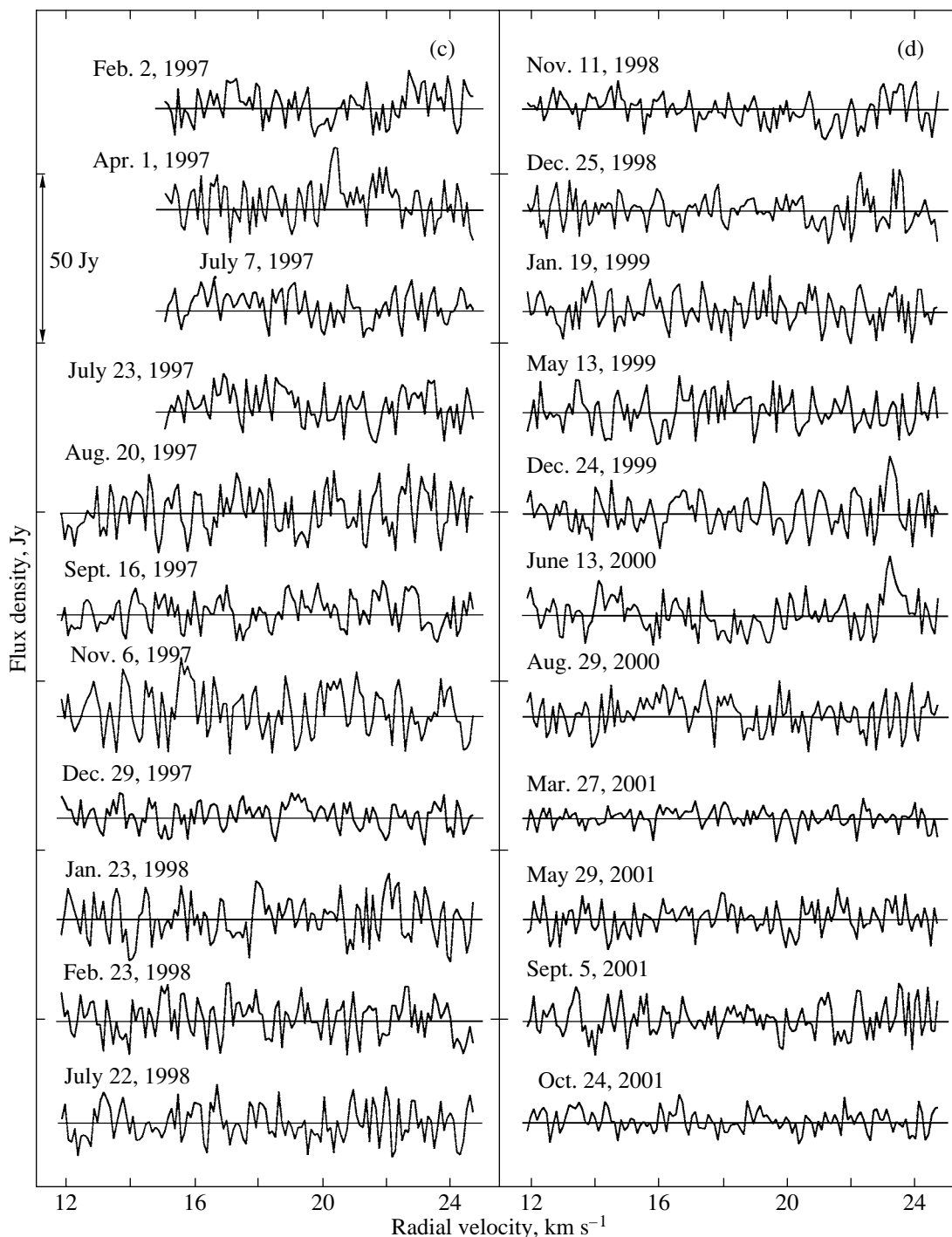
Fig. 1. (Contd.)

searching for possible cyclic variability of the maser, we calculated the total flux for each spectrum. The difficulty lay in the fact that the signal mainly had not exceeded the noise fluctuation level since the mid-1998. Therefore, determining the zero signal level in each spectrum was of great importance. The total-flux variability is shown in Fig. 4.

DISCUSSION

The water-vapor maser toward IRAS 06308+0402 became the first source associated with a dense cold cloud for which long-term monitoring was carried out. The absence of observations with high angular resolution increased the value of the monitoring results. We got an opportunity to construct a model
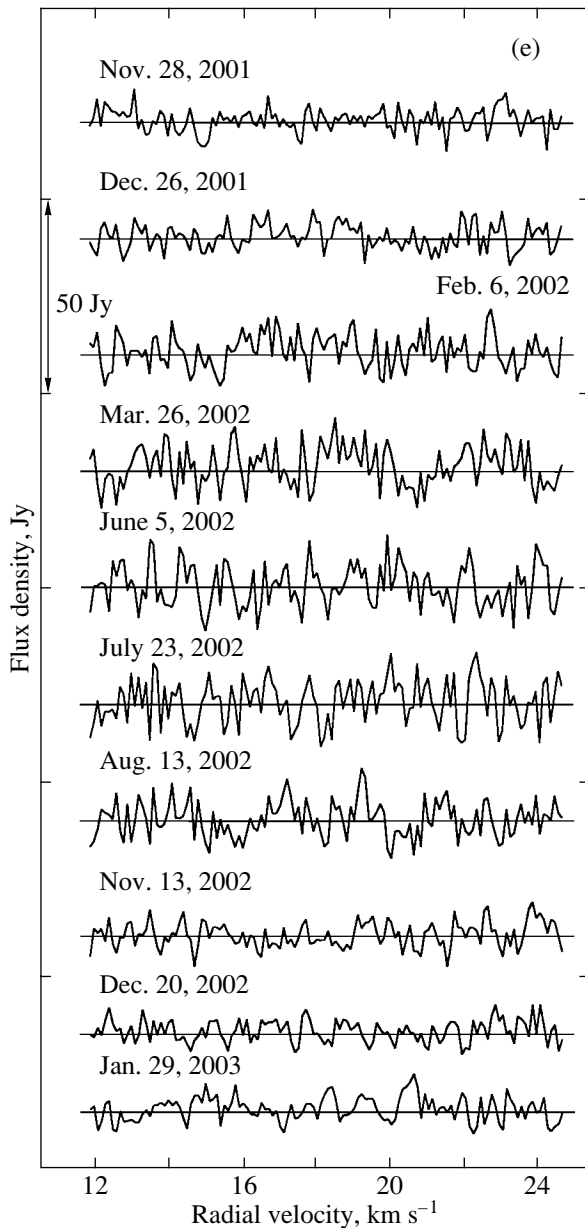
Fig. 1. (Contd.)

Fig. 2. (a) Average H_2O spectra for various time intervals; (b) Average spectrum for the observing period 1997−2003.

Analysis of the Catalog of H_2O Spectra

Our monitoring of the H_2O maser in IRAS 06308+ 0402 shows that the maser emission is mainly weak. We observed three outbursts at different radial velocities. The first outburst was associated with the detection of the maser (May 1992). The flux density at $V_{LSR} = 17$ km s^{-1} was about 50 Jy. This was apparently a short-duration outburst, because in July 1992 we observed a weaker emission with a flux density of less than 10 Jy ($V_{LSR} = 16.7$ km s^{-1}). We

may have observed this emission already during its decline, while at the maximum, its flux density was much higher than 50 Jy. The second, also short-duration outburst took place in 1993 ($F = 33$ Jy, $V_{LSR} = 18.7$ km s^{-1}). Only the third outburst may be considered as a period of higher activity of the entire maser, which lasted from December 1993 until July 1995. The range of radial velocities of the emission was 18−21 km s^{-1}. A weaker emission was observed at the spectrum edges between the first and the second outbursts.

Structure of the H_2O Spectra

Of great importance in constructing a maser model is the study of spectral structure, i.e., the separation of individual spectral components. Each component is identified with a separate maser spot. During the highest maser activity (1992−1996), the
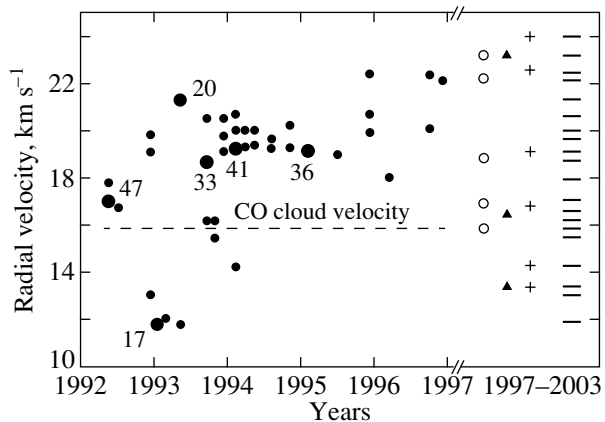
Fig. 3. The H$_2$O spectra presented in the form of individual components (filled circles). The large circles and numbers near them denote the flux peaks and flux values, respectively. The open circles, triangles, and pluses indicate the components separated from the average spectra for the intervals 1997−1999, 2000−2001, and 2002−2003, respectively. The horizontal bars on the right indicate the positions of all of the detected emission features. The dashed line indicates the radial velocity of the CO molecular cloud (Wilking *et al.* 1989).

Fig. 4. Variability of the total H$_2$O maser flux from the source IRAS 06308+0402. The dashed line represents a polynomial fit, and the arrows indicate the extrema (maxima). The dashed arrow indicates the presumed position of the peak of the first outburst.

decomposition of the spectra into separate components involved no special difficulties. A different picture has been observed since 1997. This has been a period of weak maser activity. For this reason, we averaged the spectra for two time intervals: 1997−1999 and 2000−2003 (Fig. 2). Our averaging revealed emission features as weak as 0.5−0.7 Jy. The fact that we managed to detect such features suggests their long lifetime as maser sources. Figure 3 presents the spectra in the form of separate components for the period 1992−1996. For the period 1997−2003, the components obtained from the average spectra are shown in the figure. There is a spread in radial velocities from spectrum to spectrum. Therefore, we took an interval of about 0.2 km s^{-1} as a criterion for the separated component belonging to the same maser spot. We thus identified 20 features that can be associated with maser spots. They are shown in the right part of Fig. 3. We observe a more or less uniform distribution of the components in the H$_2$O spectrum. The absence of a triplet spectral structure may be an argument for the maser model in the form of an expanding shell.

Cyclic Activity of the H₂O Maser

To estimate the activity of the maser as a whole, we used such a maser emission parameter as the total flux. As was shown above, the H$_2$O spectra have consisted of a large number of weak emission features since 1997. This factor can give a large error when determining the total flux. To avoid this, it was

necessary to adjust the zero line of each spectrum. After this adjustment, we constructed the curve of the total flux shown in Fig. 4. The dashed line represents the polynomial fit that allowed us to determine the positions of the peaks. Four peaks are observed. As we have noted above, in February 1990, Palla *et al.* (1992) observed no emission stronger than 3.5 Jy. The maser was detected in May 1992 (Pashchenko 1992). Slightly earlier (April 1992), it was observed by Xiang and Turner (1995), but their results were published only in 1995. The flux density of the main feature was 12 Jy. The emission in 1992 had a distinct outburst pattern with a large flux variation during a short time. It is virtually impossible to determine the exact position of the peak of this outburst. We can say only that it occurred in May 1992.

Thus, the maser variability is cyclic in pattern with periods of ∼2.1, 3.1, 2.7, and 1.8 yr. This cyclicity can reflect the quasi-periodic pattern of variability of a young star at the stage of its formation. The derived variability periods are several times shorter than those found for masers in star-forming regions associated with ordinary molecular clouds (see, e.g., Lekht 1996).

A Model of the H₂O Maser in IRAS 06308+0402

To have a rough pattern of distribution of maser spots on the shell surrounding the star, we constructed the frequency distribution of spectral components in radial velocities (Fig. 5). We counted the number of observed components in all of the spectra, i.e., each component was counted as many times as it was observed. Thus, this statistic included both the components themselves and the probabilities of
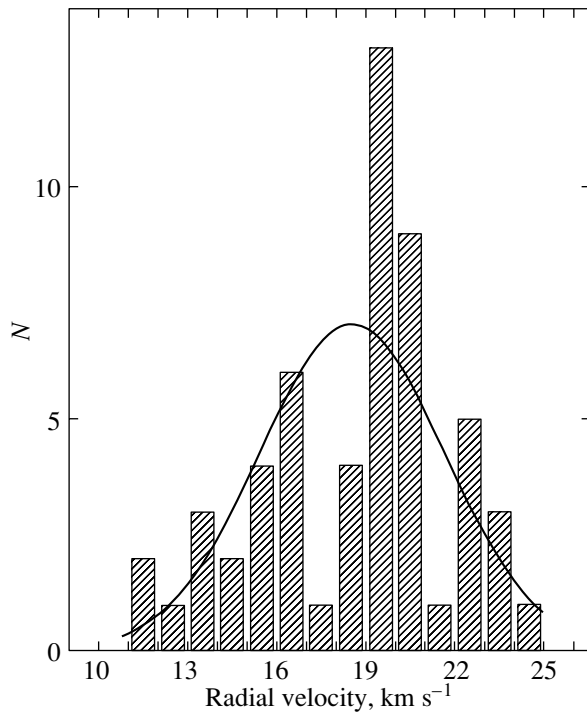
Fig. 5. Frequency distribution (histogram) of spectral components in radial velocities. The solid line represents a Gaussian fit.

their occurrence. Such studies of masers associated with star-forming regions were first carried out by Lekht *et al.* (1995) and Lekht (1995). The histograms of spectral components were obtained for the H_2O masers in W31A, W75S, and W75N. Our histogram is most similar to the histogram for W31A. There is also a difference: a deep dip at velocities of $17-19$ km s^{-1} and a large rise at $19-21$ km/s, which is shifted by $\sim$1.5 km s^{-1} relative to the distribution center. The rise can be attributed to a bipolar outflow (Xiang and Turner 1995) if it is not oriented in the plane of the sky, which is most likely.

As a model, we may consider an expanding shell on which maser spots are located. In addition, there is a bipolar mass outflow from the star, which appreciably affects the structure of the H_2O spectra.

## MAIN RESULTS

(1) We have presented a catalog of H_2O maser spectra in the 1.35-cm line toward the infrared source IRAS 06308+0402 for the period $1992-2003$.

(2) We have identified 20 individual spectral components; this can be an argument for the model of an unhomogeneous (fragmented) shell around a young star.

(3) During our 11 years of monitoring, we observed no strong outbursts of H_2O maser emission typical of masers in star-forming regions. The outburst in May 1992, when a large flux variation took place over one month, may be considered an exception.

(4) The radial velocity of the most active part of the H_2O spectrum is about 18 km s^{-1} and is shifted by $\sim$2.2 km s^{-1} relative to the velocity of the CO molecular cloud. This shift may result from a peculiar, low motion of the H_2O maser in the cloud. The radial-velocity dispersion of the maser emission is at least 12 km s^{-1} ($11.7-24$ km s^{-1}). The emission features are uniformly distributed in the spectrum, and no triplet structure is traceable; this may be an argument for the model of an expanding shell.

(5) We found a cyclic variability of the total H_2O flux with a period from 1.8 to 3.1 yr. This value is several times lower than that for masers associated with ordinary (not cold) clouds.

ACKNOWLEDGMENTS

REFERENCES

1. E. E. Lekht, E. Mendoza-Torres, and R. L. Sorochenko, Astrophys. J. **443**, 222 (1995).
2. E. E. Lekht, Astron. Zh. **72**, 31 (1995) [Astron. Rep. **39**, 27 (1995)].
3. E. E. Lekht, Astron. Zh. **73**, 695 (1996) [Astron. Rep. **40**, 632 (1996)].
4. F. Palla, J. Brand, R. Cesaroni, *et al.*, Astron. Astrophys. **246**, 249 (1991).
5. M. I. Pashchenko, Astron. Tsirk. **1553**, 27 (1992).
6. D. G. Turner, Astrophys. J. **210**, 65 (1976).
7. B. A. Wilking, L. G. Mundy, J. H. Blackwell, and J. E. Howe, Astrophys. J. **345**, 257 (1989).
8. C. G. Wynn-Williams, E. E. Becklin, and G. Neugebauer, Mon. Not. R. Astron. Soc. **160**, 1 (1972).
9. D. Xiang and B. E. Turner, Astrophys. J., Suppl. Ser. **99**, 121 (1995).

Translated by G. Rudnitskiĭ

Magnetic Fields and Rotation of the White Dwarfs 40 Eri B and WD 0009+501

S. N. Fabrika[*], G. G. Valyavin, and T. E. Burlakova

Special Astrophysical Observatory, Russian Academy of Sciences, Nizhnii Arkhyz,
Karachai-Cherkessian Republic, 369167 Russia
Received December 19, 2002; in final form, June 18, 2003

Abstract—We describe the results of our magnetometric monitoring of two white dwarfs: 40 Eri B and WD 0009+501. We found periodic variations in the longitudinal magnetic field of 40 Eri B. The field variability with an amplitude of ∼4 kG and a zero mean is discussed in terms of an oblique rotator model. The rotation period is ∼5 h 17 min, but there is another period of 2 h 25 min that may be related to nondipolar field components. The published projected rotational velocities of 40 Eri B measured from a narrow non-LTE Hα peak ($V \sin i \lesssim 8$ km s^{-1}) are in good agreement with our measurements of the magnetic field and the rotation period. The combined effect of magnetic and rotational broadening of the central Hα component constrains the rotation period, $P \gtrsim 5.2$ h. We discovered the rotation period (1.83 h) of the magnetic white dwarf WD 0009+501. The period was found from the periodically varying magnetic field of the star with a mean $\langle B_{\rm e} \rangle = -42.3 \pm 5.4$ kG and a half-amplitude of 32.0 ± 6.8 kG. © *2003 MAIK "Nauka/Interperiodica"*.

Key words: *white dwarfs, magnetic fields, rotation periods.*

INTRODUCTION

White dwarfs are evolutionary products of intermediate-mass stars. These stars evolve without catastrophic processes, and their observational parameters are directly related to the physical characteristics of the cores of red giants. A single degenerate star cools down on time scales from several hundred million to several billion years (Mestel 1952). The magnetic fields of these stars are assumed to evolve (weaken) on time scales on the order of several billion years as well (Wendell *et al.* 1987), although currently available observational data (Fabrika and Valyavin 1999a; Valyavin and Fabrika 1999; Liebert *et al.* 2003) show that the magnetic fields of white dwarfs probably evolve much faster. The remaining observed physical properties of white dwarfs, including their rotation periods, are virtually unchanged (if the white dwarf is not a member of a close binary system) throughout their lifetimes, beginning with their formation from giant stars. All these facts give a unique opportunity to statistically compare the properties of progenitor stars with the properties of their evolutionary products. For example, the magnetic-field distribution of white dwarfs, or the magnetic field–rotation period diagrams compared to those for main-sequence stars, would allow their stellar evolution scenarios to be reconstructed. A comparative analysis makes it possible to determine the fractions of angular-momentum and magnetic-moment losses for stars at the stage of core degeneracy and the mass losses of giant stars. Analysis of the information obtained from white-dwarf observations provides insight into the evolution of their progenitor stars. Thus, observational data on the magnetic fields and rotation periods of white dwarfs are of great importance.

The rotation periods of white dwarfs, if no magnetic field is detected on the star, are very difficult to measure directly. These periods can only be estimated statistically from the spectroscopic measurements of the projected rotational velocities $V \sin i$, where V is the linear equatorial rotational velocity of the stellar surface, and i is the inclination of the rotation axis to the line of sight. Such studies (Pilachowski and Milkey 1987; Koester and Herrero 1988; Koester *et al.* 1998) show that the overwhelming majority of isolated white dwarfs have relatively low rotational velocities (less than 20 km s^{-1}). The rotational velocities of main-sequence stars with masses $1.5 < M_\odot < 8$ (from which white dwarfs are formed) range from 10 to 200 km s^{-1}. If angular momentum is conserved, then these stars must rotate with velocities >1000 km s^{-1} as they collapse into white dwarfs. Thus, there is the problem of angular-momentum losses during the evolution of a star into a white dwarf.
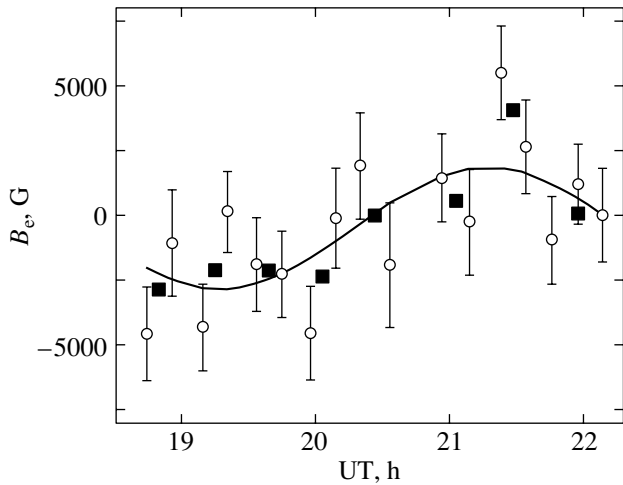
[*]E-mail: `fabrika@sao.ru`

Fig. 1. The time series of magnetic measurements for 40 Eri B obtained with MSS on December 9, 1995. The average values are indicated by solid squares.

The rotation periods can be independently determined by measuring the magnetic fields of white dwarfs. The nonuniform magnetic-field distribution over the stellar surface allows the rotation periods of stars to be directly measured by studying the magnetic-field variability. Schmidt and Norsworthy (1991) showed that magnetic white dwarfs mostly rotate with periods from several hours to several tens of days. These periods correspond to the above estimates of the rotational velocities for white dwarfs. Schmidt and Norsworthy (1991) also constructed a magnetic field−rotation period diagram for white dwarfs, in which this relationship was shown to be ambiguous and complex. Unfortunately, the statistics of measured rotation periods and magnetic fields for white dwarfs is very poor, and further magnetic measurements are required.

In this paper, we analyze our measurements of the magnetic fields and rotation periods for two white dwarfs: 40 Eri B ($V = 9^m5$) and WD 0009+501 ($V = 14^m4$).

OBSERVATIONS

We observed the white dwarfs 40 Eri B and WD 0009+501 with the 6-m BTA telescope as part of our program of research on the magnetism of white dwarfs (see, e.g., Fabrika *et al.* 2000). The observations and subsequent analysis of the circular polarization were carried out by using the standard BTA spectrographs: a high-resolution main stellar spectrograph (MSS) (Najdenov and Panchuk 1996) with a spectral resolution $R = 15\,000$ and a moderate-resolution SP-124 spectrograph (Neizvestnyǐ *et al.* 1998; Bychkov *et al.* 2000) with a spectral resolution $R = 2000$. Each CCD image in this method of

observations simultaneously contains two spectra of opposite circular polarizations split by the analyzer. The magnetic field can be determined by analyzing the difference between the positions of the same spectral lines in the spectra of opposite circular polarizations. In this way, we can determine only the longitudinal magnetic field integrated over the stellar disk.

We carried out magnetic measurements of the brightest white dwarf 40 Eri B with MSS on September 12 and 14 and December 9, 1995. The total observing time on these dates was 19, 81, and 215 min, respectively. The spectroscopy with a typical time resolution of 3−5 min near the Hα line, was aimed at determining possible magnetic-field variation due to the rotation of this white dwarf, and at obtaining highly accurate estimates of the mean magnetic field in the total spectrum. The Zeeman shift of the central narrow non-LTE Hα profile (Pilachowski and Milkey 1987) was measured. Polarization observations of this profile provide the highest accuracy for measuring the magnetic fields on hot DA white dwarfs (Valyavin *et al.* 1997; Fabrika *et al.* 2000). In our observations of 40 Eri B, the expected accuracy of measuring the magnetic field in the Hα line from a spectrum with a signal-to-noise ratio of ~100 was several hundred gauss (Valyavin *et al.* 1997).

We observed 40 Eri B with SP-124 on January 25, 27, and 28, 1999 (referred to below as the first, second, and third nights, respectively). The spectral range covered the Hα and Hβ lines. We obtained a total of about 60 Zeeman images, each with an exposure time of 5 min. In general, the observations lasted for 70, 175, and 192 min on the first, second, and third nights, respectively.

We carried out the spectroscopic observations of the white dwarf WD 0009+501 on September 2, 1999, in the same mode of Zeeman spectroscopy with short exposures, using the SP-124 spectrograph (Valyavin *et al.* 2003).

Since the technique for magnetic measurements of white dwarfs with these instruments was described in detail by Valyavin *et al.* (1997, 2003) and Fabrika *et al.* (2000), we do not discuss our observations in detail below. In this paper, we consider it important to shift the emphasis toward analyzing the results.

RESULTS

40 Eri B

MSS data. The observations of September 14, 1995, revealed a statistically insignificant longitudinal magnetic field $B_e = 0.5 \pm 0.37$ kG in the total spectrum (the observing time was 81 min) for 40 Eri B (Fabrika *et al.* 2000). Note that during

the observations of September 12 and 14, 1995, we knew nothing about the magnetic-field strength of 40 Eri B or its probable rotation period. In addition, it was necessary at that time to test the efficiency of our observing technique in magnetic measurements of white dwarfs. We carried out test observations on these dates with different exposure times from 20 to 3 min. These observations showed the high efficiency of the technique.

In another series of observations on December 9, 1995, carried out with short exposures, we found four-hour sinusoidal variations in the longitudinal magnetic field of the star over the 215 min of our observations (see also Fabrika and Valyavin 1999b). These data are shown in Fig. 1. They consist of 54 three-minute individual field measurements (with a signal-to-noise ratio of about 20−30 in each individual spectrum) averaged over three or four adjacent measurements. Figure 1 shows 17 averaged measurements (open circles) equivalent to exposure times of 11−14 min, corrected for the dead time required to read out the CCD detector. The systematic (1σ) errors were determined by averaging the individual measurements. These data are also given in Table 1, where the time corresponds to the beginning of the exposure.

The observed trend in the variations of the longitudinal magnetic field B_e in Fig. 1 is best fit by a periodic function $B_e = A + B\cos(2\pi t/P + \phi)$ with a statistically insignificant mean of $A = -510 \pm 520$ G, a half-amplitude $B = 2300 \pm 700$ G, and a period $P = 4$ h. The significance of the half-amplitude B exceeds 3σ. The magnetic-field strengths estimated at the maximum and minimum of the curve in Fig. 1 are 1.8 ± 0.7 and -2.8 ± 0.7 kG, respectively.

In this case, we cannot say that we measured the rotation period of 40 Eri B, because the accuracy of this estimate $(P \sim 4\,\mathrm{h})$ is very low. For the same reason, we do not show the measurements of September 1995 in Fig. 1; they can be easily reconciled with the derived sinusoidal curve without increasing its significance.

Near the maximum of the curve in Fig. 1, the difference between several neighboring points (open circles in the figure) is statistically significant. Situations where the results of polarimetric observations differ severalfold in their statistical errors often arise in such observations. These differences are generally attributable to fluctuations in weather conditions or unnoticed cosmic-ray particle hits in narrow line cores. Figure 1 shows our additional field estimates (filled squares) obtained by a pairwise averaging of the magnetic-field strengths at neighboring points of the series under discussion (the extreme estimate in the right-hand part of the figure was obtained by averaging the last three values). In general, these estimates

are consistent with the sinusoidal fit with the period in question. Naturally, however, longer periods or even a linear trend are possible.

Analysis of the total spectra obtained from the series in Fig. 1 yields a statistically significant magnetic-field strength. For example, the polarization spectrum obtained by averaging the individual spectra (see Valyavin *et al.* 2003) between 21 and 22 h UT shows that the magnetic splitting in the Hα core is 3.7 ± 0.5 kG. On the other hand, the shift of the telluric water absorption lines detected in the same spectrum near Hα is 0 ± 1.5 kG, in units of magnetic field.

Thus, we see that a magnetic field has been detected on 40 Eri B, and that it varies on a characteristic time scale of several hours. However, the results of our MSS observations for 40 Eri B cannot be unequivocally interpreted as four-hour periodic magnetic-field variations. The observing time is comparable to the time scale of the field variability, and the scatter of individual data points is large; we can only say that the time scale of the magnetic-field variability for 40 Eri B is several hours.

SP-124 data. The standard procedure for magnetic measurements includes observations at various orientations of a quarter-wave plate (see, e.g., Monin

Table 1. The MSS magnetic measurements of 40 Eri B on September 9, 1995

JD 2450000+	Exposure, min	B_e kG	σ, kG
61.281	11	−4.5	1.8
61.289	11	−1.0	2.0
61.299	11	−4.3	1.6
61.306	12	0.1	1.5
61.315	11	−1.9	1.8
61.323	12	−2.2	1.6
61.332	11	−4.5	1.8
61.340	11	−0.1	1.9
61.347	11	1.9	2.0
61.357	11	−1.9	2.4
61.373	11	1.4	1.6
61.381	13	−0.2	2.0
61.391	11	5.5	1.8
61.399	12	2.6	1.8
61.407	11	−0.9	1.6
61.415	14	1.1	1.5
61.423	12	0.0	1.8

et al. 2002; Valyavin *et al.* 2003). This procedure is designed to eliminate the systematic errors related to instrumental polarization (slit curvature, inaccurate alignment of the polarization optics, etc.). The systematic effects give rise to an instrumental shift between the positions of the same line in the spectra of opposite circular polarizations split by the analyzer, i.e., to a false magnetic field. Rotation of the polarization analyzer (the quarter-wave plate) completely removes the instrumental effects. In this technique, the spectra of opposite polarizations are projected onto the same place of the CCD detector, which rules out the appearance of new instrumental effects.

Nevertheless, the standard methods are not enough to study the weak and *variable* magnetic field of 40 Eri B. The MSS observations show that 40 Eri B has a variable magnetic field. Analysis of the star's varying magnetic field can lead to undersubtraction of the instrumental circular polarization in the line cores, because the magnetic field can change between successive rotations of the analyzer. For this reason, before and after the observations of 40 Eri B, we additionally observed standard stars with a zero magnetic field. The observing conditions for the standard stars and the white dwarf were identical.

The bright stars ϵ Tau, α Cep, 40 Eri A, and the star located $19'$ north of 40 Eri B were used as the zero-field standards. For the first G9.5 III star, the magnetic field (the line positions) were measured by cross correlation in a 100-Å region near Hα and Hβ. The other standard stars have approximately the same spectral type as the object under study; i.e., their spectra exhibit prominent hydrogen lines. In their spectra, we measured the line shifts directly in the hydrogen lines.

The star ϵ Tau has a zero magnetic field, less than 10 G (Smirnov *et al.* 2003). The magnetic field of α Cep does not exceed 100 G (Monin *et al.* 2002). There are no magnetic-field data for the remaining standard stars. The probability that a randomly chosen star will be magnetic, with a magnetic field stronger than 1 kG, is very low (Monin *et al.* 2002). In particular, the probability that a significant magnetic field is simultaneously present on two stars (40 Eri A and the anonymous star) is negligible. Since zero control using these stars is supplementary to our standard analyzer-rotation procedure, we believe that this control is definitely better than 1 kG. Our processing of the spectra for these four stars using the standard technique (Fabrika *et al.* 2000) showed that their magnetic fields were actually close to zero. Finally, the magnetic measurements for 40 Eri B were corrected by linearly interpolated measurements of the instrumental shifts.

In our observations of 40 Eri B, we measured two hydrogen lines, Hα and Hβ. The Zeeman splitting in the line cores was determined from the positions of the hydrogen-line centers in the spectra of opposite circular polarizations. The positions of the line centers were determined by a Gauss analysis. For our measurements, we selected only the best-quality spectra (S/N $> 80-90$) and only those in which the line cores were not distorted by cosmic-ray particle hits. The particle hits in the line centers with large intensity gradients cannot be removed.

Analysis of the power spectrum for the data of all three nights revealed sinusoidal signals that corresponded to several periods ranging from 2 to 5 h. Figure 2 illustrates our periodogram analysis of the temporal behavior of the longitudinal magnetic field on 40 Eri B measured from the Hα core. Figure 3 illustrates our analysis of the Hβ measurements. We performed the periodogram analysis by using the combined results of our observations on all three nights. The figures show, in arbitrary units, (a) the power spectra for the time series of measurements, (b) the spectral windows of observations, and (c) the final power spectra of our observations, corrected for the spectral window [the terminology and the theory for analyzing time series were described in detail by Terebizh (1992)]. Frequencies (in inverse days) are along the horizontal axis. The magnetic measurements for the star in Hα are most accurate, because its Zeeman splitting factor is larger than that for Hβ (Landstreet 1982). In addition, our spectra near Hα are better in quality than those near Hβ. The periodogram for the Hα measurements (Fig. 2) exhibits a statistically significant periodic signal at a frequency of about 4.54 inverse days, which corresponds to a period of $5^\mathrm{h}17^\mathrm{m}$. This signal with a lower significance is also present in the periodogram for the Hβ measurements. As can be seen, other peaks are also present in both periodograms. Some of these peaks are not independent; they result from the interference of the real signal at the observational data sampling. Others are random in nature.

Assuming the model of an axisymmetric dipole magnetic field for the white dwarf under consideration, we performed an additional harmonic analysis to find only sinusoidal variations in its magnetic field, due to rotation. This analysis also indicates that the best case in both lines is realized with a period of $5^\mathrm{h}17^\mathrm{m}$. However, our analysis of the Hβ line revealed a second period of sinusoidal magnetic-field variability, $2^\mathrm{h}25^\mathrm{m}$.

The phase magnetic curves with a period of $5^\mathrm{h}17^\mathrm{m}$ for both lines are shown in Fig. 4. The results of our Hα and Hβ magnetic measurements are also presented in Table 2. We estimated the accuracy of measuring the magnetic field in individual spectra by
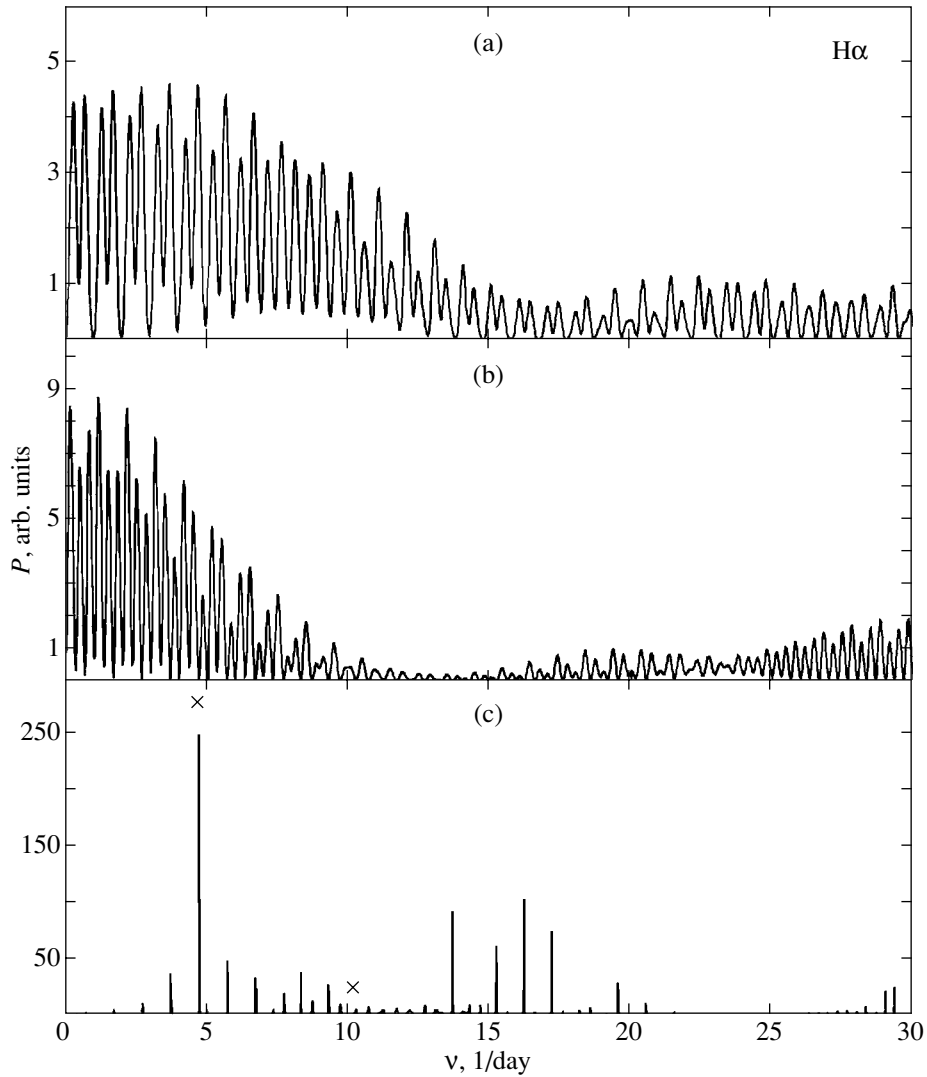
Fig. 2. Power spectra P (in arbitrary units) for the time series of magnetic measurements for 40 Eri B using the Hα line: (a) the power spectrum for the original time series; (b) the spectral window; and (c) the power spectrum corrected for the spectral window. Frequencies (in inverse days) are along the horizontal axis. The crosses denote the peaks at the frequencies that correspond to the periods $P = 5^{\rm h}17^{\rm m}$ and $P = 2^{\rm h}25^{\rm m}$.

fitting the line profiles and analyzing the measurement errors (Valyavin *et al.* 1997). The major factor that determines the measurement error of the line shifts is the signal-to-noise ratio in the spectra. In our case, we use spectra of approximately the same quality. On average, the measurement error of the magnetic field for Hα and Hβ is 3 and 7 kG, respectively. Both Hα and Hβ confirm the periodic variations with the period found, but the scatter of data in the Hβ measurements is larger, as would be expected. The individual data are represented by open circles, and the average values in 0.1ϕ-wide phase intervals with rms errors are represented by filled circles. These figures also show a sinusoidal fit to the data in the

form $B_{\rm e} = A + B\sin(2\pi t/P + \phi_0)$. The parameters of the fit with a period of $5^{\rm h}17^{\rm m}$ are

Hα $A = 300 \pm 550$ G $B = 4400 \pm 700$ G,

Hβ $A = 400 \pm 900$ G $B = 4000 \pm 1400$ G.

The periodicity in the field variations with the period $P = 5^{\rm h}17^{\rm m}$ was found with a high probability (more than 95%). The parameters of the fit with a period of $2^{\rm h}25^{\rm m}$ have an appreciably lower significance, particularly for the Hα line.

The previously found (in the MSS observations) four-hour sinusoidal cycle in the magnetic-field variations of 40 Eri B is in better agreement with the five-hour period. The averaged MSS measurements in the Hα line are also shown in Fig. 4. Note that the
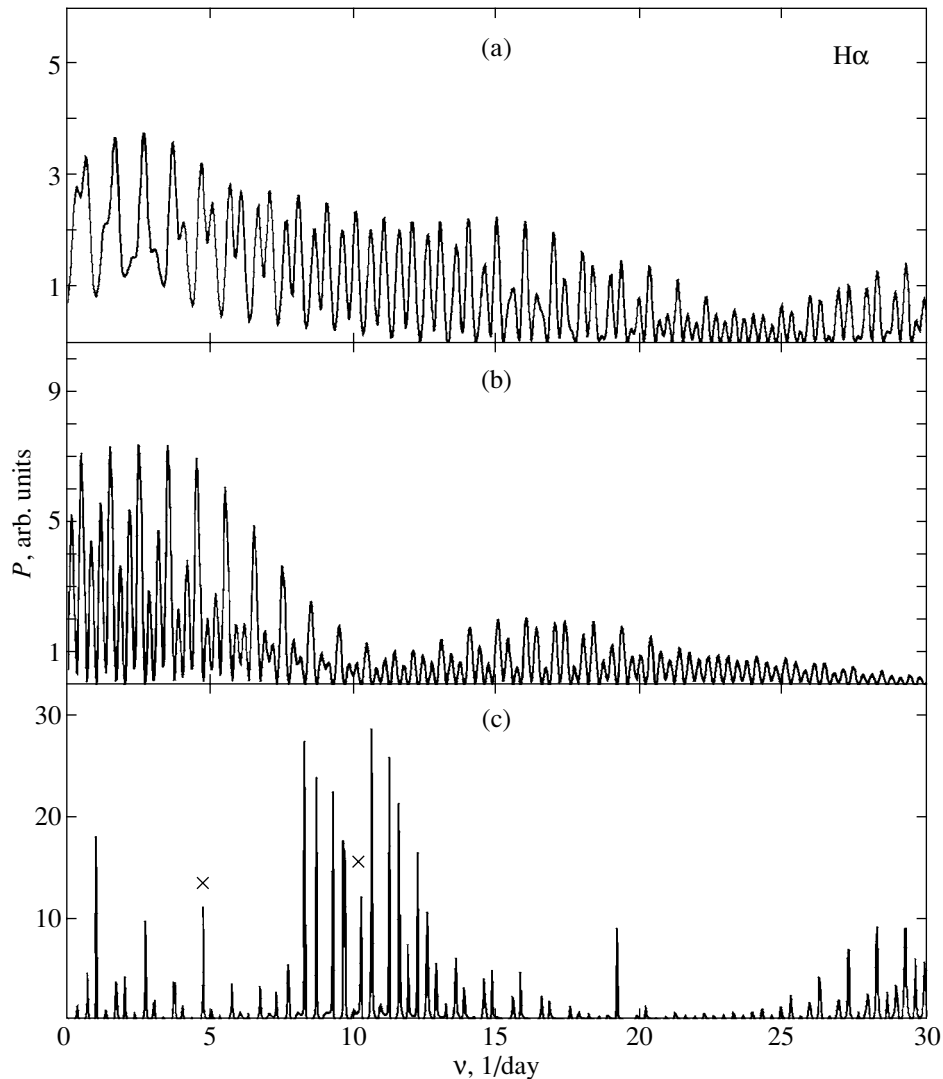
Fig. 3. Power spectra P (in arbitrary units) for the time series of magnetic measurements using the Hβ line. The order of the spectra and the notation are the same as those in Fig. 2.

low accuracy of measuring the field variability period completely rules out the possibility of simultaneously using these data to search for a period. However, the amplitudes of the magnetic-field variations differ in observations with different spectral resolutions (SP-124 and MSS). We discuss the possible causes of this difference in the next section.

It is highly likely that the five-hour period corresponds to the rotation period of the star. The lower significance of the second period ($P = 2^{\mathrm{h}}25^{\mathrm{m}}$) leads us to believe that this period is less likely as the fundamental period, the rotation period of the white dwarf. Nevertheless, we use it in the subsequent discussion, because the magnetic field of 40 Eri B may be nondipolar. In this case, the field behavior over the rotation period could also be more complex in pattern than a simple sine wave. The two-hour period

may then be also real and could represent a higher harmonic in the decomposition of the nondipolar-field behavior over the rotation period. Moreover, this period is close to half the five-hour period, which may be circumstantial evidence for the existence of a quadrupole component. The distribution of points in the phase curves (Fig. 4, Hα) admits this possibility, because an appreciable deviation from the sine wave is observed at certain phases.

The surface magnetic field of 40 Eri B. Based on the Zeeman circular polarization spectra, we measure only the longitudinal magnetic field B_{e} of the star. However, invoking the high-resolution spectroscopy obtained without a polarization analysis, we can impose a constraint on the complete integral of the magnitude of the star's magnetic field (surface field B_{s}). The narrow non-LTE Hα profile in white

dwarfs can be broadened only by rotation and Zeeman splitting. In bright white dwarfs, of which 40 Eri B is one, the accuracy in measuring the width of the central Hα profile is high (Pilachowski and Milkey 1987; Koester and Herrero 1988; Koester *et al.* 1998). It corresponds to a Zeeman line broadening in a magnetic field of ∼10−15 kG. No clear Zeeman splitting in the Hα line was detected for 40 Eri B in any of the cited studies. It thus directly follows that the surface magnetic field of this star is less than 10 kG.

Let us briefly summarize our measurements of the longitudinal magnetic field for 40 Eri B. The half-amplitude of the variability found (B_e^{max}) lies within the range 3000−5000 G, and the mean magnetic field ($\langle B_e \rangle$) is ∼300 ± 500 G. The ratio $B_e^{max}/\langle B_e \rangle$ is found to be high. The orientation of the magnetic field, both the rotation axis (the angle i between the rotation axis and the line of sight) and the symmetry axis of the magnetic field (the angle β between the rotation and magnetic axes), can be inferred from these data (Fig. 4) and the observation regarding the star's surface field. If 40 Eri B has a mainly dipole field, which is the most reasonable assumption for white dwarfs, then the rotation axis has a large inclination to the line of sight, $i \approx 90°$, with a high probability (a large $B_e^{max}/\langle B_e \rangle$). In addition, if the angle i were small, then the inferred longitudinal field $B_e^{max} \approx$ 4000 G would imply a strong surface magnetic field (Stibbs 1950). This field would cause an appreciable broadening of the narrow non-LTE Hα profile, which, in turn, would be revealed with high-resolution spectroscopy.

In other words, it follows from the phase magnetic curve for 40 Eri B (Fig. 4) that the dipole axis is close to the line of sight twice during the rotation period. Therefore, we believe that the inclination of the rotation axis to the line of sight is close to 90°. The star's magnetic dipole axis is also inclined to the rotation axis at an angle close to 90°. The estimates of $i \approx 90°$ and $\beta \approx 90°$ follow from the symmetry of the phase curves relative to zero and from the large ratio $B_e^{max}/\langle B_e \rangle$.

Taking into account the above remarks, we can impose numerical constraints on the surface magnetic field of 40 Eri B. Rotation and a magnetic field simultaneously broaden the central non-LTE Hα profile. A surface magnetic field broadens this profile as $\Delta V_m = 1.84 B_s$ km s^{-1}, where B_s is in kG. The rotational broadening is defined as $\Delta V_{rot} = V_{rot} \sin i = 2\pi R/(P/\sin i)$, where R is the stellar radius, P is the rotation period, and V_{rot} is the equatorial rotational velocity of the star. As a result, the total line broadening is $\Delta V = \sqrt{\Delta V_m^2 + \Delta V_{rot}^2}$.

Table 2. The SP-124 magnetic measurements of 40 Eri B in the Hα and Hβ lines

Hα[a]		Hβ[b]	
JD 2450000+	B_e, kG	JD 2450000+	B_e, kG
1204.228	4.5	1204.228	0.2
1204.233	6.4	1204.233	10.6
1204.237	4.3	1204.245	−7.8
1204.245	3.5	1204.269	5.6
1204.265	3.8	1204.278	−3.6
1204.269	2.2	1206.221	−0.8
1204.274	0.6	1206.231	−0.8
1204.278	7.4	1206.235	6.9
1206.227	−7.1	1206.239	0.3
1206.243	2.9	1206.243	−4.7
1206.249	6.8	1206.249	−1.0
1206.257	3.5	1206.253	5.9
1206.261	0.3	1206.257	−3.1
1206.267	−2.5	1206.261	−2.4
1206.271	2.9	1206.271	7.3
1206.275	−6.1	1206.275	−16.8
1206.280	−0.6	1206.280	10.2
1206.284	−2.5	1206.284	−14.3
1206.287	1.2	1206.291	−3.9
1206.291	0.2	1206.296	−2.6
1206.296	−7.4	1206.300	−7.9
1206.311	−9.0	1206.311	−3.0
1206.314	−6.4	1206.314	−14.4
1206.328	−5.9	1206.318	5.5
1206.332	−1.2	1206.324	6.3
1207.201	−1.5	1206.328	−6.2
1207.207	−3.1	1206.336	0.7
1207.212	−1.2	1207.193	3.6
1207.233	−2.3	1207.197	1.0
1207.244	−3.3	1207.201	−6.1
1207.248	−3.4	1207.207	2.2
1207.261	2.0	1207.212	−8.7
1207.273	2.4	1207.224	0.6
1207.277	−0.4	1207.240	8.8
1207.297	3.7	1207.244	4.3
1207.309	−0.1	1207.248	−2.6
		1207.252	11.3
		1207.256	10.6
		1207.265	6.7
		1207.273	−2.8
		1207.277	10.7

[a] The time of a single exposure is 5 min, and the error of a single measurement is $\sigma(B_e) \approx 3$ kG.
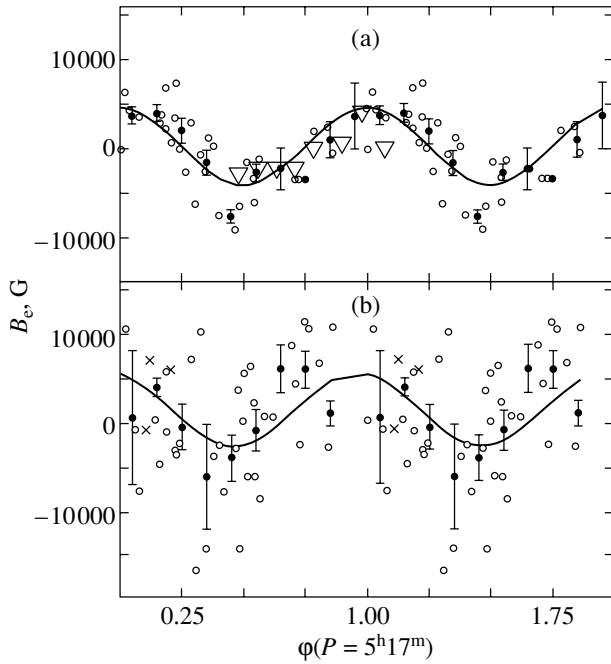[b] The error of a single measurement is $\sigma(B_e) \approx 7$ kG.

Fig. 4. The phase magnetic curves for 40 Eri B with a period $P = 5^{\rm h}17^{\rm m}$ constructed from the (a) Hα (the triangles represent the averaged MSS measurements from Fig. 1) and (b) Hβ measurements. The filled circles indicate the mean measured values and their (1σ) errors in $\Delta\phi = 0.1$ intervals.

Fig. 5. Relationship between the surface magnetic field and the rotation period for 40 Eri B. The curves correspond to the following widths of the narrow non-LTE Hα core: 10 and 6 km s^{-1}. The horizontal line represents the minimum possible surface magnetic field of 3 kG. The domain of admissible rotation periods and surface magnetic fields is located between this line and the $\Delta V = 10$ km s^{-1} curve. The vertical lines represent two rotation periods, $5^{\rm h}17^{\rm m}$ and $2^{\rm h}25^{\rm m}$ (for $i = 90°$).

The most recent spectroscopic studies of the non-LTE Hα profile for 40 Eri B (Heber *et al.* 1997) give a constraint of $\Delta V \lesssim 8$ km s^{-1} at a 3σ confidence level.

The amplitude of the star's longitudinal magnetic field is at a maximum when the line of sight is close to the magnetic dipole axis. At these times, the longitudinal field in the dipole field model is closest in magnitude to the surface magnetic field. Of course, the longitudinal magnetic field is always weaker than the surface field, but for $i \approx 90°$ and $\beta \approx 90°$, the maximum longitudinal field is close in magnitude to the surface field. We assume that $B_{\rm s} \gtrsim B_{\rm e}^{\rm max} \approx 4$ kG. In this case, the broadening of the Hα core by a magnetic field alone is $\Delta V_m \gtrsim 7.4$ km s^{-1}. The purely rotational broadening is found to be $\Delta V_{\rm rot} = \sqrt{\Delta V^2 - \Delta V_m^2} \lesssim 3$ km s^{-1}. Using the constraint $\Delta V \lesssim 8$ km s^{-1} and assuming the radius of 40 Eri B to be $R = 8.98 \times 10^8$ cm (Reid 2000), we obtain a constraint on the rotation period of the white dwarf: $P \gtrsim 5.2$ h. This constraint is in excellent agreement with our rotation period of 40 Eri B, $P = 5^{\rm h}17^{\rm m}$. Note that this result independently confirms that the rotation period of $2^{\rm h}25^{\rm m}$ must be excluded from the analysis.

Figure 5 illustrates the relationship between the surface magnetic field $B_{\rm s}$ and the rotation period

$P/\sin i$ for 40 Eri B. The two curves in this figure correspond to the total (rotational and magnetic) broadening of the non-LTE Hα profile: $\Delta V = 10$ (upper) and 6 km s^{-1} (lower). The domains of admissible $B_{\rm s}$ and $P/\sin i$ lie below the corresponding curves. We chose two values for ΔV by assuming that the magnetic broadening can vary with the rotation phase of the star. Accordingly, the observed surface field can vary by a factor of 1 to 2, which can introduce an uncertainty into the interpretation of the data by Heber *et al.* (1997), $\Delta V \lesssim 8$ km s^{-1}.

The fact that the stellar surface magnetic field varies with the rotation phase is well known for magnetic stars (Mathys *et al.* 1997). The authors analyzed data on 42 well-studied magnetic Ap stars for which they determined the surface magnetic fields with high accuracies. In their study, the ratio $q = \langle B \rangle_{\rm max} / \langle B \rangle_{\rm min}$ of the observed maximum and minimum surface magnetic fields changes from star to star with the above coefficient. To be more precise, about 60% of the stars have $q = 1.0-1.1$; for the remaining stars, this ratio is $1.1-1.9$. Since such a picture must also be observed on white dwarfs and,

accordingly, must contribute to the total variability of ΔV, we took $\Delta V \leq 10$ km s^{-1} as a probable upper limit for the width of the Hα core when the surface magnetic field of 40 Eri B is at a maximum. We chose a lower limit of $\Delta V \leq 6$ km s^{-1} (the phase of minimum surface field) from the same considerations.

The two vertical lines in Fig. 5 represent the periods of $5^\mathrm{h}17^\mathrm{m}$ and $2^\mathrm{h}25^\mathrm{m}$ that we found (in this case, $P/\sin i$ makes sense for $i = 90°$). The horizontal straight line corresponds to a surface magnetic field of 3 kG. This strength is equal to $B_\mathrm{e} - 2\sigma$, which we obtained from the Hα line for the rotation period of $5^\mathrm{h}17^\mathrm{m}$. The domain of admissible surface fields and $P/\sin i$ for 40 Eri B lies below the $\Delta V = 10$ km s^{-1} curve, above the $B_\mathrm{s} = 3$ kG straight line, and to the right of the $P/\sin i = 5^\mathrm{h}17^\mathrm{m}$ straight line. Figure 5 illustrates the fundamental possibility of measuring the rotational velocity, the inclination, and the magnetic-field strength and geometry on normal white dwarfs.

Nevertheless, we believe that further observations are required to confirm the derived rotation period of $5^\mathrm{h}17^\mathrm{m}$ and the magnetic-field strength for 40 Eri B. The half-amplitudes of the longitudinal-field variations, as determined from the MSS (2.3 ± 0.7 kG) and SP-124 (4.4 ± 0.7 kG) data, differ markedly. Since the MSS series is not long enough and, accordingly, since these data may not be accurately fitted by a sine wave, this difference may well be considered to be statistically insignificant. In this sense, the SP-124 observations are much more accurate. However, this difference can also be physical in nature. With MSS, we measured the position of the very center of the Hα line (± 1 Å), i.e., its central non-LTE profile proper. With SP-124, we measured the broader parts of the Hα profile (± 10 Å), i.e., the central part of the Stark line profile. These different parts of the Hα profile are formed at different depths in the atmosphere of the white dwarf. Accordingly, the limb-darkening effect manifests itself differently within them. Therefore, we could expect a different longitudinal magnetic field from these measurements.

WD 0009+501

WD 0009+501 was first discovered as a magnetic star by Schmidt and Smith (1994). In twelve observations on four observing nights, the authors found variations in the longitudinal magnetic field over the range $B_\mathrm{e} = +9$ to -100 kG with errors $\sigma(B_\mathrm{e}) \approx 8{-}15$ kG. Clearly, the observed field varies because of the star's rotation. Schmidt and Smith (1994) found the probable rotation period to be between 2 and 20 h. Analysis of the power spectrum revealed several statistically significant peaks between 2 and
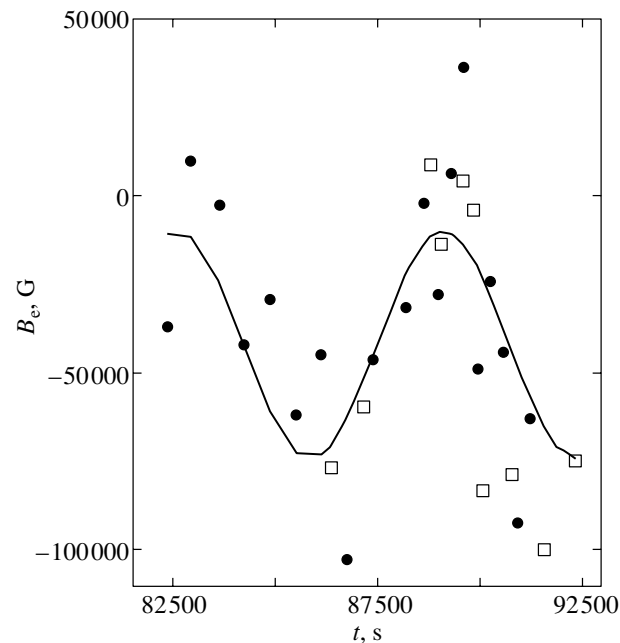
Fig. 6. The Zeeman observations of WD 0009+501 (filled circles). The error of a single measurement is 15–20 kG. The squares represent the observations by Schmidt and Smith (1994).

20 h with shorter periods preferred. No significant variations of the star's magnetic field were found in a pair of spectra separated by 12 min, but clear variations were detected in observations separated by 5 h. Field variations by $\sim$90 kG, which is much larger than the individual error in their measurements, were detected.

Our series of observations for WD 0009+501 consists of 21 sequential Zeeman spectra. The first 10 and the next 11 spectra were taken with 10- and 5-min exposures. Our magnetic measurements confirmed the presence of a periodically varying magnetic field on this star. Our measurements (filled circles) are shown in Fig. 6. As usual, the positions of the Hα line in the spectra of opposite circular polarizations were measured by Gauss analysis. The Hβ measurements are not shown here; they behave in approximately the same way as the Hα measurements, but are less accurate. Our observations span a 2.6 h interval. Magnetic-field variability is clearly seen in Fig. 6.

In general, the exact period cannot be derived from a single series of observations. Based on our data, we can only conclude that the rotation period of WD 0009+501 is about 2 h. However, having added the data by Schmidt and Smith (represented by the squares in Fig. 6), we found the probable rotation period to be 1.83 h. To match our data and the data by Schmidt and Smith, we varied the phase $\Delta\phi$ between the two series of observations. A whole number of periods between the series of observations cannot

be found, because the observations are separated in time by several years. Nevertheless, the phase $\Delta\phi$ in this method can be determined unambiguously; the power spectrum is simultaneously constructed using the entire data set. We cannot yet give a more accurate estimate of the period, because this requires further observations. In general, however, the illustrated curve of the longitudinal magnetic field is described by a sine wave, which is suggestive of the star's dipolar magnetic-field geometry. The mean magnetic field is $\langle B_e \rangle = -42.3 \pm 5.4$ kG, and the variability half-amplitude is 32.0 ± 6.8 G.

DISCUSSION

Our magnetic measurements of 40 Eri B with SP-124 confirm the result obtained in the MSS observations, which revealed magnetic-field variations on this white dwarf with a half-amplitude of 2300 ± 700 G and a period of ≥ 4 h. We gave several arguments that the actual rotation period of 40 Eri B is 5^h17^m. The five-hour phase curve shows that the magnetic curve may not be sinusoidal. An appreciable nondipolar magnetic field of the star may be present. In this case, the existence of a periodic harmonic near 2^h25^m may be real and may show the presence of a quadrupole component. The same can also be said about the magnetic-field structure on WD 0009+501, where we found a period of 1.83 h. In any case, to reach any final conclusions, we need observations with a higher accuracy to study the shapes of the phase magnetic curves in more detail. We plan to continue our observations of white dwarfs with a new polarimeter specially constructed for this task (Naydenov *et al.* 2002). With this instrument, the magnetic-field detection threshold for white dwarfs increases by more than a factor of 3, compared to SP-124.

The results presented here have a record-high accuracy. Our detailed investigation of the magnetic field and rotation of 40 Eri B is an attempt to solve the limiting problem in the studies of magnetism on white dwarfs (Schmidt and Smith 1995; Valyavin *et al.* 2003). The major goal is to study the weakly magnetic part of the magnetic-field function for white dwarfs (Fabrika and Valyavin 1999a). The main difficulties here lie in the fact that most white dwarfs are faint and have weak magnetic fields, and that the number of spectral lines is small. Despite the more than 30-year-long history of studying the magnetic fields of white dwarfs, and all the attempts to find their rotation periods, we know of slightly more than ten stars with more or less reliable estimates of these two parameters (Schmidt and Smith 1995; Wickramasinghe and Ferrario 2000). The number of

estimates should be increased by an order of magnitude to reliably analyze the magnetic field–rotation period diagram for white dwarfs. Here, several paths of development are possible: on the one hand, the development of spectropolarimetry toward a higher efficiency of instruments; and, on the other hand, a search for alternative solutions. One such solution could be an analysis of metal lines in the spectra of white dwarfs for variability.

The presence of heavy elements in the atmospheres of hot, hydrogen-rich DA white dwarfs has been firmly established. Heavy elements have been extensively studied in the ultraviolet and far-ultraviolet spectra of very hot white dwarfs ($T_{\text{eff}} \geq 20000$ K). Absorption lines of carbon, nitrogen, oxygen, silicon, sulfur, phosphorus, iron, and nickel have been found (Sion *et al.* 1992; Barstow *et al.* 1993; Vennes *et al.* 1996). Heavy elements are held in the atmosphere of a hot white dwarf by radiation pressure (Dreizler and Wolf 1999). In contrast, the atmospheres of relatively cool hydrogen DA white dwarfs with temperatures below 20 000 K are incapable of retaining heavy elements due to the insufficient action of radiative forces. Still, a small amount of heavy elements is present in the atmospheres of these stars (Zuckerman and Reid 1998). This amount is assumed to be attributable to interstellar gas accretion.

Previously (Fabrika *et al.* 2000), we suspected the presence of heavy elements in the atmosphere of 40 Eri B. Although we analyzed medium-resolution spectra, we were able to detect traces of several metal lines because of the high spectral data quality (the signal-to-noise ratio in the total spectrum was more than 1000). In this way, we detected traces of lines of heavy elements with residual intensities of less than 0.5% (Fabrika *et al.* 2000; Fabrika 2000). Assuming that gas accretion in the presence of a magnetosphere is anisotropic, we may expect variability of these lines with the rotation period. Thus, the method of studying the variability of weak spectral lines can potentially be used to find the rotation periods of bright white dwarfs.

ACKNOWLEDGMENTS

REFERENCES

1. M. A. Barstow, T. A. Fleming, C. J. Diamond, *et al.*, Mon. Not. R. Astron. Soc. **264**, 16 (1993).

2. V. D. Bychkov, S. N. Fabrika, D. N. Monin, and G. G. Valyavin, *Magnetic Fields of Chemically Peculiar and Related Stars,* Ed. by Yu. V. Glagolevskij and I. I. Romanyuk (Nauka, Moscow, 2000), p. 258 [in Russian].

3. S. Dreizler and B. Wolf, Astron. Astrophys. **348**, 189 (1999).

4. S. N. Fabrika, *Ultraviolet Universe. Proc. of the Conf. on Scientific Aspects of Space UV Observatory SPEKTR-UF,* Ed. by B. M. Shustov and D. S. Wiebe (GEOS, Moscow, 2000), p. 122.

5. S. Fabrika and G. Valyavin, ASP Conf. Ser. **169**, 214 (1999a).

6. S. Fabrika and G. Valyavin, ASP Conf. Ser. **169**, 225 (1999b).

7. S. N. Fabrika, G. G. Valyavin, T. E. Burlakova, *et al.*, *Magnetic Fields of Chemically Peculiar and Related Stars*, Ed. by Yu. V. Glagolevskij and I. I. Romanyuk (Nauka, Moscow, 2000), p. 218.

8. U. Heber, R. Napiwotzki, and I. N. Reid, Astron. Astrophys. **323**, 819 (1997).

9. D. Koester, S. Dreizler, V. Weidemann, and N. F. Allard, Astron. Astrophys. **338**, 612 (1998).

10. D. Koester and A. Herrero, Astrophys. J. **332**, 910 (1988).

11. J. D. Landstreet, Astrophys. J. **258**, 639 (1982).

12. J. Liebert, P. Bergeron, and J. B. Holberg, Astron. J. **125**, 348 (2003).

13. G. Mathys, S. Hubrig, J. D. Landstreet, *et al.*, Astron. Astrophys., Suppl. Ser. **123**, 353 (1997).

14. L. Mestel, Mon. Not. R. Astron. Soc. **112**, 583 (1952).

15. D. N. Monin, S. N. Fabrika, and G. G. Valyavin, Astron. Astrophys. **396**, 131 (2002).

16. I. D. Najdenov and V. E. Panchuk, Bull. Spets. Astrofiz. Obs. **41**, 143 (1996).

17. I. D. Naydenov, G. G. Valyavin, S. N. Fabrika, *et al.*, Bull. Spets. Astrofiz. Obs. **53**, 124 (2002).

18. S. I. Neizvestnyĭ, A. Yu. Knyazev, V. S. Shergin, *et al.,* Report No. 263 (Spec. Astrophys. Obs., Nizhniĭ Arkhyz, 1998).

19. C. A. Pilachowski and R. W. Milkey, Publ. Astron. Soc. Pac. **99**, 836 (1987).

20. I. N. Reid, Astron. J. **111**, 2000 (1996).

21. E. M. Sion, R. C. Bohlin, R. W. Tweedy, and G. P. Vauclar, Astrophys. J. Lett. **391**, L29 (1992).

22. D. Smirnov, S. Lamzin, S. Fabrika, and G. Valyavin, Astron. Astrophys. **401**, 1057 (2003).

23. D. W. N. Stibbs, Mon. Not. R. Astron. Soc. **110**, 395 (1950).

24. V. Yu. Terebizh, *Time Series Analysis in Astrophysics* (Nauka, Moscow, 1992).

25. G. D. Schmidt and J. E. Norsworthy, Astrophys. J. **366**, 270 (1991).

26. G. D. Schmidt and P. S. Smith, Astrophys. J. Lett. **423**, L63 (1994).

27. G. D. Schmidt and P. S. Smith, Astrophys. J. **448**, 305 (1995).

28. G. G. Valyavin, D. N. Monin, T. E. Burlakova, *et al.*, *Stellar Magnetic Fields,* Ed. by Yu. V. Glagolevskij and I. I. Romanyuk (Nauka, Moscow, 1997), p. 127 [in Russian].

29. G. Valyavin and S. Fabrika, ASP Conf. Ser. **169**, 206 (1999).

30. G. G. Valyavin, T. E. Burlakova, and S. N. Fabrika, Astron. Zh. **80**, 638 (2003) [Astron. Rep. **47**, 587 (2003)].

31. S. Vennes, P. Chayer, M. Hurwitz, and S. Bowyer, Astrophys. J. **468**, 898 (1996).

32. C. E. Wendell, H. M. Van Horn, and D. Sargent, Astrophys. J. **313**, 284 (1987).

33. D. T. Wickramasinghe and L. Ferrario, Publ. Astron. Soc. Pac. **112**, 873 (2000).

34. B. Zuckerman and I. N. Reid, Astrophys. J. Lett. **505**, L143 (1998).

Translated by V. Astakhov

Spectroscopy of the W Virginis Star V1 (K 307) in the Globular Cluster M12

V. G. Klochkova[1*], V. E. Panchuk[1], N. S. Tavolganskaya[1], and V. V. Kovtyukh[2]

[1]Special Astrophysical Observatory, Russian Academy of Sciences, Nizhniĭ Arkhyz, 369167
Karachai-Cherkessian Republic, Russia
[2]Astronomical Observatory, Odessa University, Odessa, Ukraine
Received February 14, 2003

Abstract—High-resolution CCD spectra have been obtained for the first time for the W Virginis star V1 (K 307) in the globular cluster M12 and its closest neighbor K 307b ($m_{pg} = 14^m$; the angular distance from the W Vir star is $\delta < 1$ arcsec). We determined the fundamental parameters ($T_{eff} = 5600$ K, $\log g = 1.3$, and $T_{eff} = 4200$ K, $\log g = 1.0$ for the W Vir star and the neighboring star, respectively) and their detailed chemical composition. The derived metallicities of the two stars ([Fe/H] $= -1.27$ and -1.22 relative to the solar value) are in good agreement with the metallicities of other cluster members. Changed CNO abundances were found in the atmosphere of the W Vir star: a small carbon overabundance, [C/Fe] $= +0.30$ dex, and a large nitrogen overabundance, [N/Fe] $= +1.15$ dex, with oxygen being underabundant, [O/Fe] ≈ -0.2 dex. The C/O ratio is ≥ 1. Na and the α-process elements Mg, Al, Si, Ca, and Ti are variously enhanced with respect to iron. We found an enhanced abundance of s-process metals relative to iron: [X/Fe] $= +0.34$ for Y, Zr, and Ba. The overabundance of the heavier metals La, Ce, and Nd with respect to iron is larger: [X/Fe] $= +0.49$. The largest overabundance was found for the r-process element europium, [Eu/Fe] $= +0.82$. The spectrum of the W Vir star exhibits the Hα and Hβ absorption−emission profiles and the He I $\lambda 5876$ Å emission line, which are traditionally interpreted as a result of shock passage in the atmosphere. However, the radial velocities determined from absorption and emission features are in conflict with the formation pattern of a strong shock. The high luminosity $\log L/L_\odot = 2.98$, the chemical peculiarities, and the spectral peculiarity are consistent with the post-AGB evolution in the instability strip. The pattern of relative elemental abundances [X/Fe] in the atmosphere of the neighboring star K 307b is solar. Statistically significant differences were found only for sodium and α-process elements: the mean overabundance of light metals is [X/Fe] $= +0.35$. © *2003 MAIK "Nauka/Interperiodica"*.

Key words: *globular clusters, post-AGB stars, spectroscopy, chemical composition, shock waves.*

INTRODUCTION

High-spectral-resolution observations of stars in globular clusters are the key to several problems: the spectroscopic calibration of metallicity indices, the dispersion of elemental abundances in the atmospheres of red giants, the simultaneous formation of cluster stars, the evolution with additional shell mixing, and the evolution upon interaction with neighboring stars and the interstellar medium. The still scarce spectroscopic observations of physical variable stars in globular clusters play an important role.

In this paper, based on high-resolution spectra, we determine the fundamental parameters and detailed chemical composition of the variable star V1 discovered by Sawyer-Hogg (1938a) in the globular cluster M12. In addition, we analyze the radial velocities

measured from various features in the star's spectrum. M12 is generally believed to contain only one variable (Clement *et al.* 2001). However, Malakhova *et al.* (1997) discovered two more cluster stars in the instability strip that were suspected to be RR Lyr variables. In the list by Küstner (1933), the W Vir star in M12 is designated as K 307; below, we use this designation in the text. The apparent magnitude of the variable varies over the range $V = 12^m0-13^m5$. The star belongs to the group of W Vir stars that have a photometric variability period $P \approx 15^d5$. The catalog by Harris (1996) gives the following basic parameters for the globular cluster M12: the mean heliocentric velocity $V_r = -42.2$ km s^{-1} (with respect to the Local Standard of Rest, $V_{lsr} = -26.4$ km s^{-1}), the mean color excess $E = 0.19$, the distance modulus $m - M = 14^m02$, and the heliocentric distance $d = 4.9$ kpc. A modern $V - (B - V)$ diagram for

*E-mail: `valenta@sao.ru`

M12 is given in Brocato *et al.* (1996). It follows from this diagram that K 307 is brighter than asymptotic-giant-branch (AGB) stars with the same $(B - V)$ color index by approximately two magnitudes, which allows it to be considered as a post-AGB star.

This paper is a continuation of our series of publications devoted to the investigation of stars at the short-duration transition evolutionary phase from the AGB to a planetary nebula (see Klochkova *et al.* (2001) and references therein). The main goal of our program is to study the chemical peculiarities of objects that have passed through the sequential change of energy release sources, mixing, and dredging-up of matter from layers with a changed chemical composition to the surface. Since the W Vir stars are evolved variable post-AGB stars (Gingold 1985), it would be natural to study them within the framework of our program. Variable stars in globular clusters are of special interest, because, being cluster members, their evolutionary phase and luminosity can be determined more reliably than those for Galactic field variables. However, the fact that the star under study belongs to a system of globular clusters complicates its high-spectral-resolution observations, because these objects are far from the Sun. In addition, cluster membership is difficult to prove, especially for stars lying above the horizontal branch. In essence, only one of the universally accepted selection criteria is decisive for such objects: the radial velocity. For stars in M12, the velocities V_r range from -58 to -29 km s^{-1} (Joy 1949). For a reciprocal spectrogram linear dispersion of 100 Å mm^{-1}, this range more likely reflects measurement errors rather than a peculiar velocity dispersion of the cluster members.

Zinn *et al.* (1972) found nine stars in M12 that are located above the horizontal branch in the color–magnitude diagram, suggesting the name "UV-bright stars" for them. Having measured the radial velocities for a sample of stars, Harris *et al.* (1983) confirmed the cluster membership of several UV-bright stars in the cluster M12 (in particular, the membership of K 307). The high probability of the cluster membership of K 307 was also confirmed by proper-motion measurements for M12 field stars (Geffert *et al.* 1991). Based on moderate-resolution spectra for stars in the globular cluster M12, these authors gave a mean velocity $V_r = -41.3$ km s^{-1}. For K 307, they gave two velocities, -36.4 and -40.9 km s^{-1}, with an rms deviation $\sigma \geq 3.3$ km s^{-1}.

The W Vir star K 307 has a close neighbor (below, this star is called K 307b for short) at an angular distance $\delta < 1$ arcsec. Sawyer-Hogg (1938b) estimated the photographic magnitude of K 307b to be $m_{pg} = 14^m$. Because of the excellent seeing during our spectroscopic observations with the 6-m telescope, apart from the spectrum of the W Vir star, we were also able to obtain a high-quality spectrum for its neighbor.

In this paper, we briefly describe our methods of observations, data reduction, and analysis. We present the radial velocities V_r measured from emission and absorption features in the spectrum and the results of our determination of the detailed atmospheric chemical composition for the two stars. We discuss the results obtained and give our main conclusions.

OBSERVATIONS AND DATA ANALYSIS

We obtained echelle spectra in the wavelength range 4550–7940 Å at the prime focus of the 6-m BTA telescope equipped with the PFES spectrometer. The spectrometer and its capabilities were described by Panchuk *et al.* (1998). The PFES echelle spectrometer is equipped with a 1160×1040-pixel CCD array (16×16 μm pixel size) designed at the Special Astrophysical Observatory. The PFES spectrometer provides a spectral resolution up to $R = 17\,000$ over a wide wavelengths range. The spectrum of a Th–Ar lamp was taken for wavelength identification. The reduction of two-dimensional images (the standard procedures of dark-current subtraction, cosmic-ray-particle hit removal, stray-light subtraction, and echelle-order extraction), as well as the spectrophotometric and position measurements in one-dimensional spectra, were described previously (see, e.g., Klochkova *et al.* 2002). Since the signal-to-noise ratio in the spectral regions used for the abundance analysis exceeds 100–150, we can measure the equivalent widths of weak lines as small as 5–7 mÅ. The mean epoch of observations for K 307 is JD = 2452072.312. However, we cannot calculate the phase of the photometric curve, because, as Clement *et al.* (1988) showed using long-term photometric observations, the period for K 307 is unstable.

Fundamental Stellar Parameters

To determine the fundamental parameters of model stellar atmospheres (effective temperature T_{eff} and surface gravity $\log g$), and to compute the chemical composition and synthetic spectra, we used the grid of model stellar atmospheres computed by Kurucz (1993) in the hydrostatic approximation.

We determined the fundamental model-atmosphere parameters for the two stars by using only spectroscopic criteria. For the W Vir star, the spectroscopic method for determining the parameters

is preferred, because we have no grounds for extrapolating the photometric data to the epoch of our observations due to the variability of its photometric period (Clement *et al.* 1988). No accurate photometric data are available for K 307b. Since the PFES echelle spectrometer simultaneously records a wide spectral range, we can determine the fundamental model parameters T_{eff} and $\log g$ by using only spectroscopic criteria that are unaffected by interstellar and circumstellar reddening. We estimated the effective temperature by the standard method (from the condition of the neutral iron abundance being independent of the excitation potential of the corresponding lines), and chose the surface gravity from the ionization balance condition for iron atoms and the microturbulence ξ_{t} from the condition of the iron abundance being independent of the line intensity. In determining the model-atmosphere parameters, it is important to use low- and moderate-intensity lines with equivalent widths $W \leq 0.25$ Å. The approximation of a steady-state plane-parallel atmosphere can be inaccurate when describing the strongest spectral features. In addition, strong absorption features can be distorted by the line splitting observed at certain pulsation phases. At an insufficient spectral resolution or a small radial-velocity difference between layers, this distortion manifests itself in an additional broadening of the line profiles.

The equivalent widths and oscillator strengths gf of the spectral lines involved in determining the model parameters and the computed elemental abundances are given in a table that is accessible via E-mail (valenta@sao.ru). To receive these data, it is necessary to send an electronic request with the words "K307, data" in the Subject line.

Thus, the effective temperatures were determined from the condition of the iron abundance being independent of the lower-level excitation potential for the lines used. An additional criterion for the reliability of the method is the absence of the same dependence constructed for other chemical elements that are also represented in the spectra by numerous lines (Ca I, Ti I, Ti II, Cr I, Cr II, Ni I). In addition, in a reliable microturbulence determination, there is no dependence of individual abundances on the equivalent widths of the lines used for the computations. The abundances of silicon, titanium, and chromium derived from both lines of neutral atoms and ion lines are in agreement, within the accuracy of the method. This agreement suggests that the surface gravity was correctly estimated from the ionization balance condition for iron atoms. The derived model-atmosphere parameters T_{eff}, $\log g$, and ξ_{t} and the elemental abundances $\epsilon(X)$ for the two stars under study are given in Table 1. This table also gives the elemental abundances relative to iron [X/Fe].

The typical accuracies of determining the model parameters (on average) for a star with a temperature of $\sim$5000 K are $\Delta T_{\text{eff}} \approx 150$, $\Delta \log g \approx 0.3$ dex, and $\Delta \xi_{\text{t}} \approx 0.5$ km s^{-1}. It should be borne in mind that most of the lines used to compute the chemical composition have equivalent widths of less than 100 mÅ. Therefore, the accuracy of the observational data must be very high, because at a given spectral resolution, the accuracy of W for weak lines depends mainly on the signal-to-noise ratio in the spectrum. The scatter of the elemental abundances derived from a set of lines is small; the rms deviation σ mainly does not exceed 0.25 dex (see Table 1). We performed all our computations with the WIDTH9 code developed by Kurucz. Figure 1 gives an example of a computed synthetic spectrum for K 307 with the model parameters and atmospheric chemical composition from Table 1.

In general, however, the internal consistency of the parameters suggests that the homogeneous model atmospheres used are suitable for LTE computations of weak lines. The detailed discussions by Luck and Bond (1989) and Gonzalez and Wallerstein (1994) confirm that the plane-parallel models and the local-thermodynamic-equilibrium (LTE) approximation can be used to analyze the spectra of pulsating stars in globular clusters. The main restriction is that, in analyzing the atmospheric chemical composition, one should avoid using the states of the atmosphere when the splitting of metal absorption lines due to shock passage is observed. The spectra of stars with luminosities close to the luminosity of ROA 24 in the globular cluster ω Cen ($M_v = -3^m66$) can also be affected by an extended atmosphere. The derived model-atmosphere parameters T_{eff} and $\log g$ as well as the known mean color excess $E = 0.19$ and distance modulus of the cluster $m - M = 14^m02$ allow us to estimate the absolute magnitude of the W Vir star $M_v = -2^m6$ and its luminosity $\log L/L_\odot = 2.98$, which is much lower than the luminosity of ROA 24. If we plot K 307 on the $\log T_{\text{eff}} - \log L/L_\odot$ diagram for variables in globular clusters (Gingold 1985), then we will see that the effective temperature and the luminosity closely correspond to the expected position in the instability strip for a W Vir star with a period of about 15$^{\text{d}}$. According to the formula (Gingold 1985), the luminosity $\log L/L_\odot = 2.98$ corresponds to the core mass $M/M_\odot = 0.52$.

DISCUSSION OF THE RESULTS

Radial Velocities

The radial velocities measured from lines in the spectra of K 307 and K 307b are given in Table 2. To increase the accuracy of determining the velocity, we

Table 1. The chemical composition $\log \epsilon(X)$ of the W Vir star K 307 and its companion K 307b (for $\log \epsilon(H) = 12.0$)

Sun		K 307					K 307b			
		5600 K, 1.3, 4.0 km s⁻¹					4200 K, 1.0, 2.2 km s⁻¹			
E	$\log \epsilon(E)$	X	$\epsilon(X)$	n	σ	[X/Fe]	$\epsilon(X)$	n	σ	[X/Fe]
C	8.55	CI	7.50	6	0.27	+0.22				
N	7.97	NI	8.10	2		+1.40				
O	8.87	OI	7.90	3	0.10	+0.30				
		OI	7.4[1]	3	0.10	−0.20				
Na	6.33	NaI	5.49	3	0.15	+0.43	5.51	1		+0.40
Mg	7.58	MgI	6.36	2		+0.05	6.70	1		+0.34
Al	6.47	AlI	6.05[2]	1		+0.85	5.66	1		+0.41
Si	7.55	SiI	6.63	8	0.25	+0.35	6.57	3	0.21	+0.24
		SiII	6.56	2		+0.28				
S	7.21	SI	6.50	4	0.13	+0.56	7.18[2]	1		+1.19
Ca	6.36	CaI	5.29	19	0.24	+0.20	5.43	3	0.22	+0.29
Sc	3.17	ScI					1.94	1		−0.01
		ScII	1.85	7	0.25	−0.05	2.03	3	0.40	+0.08
Ti	5.02	TiI	3.95	10	0.15	+0.20	4.20	8	0.06	+0.40
		TiII	3.86	10	0.18	+0.11	3.95	2		+0.15
V	4.00	VI					3.01	15	0.17	+0.23
Cr	5.67	CrI	4.23	6	0.23	−0.17	4.35	5	0.12	−0.10
		CrII	4.39	6	0.20	−0.01	4.30	2		−0.15
Mn	5.39	MnI	4.04	2		−0.08	4.00	4	0.20	−0.17
Fe	7.50	FeI	6.21	115	0.19	−0.02	6.28	76	0.22	0.00
		FeII	6.25	18	0.17	+0.02	6.28	3	0.16	0.00
Co		CoI					3.72	4	0.05	+0.02
Ni	6.25	NiI	4.89	9	0.19	−0.09	5.06	12	0.15	+0.03
Cu	4.21	CuI	2.94	2		0.00	2.94	1		−0.05
Zn	4.60	ZnI	3.43	2		+0.10				
Y	2.24	YII	1.14	4	0.22	+0.17	1.25	2		+0.23
Zr	2.60	ZrII	1.84	3	0.33	+0.51				
Ba	2.13	BaII	1.20	2		+0.34	1.06	1		+0.15
La	1.22	LaII	0.63	4	0.11	+0.68	−0.06	1		−0.06
Ce	1.55	CeII	0.73	4	0.12	+0.45	−0.01	1		−0.34
Pr	0.71	PrII					−0.29	1		+0.22
Nd	1.50	NdII	0.57	3	0.19	+0.34	0.26	2		−0.02
Eu	0.51	EuII	0.06	3	0.08	+0.82	−0.44	1		+0.27

Note: In the table, n is the number of lines used, and σ is the dispersion of the abundance determined for a given number of lines. The model parameters T_{eff} K, $\log g$, and ξ_t are given under the star number. The elemental abundances $\log \epsilon(E)$ in the solar photosphere were taken from Grevesse *et al.* (1996).

[1] The oxygen abundance corrected for non-LTE effects.

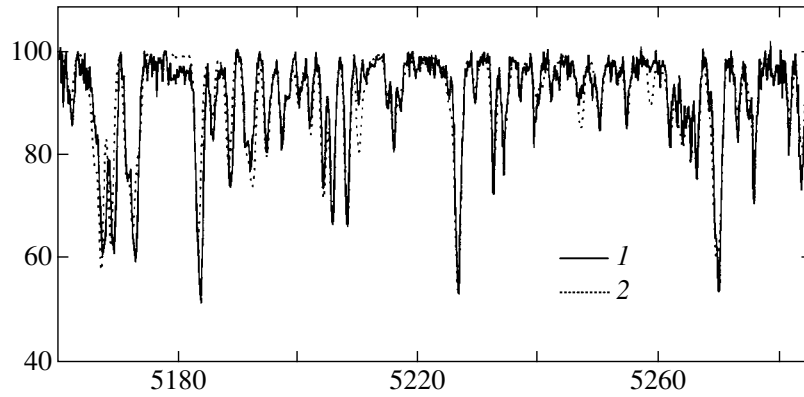[2] The abundance of this element was determined with a low accuracy.

Fig. 1. Comparison of portions of the observed spectrum for K 307 (*1*) and its theoretical spectrum (*2*).

selected unblended lines by comparing the observed and synthetic spectra. The zero position point for each spectrogram was determined by the standard method,

Table 2. The heliocentric radial velocities V_r of the W Vir star K 307 and its companion K 307b, measured from various spectral features

Spectral features	V_r, km s^{-1}	
	K 307	K 307b
Metals	−40.6 (462)	−39.2 (705)
He I λ5876	−41.4 (1)	
Hα, (blue-em)	−73.4 (1)	−94.6 (1)
abs	−37.3 (1)	−32.6 (1)
(red-em)	−3.6(1)	
Hβ, (blue-em)	−101.8 (1)	−35.6 (1)
abs	−44.4 (1)	
(red-em)	+32.7 (1)	
NaD-phot	−40.0 (2)	−34.8 (2)
NaD-IS	−15.2 (2)	
DIB	−18.2 (2)	−34.1 (1)

Note: V_r(blue-em) is the velocity measured from the blueshifted emission line peak; V_r(red-em) is the velocity measured from the redshifted emission line peak; V_r(NaD-phot) is the velocity measured from the photospheric NaD doublet lines; and V_r(NaD-IS) is the velocity measured from the circumstellar D line components. The number of lines measured to determine the velocity is given in parentheses.

by referencing to the positions of ionospheric night-sky emission features and telluric absorption features observed against the background of the object's spectrum. The typical error of the mean is $\delta = 0.2$ km s^{-1}, with the accuracy of measurement from a single line being $\sigma \approx 3.4$ km s^{-1}. The mean radial velocity of the W Vir star estimated from metal absorption lines, V_r(met) $= -40.6$ km s^{-1}, is in good agreement with the data obtained by Harris *et al.* (1983) twenty years ago. For W Vir stars, the amplitude of the radial velocity measured from metal lines is about 40 km s^{-1}. Therefore, the close agreement between our measurements and the data by Harris *et al.* (1983) most likely implies that the phases of the observations coincide. Since there is no information about the radial-velocity amplitude for K 307, it may well be that this amplitude is anomalously small.

A peculiarity of the spectrum for K 307 is the presence of several absorption features that we identified with diffuse interstellar bands (DIBs). The equivalent width of the most easily distinguishable λ6613 Å band is 97 mÅ. Since the well-known λ5780 band is blended with photospheric spectral lines, its parameters are difficult to measure. The resonance NaD1, D2 doublet lines in the spectrum of K 307 are asymmetric: their cores are redshifted. Our measurements indicate that both lines are blends that are poorly resolvable at the spectral resolution used. The blends contain two components: the velocity of one component is equal to the star's radial velocity, while the position of the other component, within the error limits, corresponds to the velocity measured from DIBs (see Table 2). The detected absorption bands can originate in the circumstellar environment, because the shock passage results in a mass outflow and the formation of a circumstellar gas–dust shell (Fadeyev 2001).

As follows from the study by Klochkova and Samus' (2001), each of the NaD1, 2 doublet lines in the spectrum of K 413 contains two components, and

the position of one of the components is close to the radial velocity of the photospheric spectrum. The radial velocity determined from the second component, $V_r = -24.6$ km s^{-1}, is equal to the velocity measured from DIBs and differs from the velocity of the same component in the spectrum of K 307. Consequently, the second component does not originate in the volume common to both cluster stars. The radial-velocity difference confirms the assumption about the circumstellar origin of the DIBs and the red NaD components in the spectra of the two stars.

However, the interstellar origin of these features cannot be ruled out either. For example, the spectrum of the hot (and closer to the Sun) star μ Ophiuchi, whose Galactic coordinates are close to those of M12, exhibits interstellar features whose positions correspond to a radial velocity of -19 km s^{-1} (Hobbs 1969). The latter is equal to the velocity measured from the red NaD components and DIBs for K 307. Further observations with a higher spectral resolution for K 307 and other luminous cluster stars are required to reach a final conclusion.

The spectrum of the star K 307b has similar peculiarities: first, Hα is slightly asymmetric due to the weak emission feature in the blue line wing; and, second, the equivalent width of the λ6613 Å absorption feature is reliably measured, $W = 125$ mÅ. Since the equivalent width of the λ6613 Å band in the spectrum of K 413 is $W = 66$ mÅ, we can make the assumption about the intensity dispersion of this band inside the globular cluster. This dispersion argues for the circumstellar origin of the DIBs in the spectra of the M12 stars that we studied.

The radial velocities determined from metal lines in K 307 and K 307b are almost equal. This equality suggests that, to within the radial-velocity differences between these stars, at the given photometric phase of K 307, we do not observe any significant inward and outward motions of the layers that form the photospheric metal lines. It follows from the radial-velocity curve for W Vir (Lèbre and Gillet 1992) that the phase interval 0.3−0.5 corresponds to this state. In this phase interval, W Vir exhibits an almost symmetric two-component emission−absorption Hα line profile, which we observe in the spectrum of K 307.

Hydrogen Lines

The main peculiarities of the spectrum for K 307 are the complex Hβ and Hα absorption−emission profiles as well as the emission feature in the He I λ5876 Å line (see Figs. 2 and 3 and Table 2). Let us consider the interpretation of the emission features in more detail.

The emission feature in Hα in the spectra of W Vir stars is commonly explained by the radiation of a hot region behind the shock front in the atmosphere of a pulsating star (Abt 1954). The spherically symmetric radiation zone can be located both in the immediate vicinity of the photosphere, when the stellar disk almost completely shields the receding part of this zone (case 1), and at a considerable distance from the star (Willson 1976), when both the approaching and receding parts of this zone can be observed (case 2). In the second case, there is no need to interpret the dip between the emission components as a result of absorption in the shell located above the radiation zone. The systematic excess in the intensity of the blue emission component above the red component may also be considered to be evidence for case 2 (because the star shields part of the spherically symmetric radiation zone receding from the observer). Gillet (1988) believes that, if there are no hydrogen absorption features falling into the Hα core in the shell located above the shock front, then the location of the central minimum above the continuum level is evidence for case 2. Gillet *et al.* (1983) showed that case 2 is characteristic of the extended atmospheres of Mira stars. Here, we make two remarks: (i) the location of the central minimum above the continuum level can occasionally result from an insufficient spectral resolution; (ii) the profile where the central minimum is located below the continuum level can also be obtained in case 2 if the emission components are superimposed on regions near the photospheric Hα core rather than on the continuum.

Figure 2a shows the observed Hα profile in the spectrum of K 307, the synthetic spectrum computed with the atmospheric parameters determined from the metal absorption spectrum, and the difference between the observed and theoretical spectra. The shift of the theoretical spectrum from the observed spectrum was chosen in such a way that the positions of the metal lines coincided (in this case, the position of the absorption core of the photospheric Hα profile corresponds to the radial velocity determined from metal lines). After the subtraction of the photospheric spectrum, the blue emission component proved to be again weaker than the red component; i.e., the pure emission profile does not correspond to case 2 (Willson 1976). A strong objection to case 2 is the absence of a similar pattern in the Hβ profile. Indeed, the red emission component in Hβ is broader and stronger than the blue component (Fig. 2b), while in Willson's case, the same narrow components and at the same positions on the V_r scale as those for Hα must be observed. This effect can be explained in case 1 by assuming that there is a sufficient amount of matter above the radiation region to produce the absorption component not only in Hα but also in Hβ.
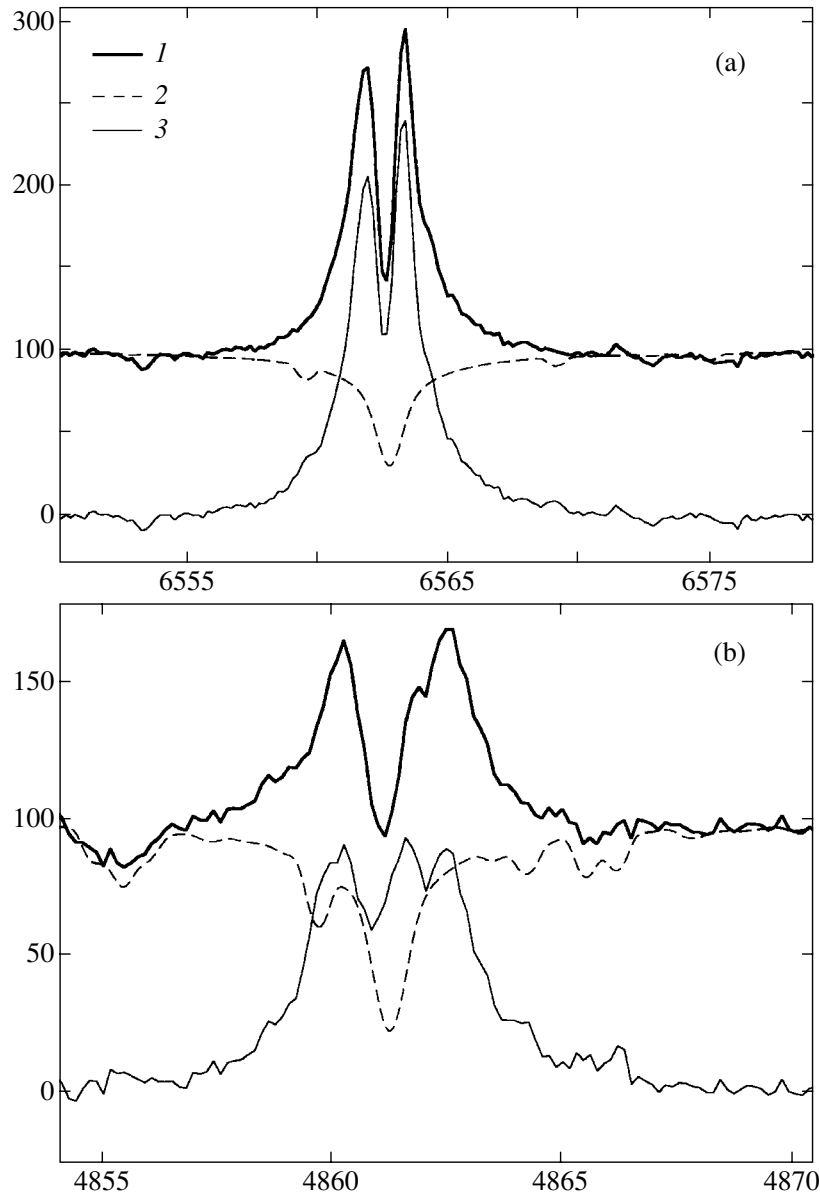
Fig. 2. Portions of the spectrum for K 307 with the (a) Hα and (b) Hβ profiles: *1*—observed spectrum, *2*—theoretical photospheric spectrum, *3*—result of the subtraction. The telluric features were not removed from the observed spectrum.

We believe that the radial velocity of the Hβ absorption component (-44.4 km s^{-1}) is affected by the red emission component. Therefore, below, we disregard the radial-velocity difference between the Hβ absorption core and the narrow minimum in the Hα profile (-37.3 km s^{-1}).

Thus, we infer from the absence of a close similarity between the Hα and Hβ profiles that the central minima in the profiles of these lines are the hydrogen absorption components. We get an additional argument by subtracting the synthetic absorption spectrum from the observed Hβ profile (Fig. 2b). The blue

Hβ wing contains Fe I lines whose subtraction makes the wings of the emission profile more symmetric.

We came to a scheme where the radiation region is located near the photosphere; i.e., we observe only the half of the spherically symmetric shock front that faces us (case 1). In this case, the central minimum is interpreted as absorption by hydrogen atoms in the shell located above the radiation region. Let us first consider the Hα profile. Since the intensities of the observed emission peaks are similar, the radial velocity determined from the position of the central absorption component was overestimated (toward negative values) only slightly, and, to a first
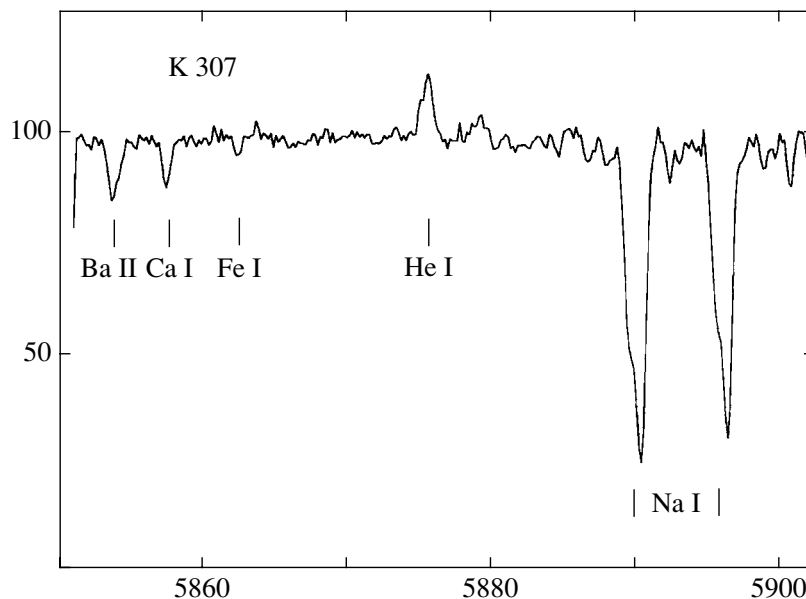
Fig. 3. A portion of the spectrum for K 307 containing the He I and Na D1, D2 doublet lines. The vertical bars indicate the strongest lines. The telluric features were not removed from the observed spectrum.

approximation, we may take $V_r = -37.3$ km s^{-1}. If we identify the absorption component with the matter than is farthest from the star, i.e., virtually at rest relative to its center, then the velocity of K 307 estimated in this way is close, within the limits of the radial-velocity dispersion for M12 stars (Joy 1949), to the mean radial velocity of the globular cluster (-42.2 km s^{-1}) and the radial velocity of the neighboring star (V_r^b(met) $= -39.2$ km s^{-1}). We adopted the hypothesis that the position of the central absorption component does not change with phase by analogy with the results of spectroscopic observations for W Vir (Lèbre and Gillet 1992). The velocity of the radiation region can be estimated either from the outer wings of the double emission profile or by restoring the emission core. In any case, we find that the radiation region is virtually at rest. The term "direction of motion" is conditional here, because velocities above 100 km s^{-1} correspond to the width of the emission peak. Thus, we have another difficulty in case 1: if the two-peak emission profile is considered as the remnants of a one-component profile, then the profile width is nonthermal; i.e., macroscopic motions with radial velocities that differ by several tens of km s^{-1} are observed in the radiation region. We drew the same conclusion from our analysis of the Hβ profile (see Fig. 2b).

The first attempts to numerically simulate the postshock hot region showed (Panchuk 1971) that when the shock wave is produced by the "turnover" of a rising compression wave, i.e., when the circumphotospheric matter rises faster than the unperturbed

matter located above the shock front, the blue emission component is always more intense than the red component. The asymmetry of the emission peak attributable to the velocity gradient in the postshock radiation region is small, for example, only 0.05 Å for an RR Lyr star. The development of dynamic models allowed the influence of the hydrogen ionization zone to be taken into account (Adams and Castor 1979). It was shown that the velocity discontinuity could also be formed during the shell expansion and cooling at the inward-moving hydrogen recombination front; i.e., the radiation region could form emission lines redshifted from the absorption spectrum.

Computations of hydrodynamic models with radiative transfer in the moving atmosphere of a W Vir star show that the blue Hα emission component is always more intense than the red component (Fokin 1991) and that the full width at half maximum (FWHM) of the Hα emission peak does not exceed 1.5 Å (Fadeyev 2001). Our observations of K 307 show a much larger FWHM of the emission peak (more than 2.5 Å) and an enhanced intensity of the red emission component. Consequently, the width of the Doppler core of the Hα emission profile and the intensity ratio of the blue and red emission components in the spectrum of K 307 require additional explanations.

In general, the blue emission component in the spectra of radially pulsating stars of different types is stronger (Gillet 1988). However, shortly before the brightness minimum of W Vir, the intensity of the red emission components exceeds that of the blue

component for a short time (at phase 0.537) (Lèbre and Gillet 1992). It may well be that we observed K 307 at a close phase. According to Lèbre and Gillet (1992), the narrow absorption feature in the Hα profile near the position that corresponds to the photospheric spectrum originates in a region outside the photosphere of W Vir. The Hβ emission profile exhibits two absorption components (Fig. 2b); the second absorption component also shows up in the red wing of the Hα emission profile (see Fig. 2a). Note that the difference between the radial velocities (68 km s^{-1}) determined from the absorption components in the Hβ profile, within the error limits, is equal to the difference (70 km s^{-1}) determined from the emission components in the Hα profile.

The presence of emission wings in Hα is also a problem. A spectroscopic monitoring of W Vir indicates that the emission wings in Hα appear at phase 0.611, reach their maximum at phase 0.730, and disappear at phase 0.945 (Lèbre and Gillet 1992). It was concluded that the Stark Hα emission wings are formed at certain densities and shock velocity in the atmosphere of W Vir. We emphasize that the effect of periodic appearances of broad emission wings in the spectrum can also arise for a constant contribution of the emission component, when only the contribution of the Stark absorption wings (they are weaker when the effective temperature is at a minimum, near phase 0.6) changes due to a change in photospheric effective temperature. If we attribute the appearance of emission wings only to an increase in density and temperature in the postshock region, then we conclude that the density and temperature of the radiation region must be at a maximum at phases 0.5–0.6. We used the models by Kurucz (1993) to roughly estimate these parameters by comparing the FWHMs of the theoretical Hα profiles at a given residual intensity with the observed FWHMs of the emission wings, measured at the same relative intensity and counted off upward from the continuum level. We found that the observed FWHMs of the emission wings correspond to the photospheric density and temperature in the model with $T_{\mathrm{eff}} = 5500$ K; this estimate does not depend on log g, because the luminosity effect in the Hα wings is negligible at temperatures below 7000 K. Using the outdated theory of Stark broadening by de Jager (1952), Raga *et al.* (1989) concluded that the emission wings of the Hβ and Hδ lines in the spectrum of W Vir correspond to an electron density of 2×10^{14} cm^{-3}. This value gives a density estimate for all preshock particles that is lower than the density estimated from a hydrostatic model by two orders of magnitude.

Let us discuss the possibility of emission-line broadening by free-electron scattering. The broadening of emission lines by Thomson electron scattering

in the spectra of hot stars has long been known (Münch 1950; Marlborough 1969; Castor *et al.* 1970; Bernat and Lambert 1978; Wolf *et al.* 1981). If the atmosphere above the Hα emission formation region has an appreciable optical depth for Thomson scattering by free electrons, then some of the Hα photons are scattered with a frequency redistribution. Since the electrons have higher thermal velocities, the scattered photons can produce extended emission features. For example, at the solar photospheric temperature, the mean thermal electron velocity is a factor of 43 higher than the proton velocity; i.e., at a thermal proton velocity of 9.7 km s^{-1}, the electron velocity is 415 km s^{-1}. For the Hα line, this velocity corresponds to a shift by 9 Å. Thus, if several percent of the photons emitted in the Hα core are scattered by free electrons, then weak emission wings with a length of several Å can arise. Estimates of the optical depth for Thomson scattering for a hydrostatic model with the above parameters give an optical density $\tau_{\mathrm{s}} = 0.1$, i.e., the free-electron scattering in an unperturbed atmosphere may be disregarded. In addition, a significant number of electrons is contained in the zone above the recombination region. The maximum postshock electron density for W Vir is estimated to be 2×10^{16} (Raga *et al.* 1989); i.e., a layer 7.5×10^7 cm in thickness, which significantly exceeds the extent of the radiation zone, provides an optical depth for Thomson scattering $\tau_{\mathrm{s}} = 1$. We conclude that the free-electron scattering mechanism in the atmospheres of W Vir stars cannot adequately explain the Hα emission wings.

If the spectroscopic variations of K 307 and W Vir with phase are assumed to have the same pattern, then the presence of Stark wings in the Hα emission profile in the spectrum of K 307 points to phases 0.7–0.9 (Lèbre and Gillet 1992). The emission feature in the He I λ5876 Å line is characteristic of phases 0.8–0.0 (Lèbre and Gillet 1992). The phase at which a similar Hα profile is observed in the spectrum of W Vir is distinctly different (0.54). The shape of the Hα profile depends not only on the parameters of the radiation region but also on the parameters of the matter outside the stellar atmosphere, while the Hα emission wings and the emission feature in the He I λ5876 Å line originate solely in the radiation region. Therefore, based on the emission features, we may assume that the spectrum of K 307 was obtained at the ascending branch of the light curve, near phase 0.8. The shape of the absorption spectrum is inconsistent with this assumption. Indeed, a double absorption-line structure with a radial-velocity difference of ∼50 km s^{-1} is observed at phases 0.8–0.0 for W Vir, while for K 307, only one absorption system

is seen. We conclude that there is no close similarity between the spectra of W Vir and K 307. Thus, because of the absence of absorption-line splitting, we cannot determine the shock velocity and then, following Wallerstein (1959) or Raga *et al.* (1989), estimate the helium abundance. An important fact in estimating the helium abundance is that other stars were also investigated in the globular cluster under consideration. The metallicity of the W Vir star (normalized to the hydrogen abundance) is equal to the metallicities of the other two stars in M12 that we investigated by the same method. This equality can be interpreted as evidence of the normal hydrogen abundance in the atmosphere of K 307 (the effects where a significant part of hydrogen is replaced with helium were discussed by Klochkova *et al.* 2002).

Let us attempt to estimate the intensity ratio of the Hα and Hβ components. By Gaussian fitting of the emission-core remnants, we can restore the central intensities of the distorted emission profiles. Since no spectrophotometric data are available for K 307, we used the fluxes in the photospheric spectrum for Kurucz's closest model with parameters (5500, 2.0, −1.0). The ratio of the Hα and Hβ emission fluxes is 1.8, a value that is lower than the ratio for the pure recombination mechanism (3). The intensity of the Hα emission component, even if corrected for effect of the narrow absorption component, appears to be underestimated. This is also suggested by evidence for the presence of a second absorption component, which shows up in the asymmetry of the red wing of the Hα emission component. Two narrow absorption components are clearly distinguished in the Hβ emission profile corrected for the effect of the photospheric absorption profile.

Helium Lines

Since there is no matter capable of absorbing in the corresponding transition above the radiation layer in the He I 5875.64 Å line, the profile intensity is measured reliably. The radial velocity determined from the He I λ5876 Å line is almost equal to the velocity estimated from metal absorption lines. This result confirms the conclusion drawn above from the hydrogen spectrum: the radiation region is virtually at rest relative to the region that forms the absorption spectrum.

The intensities of the Balmer hydrogen lines and the He I λ5876 Å line can be explained mostly by the recombination mechanism. Consequently, these intensities must be sensitive to both preshock ionization and postshock collisional ionization. Shull and McKee (1979) showed that shock waves with velocities below 80 km s^{-1} do not produce significant preshock ionization. Based on our line position

measurements, we have no reason to suggest the presence of such high velocities in the atmosphere of K 307. Therefore, the preshock matter may be assumed to be nonionized.

Wallerstein (1959) was the first to estimate the helium abundance in the atmosphere of W Vir by using the LTE approximation. Let us repeat this estimation for K 307 by correcting the Hβ emission profile for the photospheric absorption component. Given the ratio of the continuum fluxes near He I λ5876 Å and Hβ for Kurucz's model with parameters (5500, 2.0, −1.0), the intensity ratio of these emission lines in the spectrum of K 307 is 0.10. The Hα and He I λ5876 Å intensity ratio is 18. Following Wallerstein (1959), we obtain the ratio $N(H)/N(He) = 13.8$ by the number of particles. Thus, there is no reason to believe that the atmospheric helium abundance for K 307 exceeds its solar value.

The Chemical Composition

The metallicity of the globular cluster M12 was previously estimated from photometric data and low-resolution spectra. Da Costa and Armandroff (1995) obtained [Fe/H] = −1.34 from their observations of the Ca II (8498, 8542, 8662 Å) triplet and assigned M12 to the intermediate subsystem of globular clusters. However, based on the intensity of the Ca II triplet, Rutledge *et al.* (1997) derived a higher metallicity, [Fe/H] = −1.14, from low-resolution spectra. Based on high-resolution spectroscopic observations of several stars in selected globular clusters, Carretta and Gratton (1997) suggested a new homogeneous metallicity scale for an extensive sample of globular clusters. In particular, they obtained [Fe/H] = −1.37 for M12. Klochkova and Samus' (2001) published the detailed chemical composition of K 413—one of the UV-bright stars in the globular cluster M12. Based on high-resolution spectra, these authors found the star's metallicity to be [Fe/H] = −1.38 and concluded that, judging by its set of parameters, K 413 is most likely in the post-AGB evolutionary phase. Table 1 gives the chemical composition of K 413 for comparison with the chemical composition of the W Vir star. It follows from the cluster diagram that the W Vir star is located in the region of stars that are much more luminous than K 413. The absolute magnitude $M_v = −1.73^m$ for K 413 is fainter than that for the W Virginis by almost one magnitude.

For the two stars studie here, K 307 and K 307b, Table 1 gives the elemental abundances $\log \epsilon(X)$ averaged over the set of measured lines and their dispersions σ. The second column in Table 1 gives the corresponding data from Grevesse *et al.* (1996) for

the solar atmosphere that we used to determine the relative abundances

$$[X/Fe] = [\log \epsilon(X) - \log \epsilon(Fe)]_\star$$
$$- [\log \epsilon(X) - \log \epsilon(Fe)]_\odot,$$

which are required to analyze the abundance curve of the chemical elements. Below, we consider the abundance pattern of the chemical elements in the atmosphere of the star under study in more detail (see Table 1).

Metallicity. $[Fe/H] = -1.27$ for K 307 and $[Fe/H] = -1.22$ for K 307b are in good agreement with the results obtained by Klochkova and Samus' (2001) for K 413. The pattern of relative elemental abundances $[X/Fe]$ in the atmosphere of K 307b differs only slightly from the solar pattern. Statistically significant differences were found only for the α-process elements: $[X/Fe] = +0.35$ for Na, Mg, Al, and Si. The abundances of the remaining elements, within the error limits, correspond to the star's metallicity.

Let us consider the peculiar chemical composition of the W Vir star in more detail. The abundances of the iron-group metals (chromium, manganese, nickel, and zinc) for K 307 differ only slightly from the iron abundance: $[Met/Fe] = -0.04$. The zinc abundance, which does not change during stellar nucleosynthesis in the interiors of low- and intermediate-mass stars, changes by the same amount as the iron abundance over a wide metallicity range (Sneden *et al.* 1991). Therefore, the inference about the zinc abundance does not depend on the scale (differential or absolute) on which it was determined. For K 307, we obtained a normal (relative to iron) zinc abundance from two lines: $[Zn/Fe] = +0.10$. This circumstance, in combination with the normal $[Ca/Fe]$ and $[Sc/Fe]$ ratios, leads us to conclude that there is no selective separation of chemical elements in the circumstellar shell of K 307. The good agreement between the metallicity of K 307 and the mean metallicity of the globular cluster as a whole also confirms this conclusion.

The CNO elements. The CNO abundances are of fundamental importance in determining the evolutionary status of an evolved star. We determined the carbon abundance, $[C/Fe] = +0.22$, from six low-intensity C I lines (mostly with $W_\lambda < 10$ mÅ). The N I 7442 and 7468 Å lines are stronger ($W_\lambda = 14$ mÅ); the abundances derived from the two lines are in good agreement. The small oxygen overabundance ($[O/Fe] = +0.30$) revealed by the reliably measured infrared oxygen $\lambda7773$ Å triplet lines is mainly attributable to non-LTE effects. The LTE approximation for a high-luminosity star is known to yield

significantly underestimated intensities of the oxygen triplet lines, which results in an overestimation of the oxygen abundance. For example, as follows from the calculations by Takeda (1992), W_λ for an F–G supergiant ($\log g = 1.0$ and a microturbulence of 5 km s^{-1}) in the LTE approximation is a factor of 2 smaller that its value calculated by taking into account the non-LTE level populations. Thus, our derived oxygen overabundance is most likely methodological in origin; for K 307, we observe not an overabundance but a moderate underabundance of oxygen, approximately $[O/Fe] = -0.20$. As a result, for the atmosphere of the W Vir star, carbon may be said to be slightly overabundant, while nitrogen is significantly enhanced and oxygen is underabundant, suggesting that the CN- and ON-cycle products have already been dredged up into the atmospheric surface layers.

Light metals. Let us consider the behavior of the atmospheric abundances of light metals for K 307. We obtained data for sodium and aluminum from the group of odd elements. Sodium is slightly enhanced: $[Na/Fe] = +0.43$, which, as Denisenkov and Ivanov (1987) and Denisenkov (1989) showed, can be a manifestation of the sodium synthesis during hydrogen burning. However, part of the derived Na overabundance is probably attributable to non-LTE effects. Mashonkina *et al.* (2000) analyzed the statistical equilibrium for a sodium atom over a wide range of stellar-atmosphere parameters. These authors showed that, for our subordinate sodium lines in the case of a high-luminosity star with $T_{eff} \approx 5500$ K, an allowance for the overionization of the sodium atom leads to sodium-abundance corrections of about -0.17 dex in comparison with the LTE approximation. Consequently, a third of the sodium overabundance that we found can be methodological rather than evolutionary in origin.

We obtained a high aluminum abundance, $[Al/Fe] = +0.81$, from the $\lambda7084.6$ Å line. The derived aluminum overabundance matches with the oxygen underabundance. According to Shetrone (1996), the Al–O anticorrelation is a common phenomenon for stars in globular clusters with a medium metal underabundance. Klochkova and Samus' (2001) obtained a contradictory pattern for K 413: an overabundance of both O I and Al I. In contrast, for the W Vir star, the ratio of CNO and light elements is similar to that observed for most of the stars near the tip of the giant branch (Drake *et al.* 1992; Kraft *et al.* 1993; Norris and Da Costa 1995), more specifically, an overabundance of N, Al, and Na with an O underabundance.

Of the even α-process elements, we determined the abundance of Mg, Si, S, Ca, and Ti for K 307. Mg, Ca, and Ti are slightly enhanced relative to

iron; the overabundance for them is, on average, $[X/Fe] = +0.14$. In the atmosphere of the W Vir star, Na and Mg are enhanced relative to those for K 413, while the behavior of aluminum is the same for both stars. It should be noted that Ti (as well as Sc) is an intermediate element, which is occasionally considered as the heaviest α-process element or the lightest iron-group metal (Wheeler *et al.* 1989; Armorsky *et al.* 1994).

The silicon overabundance $[Si/Fe] = +0.31$ was reliably determined from two ionization states. A similar relative silicon abundance $[Si/Fe]$ is observed for K 413 and in the atmospheres of most unevolved stars with a metallicity close to the metallicity of M12 (Timmes *et al.* 1995). Consequently, based on the data obtained, we can say that the silicon abundance for the W Vir star is normal.

The sulfur abundance for the two stars studied is large (Table 1). Previously, Klochkova and Samus' (2001) also obtained a similar result for K 413. The large sulfur overabundance observed in the atmospheres of evolved stars has not yet been completely explained. This problem was considered in more detail by Klochkova *et al.* (2002). Israelian and Rebolo (2001) showed that a sulfur overabundance increasing with a decreasing metallicity of the star is also characteristic of metal-poor subdwarfs. This effect could also be responsible for a fraction of the sulfur overabundance in K 307 and its neighbor. Taking into account the absence of a calcium overabundance and a scandium underabundance, we attribute part of the observed sulfur overabundance for these stars to methodological factors.

Heavy metals. Of greatest importance in the abundance pattern of evolved stars are the abundances of heavy metals, which are synthesized through slow neutronization. It is generally believed (Schwarzshild and Härm 1965; Lattanzio and Forestini 1999; Blöcker 2001) that an overabundance of heavy metals due to the neutronization, mixing, and dredging-up of the matter that has passed through these processes in the stellar interior can be observed in the atmospheres of post-AGB stars. As we see from the data in Table 1, these elements are actually enhanced relative to iron in the atmosphere of K 307. The barium abundance was reliably found from two lines to be $[Ba/Fe] = +0.34$; the barium overabundance may also be larger, because we have reason to suspect that the Ba II lines in the spectrum of K 307 have weak emission components that reduce the equivalent widths of the absorption features. The relative abundances of lighter s-process metals (Y, Zr) are also enhanced relative to their solar content;

on average, $[s/Fe] = +0.34$ for them. The overabundance of heavy s-process metals (La, Ce, Nd) is more pronounced: $[s/Fe] = +0.49$.

Europium, which is synthesized during rapid neutronization, is even more enhanced: $[Eu/Fe] = +0.82$. The derived europium overabundance is much higher than the value typical of stars in metal-poor globular clusters synthesized only during the r-process: $[Eu/Fe] = +0.5$ (Shetrone 1996). The ratio $\log(Ba/Eu) \approx +1.1$, which is a standard indicator of the contribution from the r- and s-processes, indicates that the s-process is efficient (Spite 1992). The ratio $[La/Eu] \approx -0.14$ also argues for the s-process (McWilliam 1997).

In general, although the metallicities are in good agreement, the chemical composition of K 307 differs from that of the star K 413 in M12. Unfortunately, the CNO abundances for K 413 were determined unreliably by Klochkova and Samus' (2001). However, the abundances of α-process elements and heavy metals were determined reliably for the two stars. Therefore, it can be said with confidence that Y, Zr, Ba, La, Ce, and Eu in the atmosphere of K 307 are significantly enhanced, compared to those for K 413.

Thus, we may conclude that we detected the dredge-up of CN- and ON-cycle and s-process elements into the observed atmospheric layers of K 307. The presence or absence of an overabundance of s-process elements in the atmospheres of supergiants, including post-AGB ones, is somehow related to such fundamental parameters of the star as its initial mass and mass-loss rate, which determine the course of the evolution of a specific star. Gonzalez and Wallerstein (1994) concluded that the main parameter that determines whether the synthesis products are dredged up into the atmosphere of a post-AGB star is its luminosity. Using K 307 as an example, we confirmed the conclusion by Gonzalez and Wallerstein (1994) that the overabundances of CNO and s-process elements correlate.

It is instructive to compare the parameters of K 307 and a canonical post-AGB object, which the highly evolved star ROA 24 in the globular cluster ω Cen is believed to be; based on high-resolution spectra, Gonzalez and Wallerstein (1992) determined the detailed chemical composition for this star. The chemical peculiarities (the large overabundances of the CNO-elements and s-process metals detected in the atmosphere of ROA 24) of the brightest star in the system of Galactic globular clusters in combination with its high luminosity strongly suggest that this is a post-AGB object that is evolving toward the state of a white dwarf. We compared our elemental abundances for the W Vir star with the data for ROA 24 and concluded that the chemical elements

for these stars have similar abundance patterns. However, there are also differences: both quantitative, in the overabundances of certain elements (particularly CNO), and qualitative, in the opposite behavior of the oxygen and aluminum abundances. The difference between the luminosities (and, hence, masses) of the stars being compared appears to be mainly responsible for these differences: according to Gonzalez and Wallerstein (1992), the absolute magnitude of ROA 24 is $M_V = -3^m66$, while the W Vir is fainter by one magnitude, $M_V = -2^m6$. The supergiant ROA 24 has already crossed the instability strip at least once, while K 307 is in the stage of pulsation instability. The star V84 in the globular cluster M5, one of the variable F and G stars in globular clusters studied by Gonzalez and Lambert (1997), is the object that is closest to the W Vir star in parameters (temperature, luminosity, metallicity, sodium and aluminum overabundances combined with an oxygen underabundance, overabundance of s-process elements).

Here, it is pertinent to recall the hypothesis by Luck and Bond (1989) that the large underabundance of s-process elements in field W Vir stars is attributable to the effect where extremely metal-poor stars have virtually exhausted their hydrogen; as a result, an enhanced (relative to the left hydrogen) metal abundance is observed, while the relative elemental abundances (including the underabundance of s-process elements) correspond to extremely metal-poor stars. The results of our study for the W Vir in the globular cluster are inconsistent with this hypothesis. First, the metallicity of the W Vir star, within the error limits, is equal to the metallicity of the other two luminous stars that we studied by the same method. We have no sufficient reason to suggest that W Vir initially had a low metal abundance and squandered such an amount of hydrogen that its metallicity normalized to the left hydrogen is equal to the metallicity of other cluster stars. Second, in contrast to the field W Vir stars, K 307 exhibits an enhancement of heavy elements (relative to iron). Third, the estimate obtained in the LTE approximation from the helium and hydrogen emission spectrum points to a helium abundance that does not exceed its solar value.

We emphasize that the detailed chemical composition of post-AGB stars in globular clusters matches the elemental abundances in the atmospheres of stars that are candidates for protoplanetary nebulae in the Galactic field. A great deal of data for the latter has been published in the last decade (see, e.g., Klochkova (1995); van Winckel and Reyners (2000); Klochkova *et al.* (2001, 2002); and references therein).

CONCLUSIONS

The high-resolution spectra for the W Vir star V1 = K 307 in the globular cluster M12 and its nearest neighbor, a faint star ($m_{pg} = 14^m$) located at an angular distance of $\delta < 1$ arcsec from the W Vir star, have been studied for the first time. The radial velocities of the two stars, $V_r = -40.6$ and -39.2 km s^{-1}, confirm that they belong to this cluster.

We determined the fundamental parameters for the two stars ($T_{eff} = 5600$ K, $\log g = 1.3$, and $T_{eff} = 4200$ K, $\log g = 1.0$ for the W Vir star and its neighbor, respectively) and their detailed chemical composition. The derived metallicities for the two stars ([Fe/H] = -1.27 and -1.22) are in good agreement with the metallicity of the globular cluster M12. In the atmosphere of the W Vir star, we found CNO abundances that changed during its evolution: an enhanced carbon abundance, [C/Fe] = $+0.30$ dex, in combination with a large nitrogen overabundance, [N/Fe] = $+1.15$ dex, and an oxygen underabundance, [O/Fe] ≈ -0.2 dex. The C/O ratio is ≥ 1. The light metals Mg, Ca, and Ti are slightly enhanced relative to iron; on average, [X/Fe] = $+0.14$. The sodium and silicon overabundances are larger, [Na/Fe] = $+0.43$ and [Si/Fe] = $+0.31$. We found an enhanced (relative to iron) abundance of the light metals synthesized during slow neutronization: [X/Fe] = $+0.34$ for Y, Zr, and Ba. The behavior of CNO and heavy metals suggests that the synthesis products of these elements are effectively dredged up to the stellar surface. The overabundance of the heavier metals La, Ce, and Nd relative to iron is larger: [X/Fe] = $+0.49$. The largest overabundance was found for europium, [Eu/Fe] = $+0.82$. The high luminosity $\log L/L_\odot = 2.98$, the chemical peculiarities, and the spectroscopic peculiarity are consistent with the post-AGB evolution of a star with a core mass $M/M_\odot = 0.52$ in the instability strip.

The pattern of relative elemental abundances [X/Fe] in the atmosphere of the neighboring star K 307b is solar. Statistically significant differences were found only for the α-process elements: [X/Fe] = $+0.35$ for Na, Mg, Al, and Si.

The spectrum of the W Vir star exhibits the Hα and Hβ absorption–emission profiles and the HeI $\lambda 5876$ Å emission profile attributable to the shock passage in the stellar atmosphere. However, the radial-velocity pattern is in conflict with the formation conditions for a strong shock wave. Apart from this peculiarity, we detected absorption bands in the spectrum of K 307 whose positions allow them to be identified with the so-called diffuse interstellar bands.

ACKNOWLEDGMENTS

REFERENCES

1. H. A. Abt, Astrophys. J., Suppl. Ser. **1**, 63 (1954).
2. T. F. Adams and J. I. Castor, Astrophys. J. **230**, 826 (1979).
3. B. J. Armorsky, C. Sneden, G. E. Langer, and R. P. Kraft, Astron. J. **108**, 1364 (1994).
4. A. P. Bernat and D. L. Lambert, Publ. Astron. Soc. Pac. **90**, 520 (1978).
5. T. Blöcker, Astrophys. Space Sci. **275**, 1 (2001).
6. E. Brocato, R. Buonanno, Y. Malakhova, and A. M. Piersimoni, Astron. Astrophys. **311**, 778 (1996).
7. E. Carretta and R. C. Gratton, Astron. Astrophys., Suppl. Ser. **121**, 95 (1997).
8. J. L. Castor, L. F. Smith, and D. van Blerkom, Astrophys. J. **159**, 1119 (1970).
9. C. M. Clement, A. Muzzin, Q. Dufton, *et al.*, Astron. J. **122**, 2587 (2001).
10. C. M. Clement, H. Sawyer Hogg, and A. Yee, Astron. J. **96**, 1642 (1988).
11. G. S. da Costa and T. E. Armandroff, Astron. J. **109**, 2533 (1995).
12. P. A. Denisenkov, Pis'ma Astron. Zh. **14**, 1023 (1988) [Sov. Astron. Lett. **14**, 435 (1988)].
13. P. A. Denisenkov and V. V. Ivanov, Pis'ma Astron. Zh. **13**, 520 (1987) [Sov. Astron. Lett. **13**, 214 (1987)].
14. J. Drake, V. V. Smith, and N. B. Suntzeff, Astrophys. J. **395**, L95 (1992).
15. Yu. A. Fadeev, Astron. Zh. **78**, 421 (2001) [Astron. Rep. **45**, 361 (2001)].
16. A. V. Fokin, Mon. Not. R. Astron. Soc. **250**, 258 (1991).
17. M. Geffert, H.-J. Tucholke, Ts. B. Georgiev, and J.-F. LeCampion, Astron. Astrophys., Suppl. Ser. **91**, 487 (1991).
18. D. Gillet, *The Impact of Very High S/N Spectroscopy on Stellar Physics,* Ed. by G. Cayrel de Strobel and M. Spite (Kluwer Acad., Dordrecht, 1988), p. 143.
19. D. Gillet, E. Maurice, and D. Baade, Astron. Astrophys. **128**, 384 (1983).
20. R. A. Gingold, Mem. Soc. Astron. Ital. **56**, 169 (1985).
21. G. Gonzalez and L. Lambert, Astron. J. **114**, 341 (1997).
22. G. Gonzalez and G. Wallerstein, Mon. Not. R. Astron. Soc. **254**, 343 (1992).
23. G. Gonzalez and G. Wallerstein, Astron. J. **108**, 1325 (1994).
24. N. Grevesse, A. Noels, and A. J. Sauval, ASP Conf. Ser. **99**, 117 (1996).
25. W. E. Harris, Astron. J. **112**, 1487 (1996).
26. H. C. Harris, J. M. Nemec, and J. E. Hesser, Publ. Astron. Soc. Pac. **95**, 256 (1983).
27. L. M. Hobbs, Astrophys. J. **157**, 135 (1969).
28. G. Israelian and R. Rebolo, Astrophys. J. **557**, L43 (2001).
29. C. de Jager, Rech. Astr. Obs. Utrecht **13**, 1 (1952).
30. A. H. Joy, Astrophys. J. **110**, 105 (1949).
31. V. G. Klochkova, Mon. Not. R. Astron. Soc. **272**, 710 (1995).
32. V. G. Klochkova, V. E. Panchuk, and R. Szczerba, in *Post-AGB Objects as a Phase of Stellar Evolution*, Ed. by R. Szczerba and S. K. Gorny (Kluwer Acad., Dordrecht, 2001), p. 265.
33. V. G. Klochkova, V. E. Panchuk, and N. S. Tabolzhskaya, Pis'ma Astron. Zh. **28**, 56 (2002) [Astron. Lett. **28**, 49 (2002)].
34. V. G. Klochkova and N. N. Samus, Astron. Astrophys. **378**, 455 (2001).
35. R. P. Kraft, C. Sneden, G. E. Langer, and N. D. Shetrone, Astron. J. **106**, 1490 (1993).
36. R. L. Kurucz, CD-ROMs (1993).
37. F. Küstner, Veröff. Astron. Inst. Bonn. **26**, 1 (1933).
38. J. Lattanzio and M. Forestini, *IAU Symp. No. 191: Asymptotic Giant Branch Stars,* Ed. by T. Le Bertre, A. Lébre, and C. Waelkens (Publ. Astron. Soc. Pac., Paris, 1999), p. 31.
39. A. Lèbre and D. Gillet, Astron. Astrophys. **255**, 221 (1992).
40. R. E. Luck and H. E. Bond, Astrophys. J. **342**, 476 (1989).
41. Yu. N. Malakhova, A. N. Gerashchenko, Z. I. Kadla, Int. Bull. Var. Stars, No. 4434 (1997).
42. J. M. Marlborough, Astrophys. J. **156**, 135 (1969).
43. L. I. Mashonkina, V. V. Shimanskiǐ, and N. A. Sakhibullin, Astron. Zh. **77**, 893 (2000) [Astron. Rep. **44**, 790 (2000)].
44. A. McWilliam, Ann. Rev. Astron. Astrophys. **35**, 503 (1997).
45. G. Münch, Astrophys. J. **112**, 266 (1950).
46. J. E. Norris and G. S. Da Costa, Astrophys. J. **441**, L81 (1995).
47. V. E. Panchuk, Probl. Kosm. Fiz., No. 6, 199 (1971).
48. V. E. Panchuk, I. D. Najdenov, V. G. Klochkova, *et al.*, Bull. Spec. Astrofiz. Obs. **44**, 127 (1998).
49. A. Raga, G. Wallerstein, and J. B. Oke, Astrophys. J. **347**, 1107 (1989).
50. G. A. Rutledge, J. E. Hesser, P. B. Stetson, *et al.*, Publ. Astron. Soc. Pac. **109**, 883 (1997).
51. H. Sawyer-Hogg, Publ. Domin. Astrophys. Obs. **7** (5) (1938a).
52. H. Sawyer-Hogg, Publ. David Dunlap Obs. **1** (2) (1938b).
53. M. D. Shetrone, Astron. J. **112**, 1517 (1996).
54. M. Schwarzshild and R. Härm, Astrophys. J. **142**, 855 (1965).

55. J. M. Shull and C. F. McKee, Astrophys. J. **227**, 131 (1979).

56. C. Sneden, R. G. Gratton, and D. A. Crocker, Astron. Astrophys. **246**, 354 (1991).

57. M. Spite, *IAU Symp. No. 149: The Stellar Populations of Galaxies,* Ed. by B. Barbuy and A. Renzini (Kluwer Acad., Dordrecht, 1992), p. 123.

58. Y. Takeda, Publ. Astron. Soc. Jpn. **44**, 309 (1992).

59. F. X. Timmes, S. E. Woosley, and T. A. Weaver, Astrophys. J., Suppl. Ser. **98**, 617 (1995).

60. G. Wallerstein, Astrophys. J. **130**, 560 (1959).

61. J. C. Wheeler, C. Sneden, and J. W. Truran, Ann. Rev. Astron. Astrophys. **27**, 279 (1989).

62. L. A. Willson, Astrophys. J. **205**, 172 (1976).

63. H. van Winckel and M. Reyners, Astron. Astrophys. **354**, 135 (2000).

64. B. Wolf, O. Stahl, M. J. H. de Groot, and C. Sterken, Astron. Astrophys. **99**, 351 (1981).

65. R. J. Zinn, E. B. Newel, and J. B. Gibson, Astron. Astrophys. **18**, 390 (1972).

Translated by V. Astakhov

FG Sagittae: New Observations in the R CrB Photometric Phase

V. P. Arkhipova[*], N. P. Ikonnikova, G. V. Komissarova, R. I. Noskova, S. Yu. Shugarov, and V. F. Esipov

Sternberg Astronomical Institute, Universitetskii pr. 13, Moscow, 119992 Russia
Received June 5, 2003

Abstract—In 1999–2002, we continued our photometric and spectroscopic observations of FG Sge. This star has been in a new R CrB photometric phase since 1992. We constructed the $BVRI$ light curves and studied the behavior of the color indices as a function of the fading amplitude. As previously, all of the three deep minima observed during this period were found to be blue on the descent; this was interpreted as the result of strong stellar light scattering in dust clouds formed on the line of sight. We analyzed the wavelength dependence of extinction in the circumstellar shell outside fadings, which was similar to Whitford's standard reddening law. Low-resolution spectroscopic observations allowed us to study the changes in the intensities of Swan bands and the Na I D doublet during deep and shallow (up to 1^m) fadings. We confirmed the reversal of the spectrum of the extended stellar envelope on the descending branches of deep minima. © 2003 MAIK "Nauka/Interperiodica".

Key words: *stars—variable and peculiar, planetary nebula nuclei, FG Sge.*

INTRODUCTION

The central star of the planetary nebula He 1-5, the well-known variable FG Sge, has long been a whetstone on which the details of the theory of late stellar evolution are sharpened. The unprecedented secular changes in brightness and temperature, the hypertrophic chemical composition of the atmosphere in the early 1970s, the unexpected appearance of deep fadings in the early 1990s due to the formation of dust clouds in the circumstellar shell, and the presence of a classical planetary nebula around the star—all of these observational facts have stimulated the theoretical studies of post-AGB stellar evolution and provided a deeper insight into the stage of helium shell flashes and, in particular, the role of the final helium flash in the cooling phase of a white dwarf—the central star of the planetary nebula (Schoenberner 1983; Iben 1984; Bloecker 1995; Herwig *et al.* 1997; Bloecker and Schoenberner 1997; Lawlor and Mac Donald 2003). FG Sge is currently recognized as the brightest of the three known objects in the stage of a final helium flash in planetary nebula nuclei.

Multicolor photometric observations, mainly in three colors (UBV) before the early 1990s and in a wider wavelength range ($UBVRIJHKLM$) in the last decade, have yielded important information about the parameters of the star at various stages of its evolution. Three-color photometry of FG Sge has been systematically performed since 1967 at the Crimean Station of the Sternberg Astronomical Institute (SAI). Several thousand UBV-magnitude estimates have been obtained in the past 35 years. They were published in a series of papers by Arkhipova (1982, 1988, 1993). The photometric behavior of the star was analyzed in detail over the period 1967–1991: we found brightness and color trends attributable to a secular decrease in stellar temperature, studied quasi-periodic pulsations, and showed the amplitude and duration of the pulsation cycle to increase as the star cools down (Arkhipova 1993).

Figure 1 shows our V light curve from 1973 to 1991, which has not been published previously in complete form. It strongly suggests pulsations of the star and an increase in their period and amplitude with time. The pulsation amplitude and shape differed greatly at different times; the pulsations were most regular when the star passed through the instability strip in the spectrum—luminosity diagram. We have repeatedly observed a halt in brightness pulsations with a duration of one or two cycles, following which a new buildup began. All of these facts pointed to the absence of a strict periodicity that may be attributable to the presence of several oscillation frequencies. However, on average, the observed pulsation quasi-period increased over 25 years from 60 to 110–120 days (by 1992). This increase resulted from the decrease in the mean density of the star because its expansion.
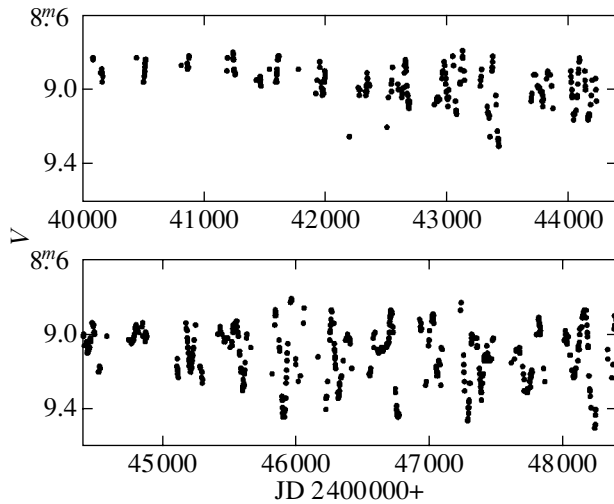
[*]E-mail: `vera@sai.msu.ru`

Fig. 1. Segments of the V light curve for FG Sge before 1992.

A new photometric phase of the star began in 1992, when the brightness of FG Sge suddenly began to decline at a rate of about $0^m.1$ per day and reached 14^m in V. The amplitude of the brightness decline was more than 5^m. In addition, the $B-V$ and $U-B$ color indices systematically decreased as the star was descending to its minimum by more than 1^m in general. In succeeding years, these fadings were repeated with various amplitudes; a significant decrease in color indices on the descent and, as a rule, their return to the initial value after the emergence from the minimum have always been observed during the deepest (by $5-7^m$) fadings. During fadings by $1-2^m$, the color indices usually exhibit only small changes. We called the new photometric phase of FG Sge that began in 1992 an R CrB phase, by analogy with the photometric behavior of this type of stars. As in R CrB stars, the deep fadings of FG Sge are attributable to the formation of dust in the matter ejected by the star, which was first proved by infrared observations (Woodward *et al.* 1993). Our observations of the star after 1991 were published in papers by Arkhipova (1994, 1996) and Arkhipova *et al.* (1999).

From 1992 until 2002, FG Sge experienced at least ten R CrB fadings. The deepest photometric minima were in 1998, 1999, 2001, and 2002.

In this paper, we present our photometric observations of the star from 1999 until 2002. Apart from the UBV bands, the observations have also been carried out since 1997 in the R and I bands of Johnson's multicolor system. In addition, we used our spectroscopic observations to search for a correlation between the spectroscopic and photometric variations of FG Sge in the R CrB phase. Below, we also consider
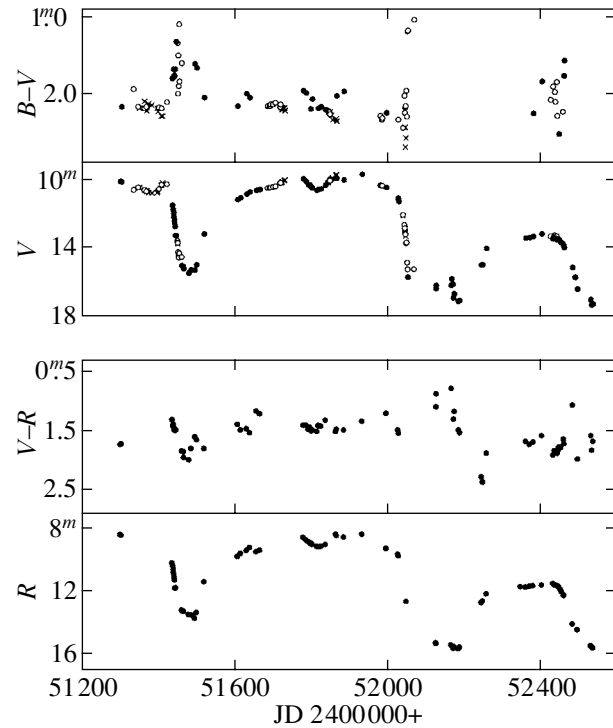
Fig. 2. The light and color curves for FG Sge in 1999–2002. Different symbols refer to different detectors: the crosses and open circles represent the photoelectric observations corrected for the contributions from the companion and the nebula, respectively; the filled circles represent the CCD observations.

the extinction parameters of the star in the gas–dust circumstellar shell formed during mass ejections.

$UBVRI$ PHOTOMETRY OF FG Sge IN 1999–2002

We observed the star with two Zeiss-600 telescopes at the Crimean Station of the SAI. We used a UBV photometer for photoelectric measurements and two photometers equipped with a CCD camera with SBIG ST-6 and ST-7 CCD arrays for $BVRI$ brightness measurements.

In our photoelectric observations, $BD + 19°4319$ ("x" in our old notation) was the comparison star. In our CCD brightness measurements, the comparison star was mainly the optical companion of FG Sge located $7''$ east of it; we had determined its magnitudes previously (Arkhipova 1996; Arkhipova *et al.* 1999) and redetermined them for this paper. Finally, we took the following magnitudes for the companion of FG Sge in Johnson's system: $B(com) = 13^m.84$, $V(com) = 12^m.33$, $R(com) = 11^m.19$, $I(com) = 10^m.33$. In addition to this companion, we also occasionally used other photometric standard stars near FG Sge from the above papers.

Table 1. The photoelectric observations of FG Sge in 1999−2000

JD 2400000+	V	B	U	$B{-}V$	$U{-}B$	d	JD 2400000+	V	B	U	$B{-}V$	$U{-}B$	d
51 336	$10\overset{m}{.}61$	$12\overset{m}{.}55$	$14\overset{m}{.}43$	$1\overset{m}{.}94$	$1\overset{m}{.}88$	$27''$	51 780	$9\overset{m}{.}86$	$11\overset{m}{.}97$	$13\overset{m}{.}69$	$2\overset{m}{.}11$	$1\overset{m}{.}72$	$27''$
51 348	10.46	12.63	14.54	2.17	1.90	27	51 782	9.92	12.03	13.56	2.11	1.53	27
51 351	10.49	12.68	14.78	2.19	2.10	13	51 788	10.06	12.21	13.92	2.15	1.71	27
51 364	10.63	12.82	14.72	2.19	1.90	27	51 789	10.09	12.24	14.06	2.15	1.82	27
51 364	10.63	12.73	15.09	2.10	2.36	13	51 791	10.18	12.36	13.91	2.18	1.55	27
51 369	10.70	12.87	14.34	2.17	1.47	27	51 806	10.44	12.60	14.94	2.16	2.34	27
51 369	10.66	12.88	14.58	2.22	1.70	13	51 815	10.53	12.69	14.49	2.16	1.80	27
51 370	10.70	12.88	14.80	2.18	1.92	13	51 819	10.54	12.73	14.30	2.19	1.57	27
51 374	10.77	12.90	14.75	2.13	1.85	13	51 824	10.52	12.69	14.43	2.17	1.74	27
51 383	10.79	12.94	15.29	2.15	2.35	13	51 834	10.39	12.62	14.03	2.23	1.41	27
51 397	10.78	12.97	15.13	2.19	2.16	13	51 838	10.31	−	−	−	−	27
51 399	10.71	12.94	16.79	2.23	3.85	13	51 841	10.25	12.47	14.29	2.22	1.82	27
51 402	10.56	12.74	14.56	2.18	1.82	27	51 843	10.18	12.39	14.59	2.21	2.199	27
51 408	10.33	12.62	15.20	2.29	2.58	13	51 844	10.17	12.39	14.24	2.22	1.85	27
51 409	10.30	12.49	14.29	2.19	1.80	27	51 844	10.18	12.42	14.40	2.24	1.98	13
51 411	10.20	12.49	14.32	2.29	1.83	13	51 847	10.12	12.36	14.32	2.24	1.96	27
51 423	10.28	12.39	14.06	2.11	1.67	27	51 849	10.05	12.32	14.40	2.27	2.08	27
51 451	13.62	14.96	−	1.34	−	27	51 850	10.06	12.33	14.32	2.27	1.99	27
51 451	13.77	−	−	−	−	13	51 850	10.05	12.29	14.51	2.24	2.22	13
51 452	13.73	15.73	17.17	2.00	1.46	27	51 853	9.97	12.25	14.32	2.28	2.07	13
51 453	14.25	15.75	−	1.50	−	27	51 856	9.92	12.26	14.14	2.34	1.88	13
51 454	14.48	16.38	−	1.90	−	27	51 865	9.74	12.07	14.32	2.33	2.25	13
51 455	14.59	15.67	17.13	1.10	1.46	27	51 867	9.73	12.09	14.32	2.36	2.23	13
51 456	14.33	16.17	−	1.84	−	27	51 982	10.34	12.63	14.08	2.29	1.45	27
51 462	14.55	16.15	−	1.60	−	27	51 986	10.38	12.72	15.32	2.34	2.60	27
51 687	10.50	12.66	14.57	2.16	1.91	27	51 987	10.37	12.69	14.92	2.32	2.23	27
51 692	10.49	12.65	14.56	2.16	1.91	27	52 029	11.11	13.45	15.44	2.34	1.99	27
51 693	10.45	12.61	14.08	2.16	1.47	27	52 041	12.08	14.53	15.64	2.45	1.11	27
51 695	10.47	12.61	14.13	2.14	1.52	27	52 041	12.13	−	−	−	−	13
51 701	10.44	12.58	14.34	2.14	1.76	27	52 045	12.66	14.69	−	2.03	−	27
51 707	10.40	12.52	14.23	2.12	1.71	27	52 046	12.87	15.12	16.38	2.25	1.26	27
51 720	10.21	12.38	13.96	2.17	1.58	27	52 046	12.88	15.32	−	2.44	−	13
51 721	10.20	12.34	13.86	2.14	1.52	27	52 047	13.15	15.33	−	2.18	−	27
51 722	10.18	12.36	14.07	2.18	1.71	13	52 047	13.11	15.81	−	2.70	−	13
51 724	10.13	12.34	14.34	2.21	2.00	13	52 048	13.22	15.38	−	2.16	−	27
51 725	10.14	12.33	14.29	2.19	1.96	13	52 048	13.33	15.91	−	2.58	−	13
51 730	10.06	12.25	14.22	2.19	1.97	13	52 050	13.74	15.70	17.31	1.96	1.61	27
51 732	10.02	12.24	14.09	2.22	1.85	13	52 051	13.70	16.00	16.70	2.30	0.70	27
51 750	9.70	11.86	13.75	2.16	1.89	27	52 053	14.88	16.07	−	1.19	−	27
51 754	9.66	11.82	13.64	2.16	1.82	27	52 054	15.28	16.46	−	1.18	−	27
51 761	9.71	11.86	13.49	2.15	1.63	27	52 071	15.27	16.31	−	1.04	−	27
51 765	9.63	11.77	13.50	2.14	1.73	27	52 428	13.34	15.42	−	2.08	−	27
51 767	9.68	11.82	13.55	2.14	1.73	27	52 434	13.48	15.39	−	1.91	−	27
51 768	9.70	11.84	13.38	2.14	1.54	27	52 439	13.27	15.25	−	1.98	−	27
51 776	9.80	11.97	13.41	2.17	1.44	27	52 440	13.37	15.48	−	2.11	−	27
51 777	9.83	11.98	13.81	2.15	1.83	27	52 444	13.34	15.19	−	1.85	−	27
51 778	9.83	11.97	13.78	2.14	1.81	27	52 445	13.54	15.83	−	2.29	−	27
51 779	9.83	11.97	−	2.14	−	27	52 460	13.77	16.01	−	2.24	−	27

Table 2. The photometric observations of FG Sge in 1999−2002

JD 2400000+	B	V	$B-V$	R	$V-R$	I	$V-I$	Detector
51 302	−	10^m11	−	8^m38	1^m73	7^m89	2^m22	ST-7
51 305	12^m31	10.14	2^m17	8.42	1.72	7.90	2.24	ST-7
51 438	13.31	11.51	1.80	10.20	1.31	9.24	2.27	ST-7
51 440	−	11.77	−	10.36	1.41	9.40	2.37	ST-7
51 441	13.62	11.94	1.68	10.55	1.39	9.47	2.47	ST-7
51 442	13.98	12.20	1.78	10.78	1.42	9.65	2.55	ST-7
51 443	14.14	12.38	1.76	10.93	1.45	9.82	2.56	ST-7
51 444	14.36	12.59	1.77	11.11	1.48	9.99	2.60	ST-7
51 445	14.43	12.75	1.68	11.28	1.47	10.13	2.62	ST-7
51 446	−	13.28	−	11.79	1.49	−	−	ST-7
51 448	14.60	13.28	1.32	11.80	1.48	10.59	2.69	ST-7
51 463	−	15.05	−	13.21	1.84	11.53	3.52	ST-7
51 467	−	15.11	−	13.26	1.85	11.53	3.58	ST-7
51 468	−	15.23	−	13.28	1.95	11.55	3.68	ST-7
51 482	−	15.48	−	13.49	1.99	11.76	3.72	ST-7
51 487	−	15.31	−	13.51	1.80	11.83	3.48	ST-7
51 497	16.93	15.32	1.61	13.72	1.60	11.83	3.49	ST-7
51 502	16.66	15.00	1.66	13.35	1.65	11.64	3.36	ST-7
51 522	15.25	13.20	2.05	11.40	1.80	10.23	2.97	ST-7
51 609	13.34	11.18	2.16	9.79	1.39	8.77	2.41	ST-6
51 617	−	11.07	−	9.59	1.48	8.74	2.33	ST-6
51 632	12.86	10.86	2.00	9.40	1.46	8.32	2.54	ST-7
51 641	12.79	10.74	2.05	9.21	1.53	−	−	ST-7
51 658	−	10.64	−	9.48	1.16	8.17	2.57	ST-6
51 667	−	10.59	−	9.38	1.21	−	−	ST-6
51 781	11.92	9.96	1.96	8.56	1.40	7.61	2.35	ST-7
51 788	12.14	10.12	1.99	8.72	1.43	7.79	2.33	ST-7
51 794	−	10.30	−	8.83	1.47	7.86	2.44	ST-7
51 798	−	10.32	−	8.88	1.44	7.86	2.46	ST-7
51 800	12.61	10.40	2.20	8.94	1.46	7.87	2.53	ST-7
51 802	−	10.44	−	8.94	1.50	7.91	2.53	ST-7
51 804	12.56	10.49	2.07	9.01	1.48	7.96	2.53	ST-7
51 817	−	10.65	−	9.14	1.51	8.03	2.62	ST-7
51 820	12.77	10.58	2.19	9.17	1.41	8.13	2.45	ST-6
51 827	12.73	10.56	2.17	9.14	1.42	8.05	2.51	ST-6
51 839	12.54	10.33	2.21	9.01	1.32	7.84	2.49	ST-6
51 866	−	9.87	−	8.36	1.51	7.56	2.31	ST-7
51 868	11.95	9.92	2.03	8.45	1.47	7.58	2.34	ST-7
51 887	11.99	10.02	1.97	8.54	1.48	7.59	2.43	ST-7
51 935	−	9.70	−	8.36	1.34	−	−	ST-6

Table 2. (Contd.)

| JD 2400000+	B	V	$B-V$	R	$V-R$	I	$V-I$	Detector
51 998	12.73	10.48	2.25	9.28	1.20	−	−	ST-6
52 029	−	11.14	−	9.65	1.48	8.72	2.42	ST-7
52 031	−	11.30	−	9.76	1.54	8.74	2.56	ST-7
52 051	−	−	−	12.66	−	−	−	ST-6
52 055	−	15.73	−	−	−	12.39	3.34	ST-6
52 129	−	16.40	−	15.31	1.09	13.17	3.23	ST-6
52 130	−	16.21	−	15.34	0.87	13.19	3.02	ST-6
52 169	−	16.20	−	15.42	0.78	13.51	2.69	ST-6
52 175	−	16.94	−	15.64	1.30	14.02	2.92	ST-7
52 177	−	16.70	−	15.53	1.17	13.97	2.73	ST-7
52 188	−	17.13	−	15.65	1.48	13.96	3.17	ST-7
52 191	−	17.08	−	15.56	1.53	14.02	3.06	ST-7
52 248	−	15.01	−	12.73	2.28	11.36	3.65	ST-7
52 251	−	15.01	−	12.64	2.37	11.22	3.79	ST-7
52 261	−	14.04	−	12.17	1.88	10.81	3.23	ST-7
52 350	−	−	−	11.72	−	10.45	−	ST-6
52 364	−	13.44	−	11.76	1.68	10.45	2.99	ST-6
52 374	−	13.42	−	11.69	1.73	10.40	3.02	ST-6
52 383	15.61	13.35	2.26	11.66	1.69	10.39	2.96	ST-6
52 406	15.04	13.20	1.84	11.62	1.58	10.36	2.84	ST-6
52 435	−	13.43	−	11.52	1.91	10.51	2.92	ST-6
52 439	−	13.46	−	11.62	1.84	10.14	3.32	ST-7
52 440	−	13.47	−	11.60	1.87	10.19	3.28	ST-7
52 442	−	13.47	−	11.61	1.87	10.18	3.29	ST-7
52 446	−	13.54	−	11.66	1.88	10.24	3.30	ST-7
52 448	−	13.51	−	11.68	1.84	10.26	3.25	ST-7
52 450	16.04	13.51	2.53	11.72	1.78	10.33	3.18	ST-7
52 455	−	13.68	−	11.90	1.78	10.52	3.16	ST-7
52 458	15.29	−	−	12.04	−	10.66	−	ST-6
52 463	15.67	13.90	1.77	12.26	1.64	10.95	2.95	ST-6
52 464	15.57	14.00	1.57	12.28	1.72	10.96	3.04	ST-6
52 469	16.43	14.28	2.15	12.60	1.68	11.23	3.05	ST-7
52 472	16.55	14.42	2.13	12.83	1.59	11.49	2.93	ST-7
52 476	16.78	14.80	1.98	13.30	1.50	11.87	2.93	ST-7
52 486	−	15.17	−	14.10	1.06	−	−	ST-6
52 493	−	15.74	−	−	−	−	−	ST-6
52 499	−	16.44	−	14.46	1.98	12.67	3.77	ST-6
52 534	−	17.05	−	15.47	1.58	13.38	3.67	ST-7
52 537	−	17.34	−	15.51	1.83	13.37	3.97	ST-7
52 540	−	17.30	−	15.62	1.68	13.52	3.78	ST-7
52 551	−	−	−	−	−	13.8	−	ST-6
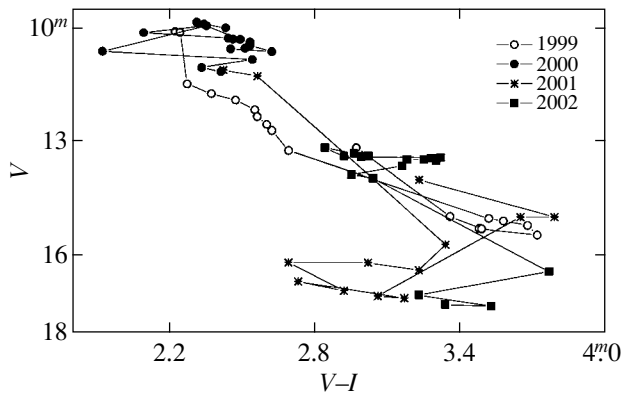
Fig. 3. The $V-I$ color$-V$ magnitude diagram for FG Sge.

In our photoelectric observations, we used $13''$ and $27''$ photometer apertures. The measurements with these apertures should be corrected for the contributions from the nebula surrounding the star and the companion. The magnitudes in each band are known from our previous measurements (Arkhipova 1996). We obtained photoelectric data mainly for the star's brighter states and carried out CCD photometric measurements when it faded below $12^m.5$ in V.

Table 1 gives our photoelectric UBV magnitudes of the star, while Table 2 gives our $BVRI$ CCD observations for 1999−2002. Figure 2 shows the light and color curves for the same period. The accuracy of the magnitude estimates depends significantly on the brightness level, being about $0^m.01$ in a bright state and about $0^m.05$ or even $0^m.2$ at deep photometric minima. The error in the color indices can reach $0^m.3$ at the deepest minima.

We see that FG Sge experienced three deep R CrB fadings over the last four years; the minimum of 2001 was double, as in 1994, but much deeper, and the brightness did not rise to its maximum by the beginning of the next minimum in 2002 but stopped at 13^m in V. Note the similarity between the brightness decline amplitudes in the V, R, and I bands.

The deep minima of 1999 and 2001 were both blue on the descent, as the previous minima of 1992, 1994, 1995, 1998, and, probably, 1996, although nobody has obtained any estimate of the $B-V$ color index for the latter on the descending branch. Note that the R CrB photometric phase in 1992 began precisely from a blue minimum; we performed its observations (Arkhipova 1994). After the minimum brightness is reached, the $B-V$ color index generally increases rapidly, reaches a maximum, and then decreases as the star emerges from its minimum, returning to the original, or a slightly larger value.

During the shallow ($\sim 1^m$) fading in 2000, the $B-V$ color index was nearly constant on the descending branch and began to systematically increase only on the ascending branch.

In 2002, we carried out our photoelectric observations when the V magnitude was $13-14^m$ and the errors in $B-V$ reached $\pm 0^m.2$. Therefore, it is difficult to judge whether the magnitude correlates with the color on the descending branch.

The $V-R$ color index shows a significant scatter because of the measurement errors, which reach $\pm 0^m.2$ at a low brightness, and, possibly, because of the difference between the two instrumental R systems used, although they were reduced to Johnson's standard system. The planetary nebula surrounding FG Sge, which is very bright in the range $\lambda\lambda 6500-6600$ Å because of the strong Hα and [N II] emission lines, severely complicates R-band measurements. The nebular contribution in B- and V-band CCD measurements is smaller and can be accurately taken into account. FG Sge has, on average, $V-R = +1.4$ in a bright state.

It is important to note the main features in the $V-R$ behavior in the R CrB photometric phase:

(1) during the deep fadings in 2001 and 2002, when the star reached 17^m in V, the $V-R$ color index decreased only slightly on the descending branch and, after the minimum was reached, began to appreciably increase;

(2) at the shallower minimum of 1999, the $V-R$ color index systematically and significantly increased as the star faded, and it decreased by $0^m.4$ after the minimum brightness (15^m V) was reached;

(3) at the shallow minimum of 2000, the $V-R$ color index increased slightly on the descending branch and reached $V-R = +1.5^m$ near the time of minimum brightness (about 11^m in V).

In comparison with $V-R$, the $V-I$ color index exhibits an appreciably larger amplitude of its variations during fadings. Figure 3 shows the $V-I$ variations with V in 1999−2002.

During the deep double fading in 2001, $V-I$ rapidly increased from $+2^m.5$ to $+3^m.3$ by the first minimum. Subsequently, this color index initially decreased and then increased to $V-I = +3^m.7$ on the ascent to $V = 15^m$.

At the deep minimum of 2002, the descending branch was covered by observations starting from $13^m.5$ V at $V-I = +3^m.1$, and the $V-I$ color index reached $+3^m.5$ at the photometric minimum itself.

During the shallower fading in 1999, the $V-I$ color index gradually increased from $+2^m.2$ to $+3^m.6$ by the minimum and then decreased by $0^m.7$ on the ascending branch until the brightness rose to $V = 13^m$.

During the shallow minimum in 2000, $V-I$ slightly increased from $+2^m4$ to $+2^m6$ by the minimum brightness and returned to its original value of $+2^m4$ after the emergence from the minimum.

Thus, the $V-I$ color amplitude correlates closely with the V brightness amplitude. During deep fadings, the color index increases by more than 1^m, while during shallow fadings, it increases only by a few tenths of a magnitude. After the brightness of the star returned from its minima, with the exception of 2002, the mean $V-I$ color index was with the range $+2^m2 - +2^m6$.

The color behavior of FG Sge will be qualitatively interpreted below.

It should be noted that in the ten years of the star's stay in the R CrB phase, the depth of its optical minima tended to increase; in recent years, the star has not regained its normal brightness. This behavior showed up particularly clearly in 2002, which may be indicative of a further increase in the stellar-wind intensity with time.

THE DUST SHELL OF FG Sge IN THE R CrB PHASE

As was shown by many authors (Woodward *et al.* 1993; Tatarnikov *et al.* 1998; Taranova and Shenavrin 2002), all features of the star's photometric behavior in the new phase that began in 1992 are attributable to the dust clouds that condense in the matter ejected by the star. The star now has a probably spherical dust shell that formed in 1992 and is clearly seen in the LM bands. The LM photometry suggests (Taranova and Shenavrin 2002) that the radiation in these bands responded only slightly to the dramatic optical brightness variations in 1999−2002. The temperature of the dust shell was estimated by the above authors to be about 750 K, and its mass is variable both because of its expansion and dispersal and because of its replenishment with newly forming dust.

The optical events that we consider here are associated mainly with the formation of new dust clouds along the line of sight. The dust grains are most likely composed of carbon, because the spectroscopic observations suggest that a large amount of carbon is dredged up from the star's deep layers into its atmosphere (Kipper *et al.* 1995). The presence of strong Swan bands in the spectrum of FG Sge, which are in absorption in a bright state and in emission when the stellar photosphere is obscured by a dust cloud, is also indicative of a high carbon abundance in the extended gaseous envelope (Arkhipova *et al.* 1999). In addition, a double CO source associated with FG Sge has been observed (Hinkle *et al.* 1995).

The significant decrease in $B-V$ on the descending branch of blue minima most likely results from the scattering of light by a dust cloud along the observer's line of sight. Strong scattering in the direction of the incident beam and a significant decrease in $B-V$ compared to the color index of the incident light are known to have been observed at small angles of incidence of the light on interstellar dust grains. The blueness decreases with increasing angle of incidence, and the color index of the scattering cloud can be larger than that of the star at large angles of incidence. It is highly likely that the deepest and always blue photometric minima of FG Sge are attributable to the dense dust clouds that were ejected exactly toward the observer, and the color index increases as they move tangentially. When the cloud becomes transparent, as long as the extinction in it is substantial ($\Delta A_V \geq 3^m$), an additional color excess $\Delta(B-V)$ appears; this excess characterizes the absorbing properties of the cloud, in particular, $R_V = \Delta A_V/\Delta(B-V)$. As the brightness rises, this color excess decreases, and the $B-V$ color index approaches its normal (after 1992) value of about $+2^m0$.

Thus, the $B-V$ color index during deep photometric minima is strongly affected by both the scattering and the absorption of light by the particles of which the dust cloud consists.

During the ejections of the clouds that obscure a small part of the stellar disk (a shallow minimum), the fraction of scattered radiation is small, and the $B-V$ color index changes only slightly.

The completely different behavior of $V-I$ compared to $B-V$ is most likely related to the absorbing and emitting properties of the dust cloud. The newly forming dust clouds have a temperature that appreciably exceeds the temperature of the farther dust shell. It can be estimated by using near-infrared two-color diagrams, for example, $I-J$ and $J-H$. Using the observations in the I band from Table 2 of this paper (which are either simultaneous or close in time) and those in the JH bands of Taranova and Shenavrin (2002), and taking the temperature of a G2 I star for that of FG Sge, we estimated the temperature of the newly forming dust clouds to be 1000−1200 K.

Thus, the newly forming dust clouds primarily show up as absorbing and scattering ones in the BV bands and as absorbing and emitting ones at wavelengths of about 1 μm or longer; as the wavelength increases, the absorption amplitude greatly decreases, while the contribution from the radiation of dust clouds is generally small. Since the situation in the R band is particularly complex, we restricted ourselves to describing the behavior of the $V-R$ color index.
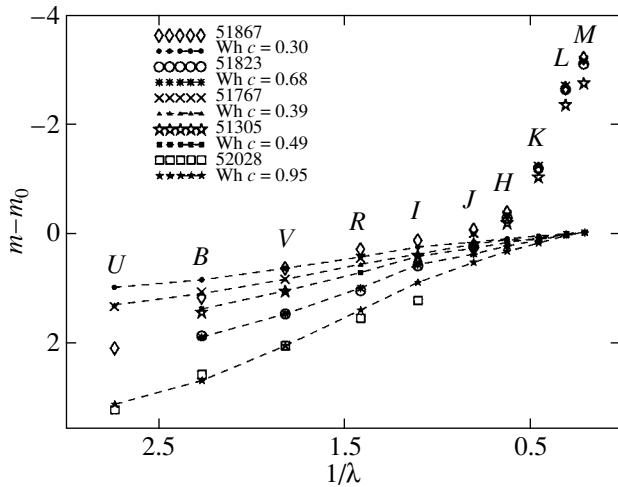
Fig. 4. Wavelength dependence of extinction in the dust shell of FG Sge.

To get an idea of the wavelength dependence of extinction in the circumstellar dust shell, we chose epochs in the light curve of the star outside those of eclipses and compared the observed U, B, V, R, I magnitudes with the observations of FG Sge in 1986. At the same time, we assumed that the stellar temperature was constant after 1986, as confirmed by the spectroscopic observations (Kipper *et al.* 1995). For the epoch JD 2446618 (July 6, 1986), Arkhipova and Taranova (1990) gave the following magnitudes:

$$B = 10\overset{m}{.}88, \quad V = 9\overset{m}{.}09, \quad J = 6\overset{m}{.}93,$$
$$H = 6\overset{m}{.}53, \quad K = 6\overset{m}{.}49, \quad L = 6\overset{m}{.}27,$$
$$M = 6\overset{m}{.}26.$$

For the same date, the U magnitude corrected for the contribution from the companion and the nebula is $U = 12\overset{m}{.}23$. These magnitudes characterize the mean brightness of FG Sge in the pulsation cycle, before the onset of the R CrB phase.

The magnitude differences between the chosen epoch of observations after 1992 and the above epoch are presented in Fig. 4. They give the amplitude of the fading in each of the optical bands caused by extinction in the circumstellar dust shell. At $\lambda > 1\,\mu$m, the dust radiation is substantial, and an infrared excess increasing with wavelength is observed. The infrared photometric data were taken from Tatarnikov *et al.* (1998) and Taranova and Shenavrin (2002). Figure 4 also shows the wavelength dependence of extinction for the standard reddening law (Whitford 1958) normalized to the observed extinction in V. We see that for the star's bright states after its emergence from the minimum or at the beginning of the descent (JD 2451305, 2451767, 2452029), the extinction in the dust shell in $UBVRI$ is satisfactorily

represented by the standard law at various extinction constants $c = \log[I_0(H_\beta)/I(H_\beta)]$: from $c = 0.4$ to $c = 0.95$. The epoch JD 2451823 in Fig. 4 is the epoch of a red shallow minimum ($c = 0.68$), and it is important to emphasize that no deviations from Whitford's reddening law are observed in this case. The date JD 2451867, for which the wavelength dependence of extinction in the circumstellar shell is much steeper than the standard law $A_\lambda \sim \lambda^{-1}$ and can be fitted as $A_\lambda \sim \lambda^{-3}$ in the $UBVRI$ bands, constitutes an important exception. This epoch in the light curve corresponds to the emergence of the star from the shallow minimum mentioned above, the ascending branch of which exhibited a systematic increase in $B-V$ that continued to grow.

The circumstellar dust shell is replenished through the expansion and dispersal of the dust clouds that cause deep fadings. Clearly, it consists of the same particles as the clouds, which are similar to the interstellar particles responsible for the optical extinction, judging from Fig. 4. In this case, there is no need to assume the presence of small particles to explain the star's bluing on the descent to its minima, and the hypothesis of light scattering by particles on the line of sight is further justified. However, as we see from the data at JD 2451867, the situation even outside periods of eclipses can be more complex, and other hypotheses should be invoked to interpret the wavelength dependence of optical and near-infrared (up to $1\,\mu$m) extinction.

SPECTROSCOPIC OBSERVATIONS OF FG Sge IN 1999−2002

The dramatic brightness variations of FG Sge after it entered the R CrB phase are also accompanied by significant changes in its spectrum. In contrast to the photometric observations, spectroscopic observations have been carried out by many researchers (Stone *et al.* 1993; Kipper *et al.* 1995; Iijima 1996; Gonzalez *et al.* 1998; Kipper and Klochkova 1999, 2001). We also follow the spectroscopic behavior of FG Sge (Arkhipova and Esipov 1996; Arkhipova *et al.* 1998, 1999). In 1999−2002, we continued to observe the star at the Cassegrain focus of the 125-cm reflector at the Crimean Station of the SAI with a fast spectrograph equipped with an ST-6I CCD camera. With a 600 line/mm grating, the spectral resolution was ~5.5 Å per pixel. We obtained a total of 13 spectrograms in the range $\lambda\lambda 4200-7500$ Å, which was covered by two frames with a small mutual overlap, and one spectrogram in the range $\lambda\lambda 4500-6400$ Å. Table 3 gives a log of observations together with our V magnitudes of the star at the corresponding date and a brief description

Table 3. A log of spectroscopic observations for FG Sge in 1999−2002

Date	Range, Å	V	Spectral features
May 14, 1999	4200−7500	10^m14	C_2 bands and Na I lines in absorption
June 17, 1999	4200−7500	10.46	Na I lines in absorption, strengthening of C_2 absorption bands
Aug. 9, 1999	4200−7500	10.71	Na I lines in absorption, further strengthening of C_2 absorption
Sep. 17, 1999	4200−7500	11.64	Na I lines in absorption, weak C_2 absorptions; nebular lines are seen
Sep. 20, 1999	4200−7500	12.20	C_2 bands and Na I lines in emission; nebular lines
Nov. 5, 1999	4500−6400	15.31	C_2 bands and Na I lines in emission; nebular lines
May 13, 2000	4200−7500	10.50	C_2 bands and Na I lines in absorption
Sep. 1, 2000	4200−7500	10.06	C_2 bands and Na I lines in absorption
Sep. 27, 2000	4200−7500	10.53	C_2 bands and Na I lines in absorption
Oct. 24, 2000	4200−7500	10.25	C_2 bands and Na I lines in absorption
May 16, 2001	4200−7500	12.66	Na I lines in emission, C_2 bands in absorption; nebular lines
May 18, 2001	4200−7500	13.13	Na I lines in emission, C_2 bands in absorption; nebular lines
May 6, 2002	4200−7500	13.20	Na I lines in emission, C_2 bands in absorption; nebular lines
May 15, 2002	4200−6000	13.20	Na I lines in emission, C_2 bands in absorption; nebular lines

of spectral features. Because of the low spectral resolution, we restricted our analysis to broad features— the Swan C_2 bands and the Na I doublet ($\lambda\lambda5890-5896$ Å). Table 4 presents the Na I D equivalent widths and the indices that characterize the depths of the C_2 $\lambda4737$ Å

$$C_2 = 1.0-2.0I(4700)/[I(4600) + I(4800)]$$
$$\text{(Iijima 1996)}$$

and $\lambda5635$ Å bands:

$$C_2 \text{ index} = -2.5\log(F_\nu(5610)/F_\nu(5710))$$
$$\text{(Fay } et\ al.\ 1974).$$

Apart from the 1999−2002 observations, Table 4 presents the 1998 observations, which we qualitatively described previously (Arkhipova *et al.* 1999). The errors in the Na I D equivalent widths and the C_2 indices were ∼10% and ±0.05, respectively. Figure 5 shows the V light curve for FG Sge and data from Table 4.

In 1999, we obtained six spectrograms; three of these indicate a high brightness, two were taken when the star descended to a deep minimum, and one was taken at minimum brightness. The 1999 spectroscopic observations of FG Sge began in May, when the star was bright. The May 14 spectrum exhibits shallow Swan C_2 $\lambda4737$, 5165, 5635, 6191 Å bands and the Na I D absorption line. The most dramatic event of 1999, the fading of the star by 5^m,

was preceded by a shallow photometric minimum (JD(min) = 2451387 ± 5). The June 17 spectrogram (JD 2451347) refers to the descent of FG Sge to this minimum. The Swan bands at this time were deeper than those observed on May 14. The spectroscopic observations on August 9 (JD 2451400), when the star had just emerged from the shallow minimum, showed a further strengthening of the Swan bands. Figure 6 shows the variations in the depth of the Swan bands at the shallow minimum of 1999.

The next two spectrograms taken on close dates, September 17 and 20, 1999, refer to the descent of the star to a deep minimum. On September 17, the star, at a magnitude $V = 11^m6$, had weak Swan absorption bands and the Na I D absorption line in its spectrum. Its spectrum exhibited lines of the planetary nebula. Three days later, the star faded by 0^m5, and the Swan bands and the Na I D line were in emission. Thus, a self-reversal occurred in the Swan bands and the Na I D lines between September 17 and 20 at a V magnitude of 12^m. The next spectrum was taken on November 5, 1999, at a deep photometric minimum for FG Sge. The strong Na I D emission line was the most prominent feature in the $\lambda4500-6400$ Å spectrum. The Swan bands continued to be in emission. For comparison, Fig. 7 shows the star's normalized spectra in May and November 1999 near the sodium doublet.

In 2000, FG Sge returned from its deep photometric minimum of 1999 and then slightly faded by 1^m

Table 4. Na I D line equivalent widths and C_2 indices

Date	W(Na I), A	C_2	C_2 index
Apr. 2, 1998	−5.7	0.50	0.44
May 24, 1998	6.3	−	−
May 25, 1998	37.3	−0.30	−
May 29, 1998	50.7	−0.26	−0.22
May 31, 1998	61.7	−0.45	−0.35
June 22, 1998	225	−	−
Sep. 17, 1998	180	−0.01	−
Sep. 18, 1998	228	0.28	0.33
Sep. 21, 1998	160	0.24	0.33
Sep. 24, 1998	129	0.15	0.46
Sep. 25, 1998	114	0.31	0.39
Oct. 18, 1998	54	0.38	0.55
May 14, 1999	−6.8	0.19	0.13
June 17, 1999	−4.3	0.36	0.26
Aug. 9, 1999	−8.6	0.59	0.58
Sep. 17, 1999	−5.6	0.11	0.11
Sep. 20, 1999	2.7	−0.06	−0.05
Nov. 5, 1999	196	−0.30	−0.09
May 13, 2000	−5.9	0.17	0.26
Sep. 1, 2000	−7.0	0.43	0.56
Sep. 27, 2000	−6.0	0.63	0.73
Oct. 24, 2000	−8.0	0.55	0.52
May 16, 2001	1.9	0.73	0.85
May 18, 2001	2.7:	0.69	0.70
May 6, 2002	3.0	0.44	0.54
May 15, 2002	3.8	0.46	0.61

in V. The first 2000 spectrum that we took on May 13 relates to the time the dust cloud responsible for the deep minimum of 1999 dispersed and the spectrum had the appearance characteristic of the bright state of FG Sge. In late June and July 2000, Kipper and Klochkova (2001) obtained high-resolution spectra of FG Sge. The authors noted that these spectra did not differ significantly from the spectra that the star had before its brightness decline in 1992 and at its photometric maximum in 1997. Our next three spectra, taken on September 1, September 27, and October 24, 2000, showed variations in the depths of the Swan bands with brightness. The depths of the Swan bands were at a maximum when the brightness of FG Sge was at a minimum. The spectroscopic observations confirm our conclusion drawn from the photometric observations that the shallow minimum of 2000 was a dust one. This is suggested by the strengthening of the Swan bands, due to an increase in the abundance of molecular carbon in the extended expanding stellar envelope and the subsequent dust condensation.

In 2001, we carried out spectroscopic observations of FG Sge on May 16 and 18 on the descent to a deep minimum, when the star already faded by more than 3^m in V. In contrast to 1999, when a self-reversal occurred in the Swan bands at a V magnitude of 12^m, in 2001, the Swan bands at a fainter magnitude were still in absorption and very deep, while the Na I D line was already in emission.

The spectroscopic observations of FG Sge in 2002 relate to the time the star emerged from a deep minimum and, having reached a V magnitude of 13^m, was just about to descent to the next deep minimum. The May 6 and 15 observations showed that the Swan bands were enhanced, compared to the star's normal (bright) state.

The spectroscopic observations of FG Sge in 1999 indicated that, as during the deep minima of 1992 (Arkhipova and Esipov 1996), 1994 (Gonzalez *et al.* 1998), 1996 (Gonzalez *et al.* 1998; Arkhipova *et al.* 1998), and 1998 (Arkhipova *et al.* 1999), during the descent of the star to a deep minimum, the Swan C_2 absorption bands and the Na I D lines initially weakened, and a self-reversal subsequently occurred in these lines. The deep photometric minima of 1999 and 2001 were preceded by fadings of less than 1^m in V. We were able to trace the development of the spectra at these shallow minima. There is a clear correlation of the C_2 indices with brightness: the Swan absorption bands become deeper with declining brightness. The reason is that the abundance of molecular carbon in the extended envelope of FG Sge increases during the stellar-wind enhancement and the subsequent condensation of dust clouds that are also responsible for the
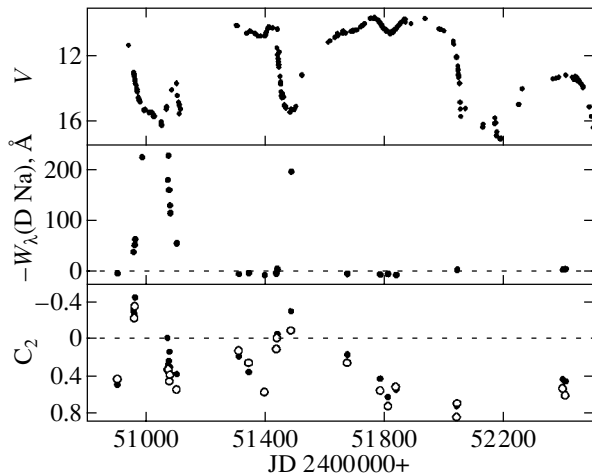
Fig. 5. The V light curve for FG Sge and data from Table 4. In the lower panel, the open and filled circles denote C_2 and C_2 index, respectively.
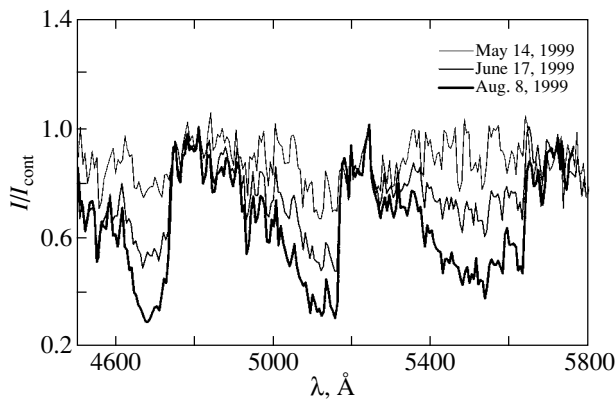

Fig. 6. Variations in the depths of the Swan bands in the May 14, June 17, and August 9, 1999 spectra.
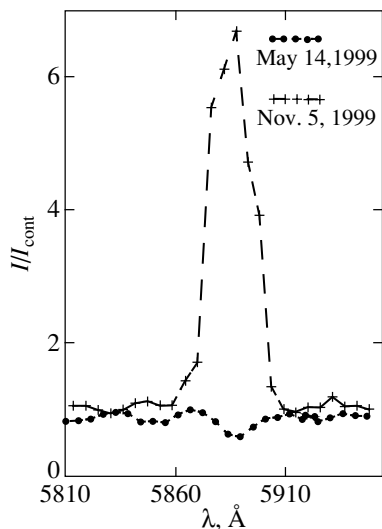

Fig. 7. The spectra of FG Sge near the Na I D doublet on May 14 and November 5, 1999.

shallow minima. The 1999−2002 observations also indicated a strengthening of the Swan bands with time—an increase in the maximum C_2 indices. Thus, Iijima (1996) give a maximum value of $C_2 = 0.4 \pm 0.05$ for 1992−1994, and Arkhipova *et al.* (1998) give C_2 index $= 0.38$ for 1996−1997. According to our most recent observations, the C_2 index has already reached 0.73 ± 0.05.

CONCLUSIONS

In 1999−2002, the photometric activity of FG Sge, which resembles the behavior of R CrB stars, continued. We carried out four-color observations of three deep fadings. During all of these fadings, the $B - V$ color index significantly decreased with declining brightness, as in 1992−1998. These decreases most likely resulted from the scattering of stellar light by particles of a dust cloud along the line of sight. In contrast to them, the fraction of scattered light during shallower fadings is probably small, and only the absorption of light in the cloud is substantial. At longer wavelengths (in R and particularly in I), the fraction of scattered light is smaller than that in B and V.

For the epochs of maximum brightness (outside eclipses by dust clouds), we constructed the wavelength dependence of circumstellar extinction in the bands from U to I. In general, it differs only slightly from the standard interstellar reddening law, suggesting that the dust grains in the circumstellar dust shell of FG Sge and in the interstellar medium are similar.

The low-resolution spectroscopic observations performed in 1999−2002 confirmed the reversal of the spectrum of the extended gaseous stellar envelope—the Swan bands and the Na I D doublet—on the descent of the star to deep minima. At the same time, we found a close correlation between the depths of the Swan bands and the brightness phase during shallow fadings. The depths of the Swan bands in the star's bright state were found to increase with time, which is attributable to the growth of the gas−dust circumstellar shell around FG Sge as increasingly powerful dust ejections are repeated.

ACKNOWLEDGMENTS

REFERENCES

1. V. P. Arkhipova, Perem. Zvezdy **21**, 617 (1982).
2. V. P. Arkhipova, Perem. Zvezdy **22**, 631 (1988).
3. V. P. Arkhipova, Pis'ma Astron. Zh. **19**, 593 (1993) [Astron. Lett. **19**, 235 (1993)].
4. V. P. Arkhipova, Pis'ma Astron. Zh. **20**, 919 (1994) [Astron. Lett. **20**, 804 (1994)].
5. V. P. Arkhipova, Pis'ma Astron. Zh. **22**, 828 (1996) [Astron. Lett. **22**, 743 (1996)].
6. V. P. Arkhipova and V. F. Esipov, Pis'ma Astron. Zh. **22**, 264 (1996) [Astron. Lett. **22**, 235 (1996)].
7. V. P. Arkhipova and O. G. Taranova, Pis'ma Astron. Zh. **16**, 808 (1990) [Sov. Astron. Lett. **16**, 347 (1990)].
8. V. P. Arkhipova, V. F. Esipov, and G. V. Sokol, Pis'ma Astron. Zh. **24**, 431 (1998) [Astron. Lett. **24**, 365 (1998)].
9. V. P. Arkhipova, V. F. Esipov, G. V. Sokol, and S. Yu. Shugarov, Pis'ma Astron. Zh. **25**, 849 (1999) [Astron. Lett. **25**, 739 (1999))].
10. T. Bloecker, Astron. Astrophys. **299**, 755 (1995).
11. T. Bloecker and D. Schoenberner, Astron. Astrophys. **324**, 991 (1997).
12. T. D. Fay, W. H. Warren, H. R. Johnson, and R. K. Honeycutt, Astron. J. **79**, 634 (1974).
13. F. Herwig, T. Bloecker, D. Schoenberner, and M. El Eid, Astron. Astrophys. **324**, L81 (1997).
14. K. H. Hinkle, R. R. Joyce, and V. Smith, Astron. J. **109**, 808 (1995).
15. G. Gonzalez, D. L. Lambert, G. Wallerstein, *et al.*, Astrophys. J., Suppl. Ser. **114**, 133 (1998).
16. I. Iben, Astrophys. J. **277**, 333 (1984).
17. T. Iijima, Mon. Not. R. Astron. Soc. **283**, 141 (1996).
18. T. Kipper and V. Klochkova, Inf. Bull. Var. Stars, No. 4661 (1999).
19. T. Kipper and V. Klochkova, Baltic Astron. **10**, 393 (2001).
20. T. Kipper, M. Kipper, and V. Klochkova, Astron. Astrophys. **297**, L33 (1995).
21. T. M. Lawlor and J. MacDonald, Astrophys. J. **583**, 913 (2003).
22. D. Schoenberner, Astrophys. J. **272**, 708 (1983).
23. R. P. S. Stone, R. P. Kraft, and C. F. Prosser, Publ. Astron. Soc. Pac. **105**, 755 (1993).
24. O. G. Taranova and V. I. Shenavrin, Astron. Zh. **79**, 1118 (2002) [Astron. Rep. **46**, 1010 (2002)].
25. A. V. Tatarnikov, V. I. Shenavrin, and B. F. Yudin, Astron. Zh. **75**, 428 (1998) [Astron. Rep. **42**, 377 (1998)].
26. A. E. Whitford, Astron. J. **63**, 201 (1958).
27. C. E. Woodward, G. F. Lawrence, R. D. Gehrz, *et al.*, Astrophys. J. **408**, 37 (1993).

Translated by V. Astakhov

The Hydrogen Emission Spectrum of a Shock Wave in a Stellar Atmosphere

Yu. A. Fadeyev[*]

Institute of Astronomy, Russian Academy of Sciences, Pyatnitskaya ul. 48, Moscow, 109017 Russia
Received June 19, 2003

Abstract—Based on a self-consistent solution of the equations of gas dynamics, kinetics of hydrogen atomic level populations, and radiative transfer, we analyze the structure of a shock wave that propagates in a partially ionized hydrogen gas. We consider the radiative transfer at the frequencies of spectral lines by taking into account the effects of a moving medium in the observer's frame of reference. The flux in Balmer lines is shown to be formed behind the shock discontinuity at the initial hydrogen recombination stage. The Doppler shift of the emission-line profile is approximately one and a half times smaller than the gas flow velocity in the Balmer emission region, because the radiation field of the shock wave is anisotropic. At Mach numbers $M_1 \lesssim 10$ and unperturbed gas densities $\rho_1 = 10^{-10}$ g cm^{-3}, the Doppler shift is approximately one third of the shock velocity U_1. The FWHM of the emission-line profile $\delta\varphi$ is related to the shock velocity by $\delta\varphi \approx k_\varphi U_1$, where $k_\varphi = 1$, 0.6, and 0.65 for the Hα, Hβ, and Hγ lines, respectively. © *2003 MAIK "Nauka/Interperiodica"*.

Key words: *plasma astrophysics, hydrodynamics and shocks, stellar atmospheres, radiative transfer.*

INTRODUCTION

The spectra of radially pulsating late-type stars near maximum light show intense hydrogen emission lines, and many metal absorption lines split into two components with a radial-velocity difference of several tens of km s^{-1}. These spectral features are attributable to the propagation in the stellar atmosphere of the shock wave that arises in each oscillation cycle at the photospheric level at the time of the fastest expansion of the outer layers in a pulsating star. Split absorption lines are indicative of an abrupt change in the gas flow velocity in the stellar atmosphere, and the appearance of hydrogen emission lines is attributed to the radiative cooling of the gas behind the shock discontinuity (Kraft *et al.* 1959; Wallerstein 1959; Abt 1959; Abt and Hardy 1960; Gorbatskiĭ 1961).

A large amount of observational data on the emission lines in the spectra of pulsating stars has been obtained to date. However, the absence of a detailed self-consistent model for a radiative shock wave significantly narrows the possibilities for spectroscopy in diagnosing the state of the gas in a shock wave. Fadeyev and Gillet (1998) suggested a method for calculating the shock structure based on a self-consistent solution of the equations of gas dynamics, atomic kinetics, and radiative transfer.

The potentialities of this method, as applied to shock waves propagating in a partially ionized hydrogen gas with the temperature and density typical of stellar atmospheres, were demonstrated in several subsequent papers (Fadeyev and Gillet 2000, 2001; Fadeyev 2001; Fadeyev *et al.* 2002). Unfortunately, since in all these papers the radiative transfer was considered in the approximation of a stationary medium, the theoretically calculated emission-line profiles could not be compared with the results of observations. In this paper, we present the results of our calculations of the shock structure by taking into account the effects of a moving medium in the solution of the radiative transfer equation in hydrogen spectral lines.

THE SHOCK MODEL

As in our previous papers (Fadeyev and Gillet 1998, 2000, 2001; Fadeyev 2001; Fadeyev *et al.* 2002), below we consider the structure of a stationary plane-parallel shock wave propagating in a homogeneous medium. The applicability of the assumed stationarity and plane geometry to the conditions of stellar atmospheres follows from the fact that the shock length ($\sim 10^5$ cm) is small compared to the dynamic scale height of a pulsating supergiant ($H_{\rm p, dyn} \gtrsim 10^{11}$ cm). In the approximation of a steady-state gas flow and a plane geometry, the continuity equation reduces to the relation $\rho U = \dot{m} \equiv$ const between the gas

[*]E-mail: `fadeyev@inasan.rssi.ru`

density ρ and flow velocity U, while the equations of motion and energy conservation, together with the equations of atomic-level population kinetics, form a system of ordinary differential equations. The obvious advantages of this approach stem from the fact that the efficient methods for solving "stiff" problems, to which the equations of atomic kinetics belong, were best developed for ordinary differential equations (Hall and Watt 1976; Radhakrishnan and Hindmarsh 1993). The equations used to calculate the structure of a radiative shock wave were described in detail by Fadeyev and Gillet (2000).

We model the shock wave by a plane-parallel layer that moves together with the shock, with a velocity U_1, relative to an unperturbed gas with a density ρ_1 and temperature T_1. The coordinate origin coincides with the infinitely thin layer where the gas-dynamic variables undergo a discontinuity. The spatial coordinate X is reckoned along the trajectory of the gas particles that move through the shock. The unperturbed gas flows into the front boundary of the slab with coordinate X_1, and the coordinate X_N of the rear boundary of the slab is determined during the calculations in such a way that the thermodynamic state of the outflowing gas (in particular, the electron temperature T_e and the degree of ionization x_H) are as close as possible to the unperturbed state.

We determined the monochromatic parameters of the shock-generated radiation field for given spatial distributions of the optical depth $\tau_\nu(X)$ and the source function $S_\nu(X)$ by solving the two-point boundary-value problem for the entire shock using the modified Feautrier method suggested by Rybicki and Hummer (1991). The quantities $\tau_\nu(X)$ and $S_\nu(X)$ are the solutions of the initial-value problem for the equations of motion, energy conservation, and atomic-level populations. These equations are integrated in the segment $[X_1, X_N]$, with the solution being interrupted at the shock discontinuity, where the Rankine–Hugoniot relations are used. We take into account the relationship between the gas flow and the radiation field by using an iterative procedure that includes the integration of the system of differential equations, followed by the solution of the transfer equation for the entire shock. The convergence of the iterative process was demonstrated by Fadeyev and Gillet (1998, 2000).

When solving the radiative transfer equation, we approximate the shock wave by a discrete model on a spatial grid X_j $(1 \leq j \leq N)$ with $N = 2000$ points. The sizes $\Delta X_{j-1/2} = X_j - X_{j-1}$ of the spatial intervals increase in geometric progression in both directions from the point of shock discontinuity $X_{\mathcal{J}} = 0$. The frequency range $13.5 \leq \log \nu \leq 16$, within which we solve the transfer equation, is represented by a set of intervals. The boundaries of these intervals are either the threshold frequency of ionization from the ith level of a hydrogen atom or the boundary of the adjacent frequency interval of a spectral line with a half-width $\Delta \nu = 5 \times 10^{-4} \nu_0$, where ν_0 is the frequency of the line center in the comoving reference frame. We used eight grid points of the Gaussian quadrature formula in the continuum frequency intervals and up to 300 grid points for the spectral-line frequency intervals. The angular moments of the transfer equation were calculated by using eight grid points for the continuum and 32 grid points for spectral lines. A large number of quadrature grid points in the angular variable are required, because the radiation field in spectral lines is highly anisotropic.

The model hydrogen atom is represented by $L = 5$ levels and an ionization state. We used the cross sections calculated by Scholz *et al.* (1990), Aggarwal *et al.* (1991), and Callaway (1994) to calculate the electron-impact excitation rates and calculated the collisional ionization rates, by using the approximation polynomials derived by Lennon *et al.* (1986). We calculated the radiative bound–bound transition rates for lines with Doppler profiles.

Figure 1 illustrates the structure of a radiative shock wave, i.e., the variation of gas-dynamic variables with spatial coordinate X. For a better visualization, we use the logarithmic scale along the X axis. Therefore, the spatial dependence of each variable is represented by two plots: the left-hand plot for the preshock region of space $(X < 0)$ and the right-hand plot for the postshock region of space $(X > 0)$. The temperature of the hydrogen atoms behind the shock discontinuity T_a^+ can be determined by solving the Rankine–Hugoniot equations (formula (5) in the paper of Fadeyev and Gillet (2001)), while for the electron gas, we use the approximation of adiabatic compression: $T_e^+ = (\rho^+/\rho^-)^{\gamma-1} T_e^-$, where $\gamma = \frac{5}{3}$ is the adiabatic index for the electron gas and the minus and plus superscripts denote the variables at the points $X_{\mathcal{J}-1/2}$ and $X_{\mathcal{J}+1/2}$ that are closest to the shock discontinuity. The electron (T_e) and atomic (T_a) temperatures behind the shock discontinuity are equalized by the elastic collisions between electrons and hydrogen ions. At hydrogen ionization degrees $x_H > 10^{-2}$, the efficiency of energy transfer from neutral hydrogen atoms to electrons is negligible because of the low density of neutral atoms and the small cross section of this process.

The extent of the shock wave in a partially ionized hydrogen gas can be estimated from the dependence of ionization degree x_H on spatial coordinate X. In front of the shock discontinuity, the actual shock boundary coincides with the ionization region associated with the absorption of Lyman continuum

emission (the radiative-precursor region); behind the discontinuity, the shock boundary is determined by the region of the hydrogen atomic recombination as the slowest relaxation process.

The radiative heating and cooling of a gas are described by the divergence of the radiation flux

$$\nabla \cdot F_R = 4\pi \int_0^\infty (\eta_\nu - \kappa_\nu J_\nu) d\nu, \qquad (1)$$

where η_ν and κ_ν are the monochromatic emission and absorption coefficients, and J_ν is the mean intensity of radiation at frequency ν. The significant variations in the divergence of the radiation flux in the region -10^2 cm $\lesssim X \lesssim 10^2$ cm are attributable to variations in the populations of atomic levels $i \geq 2$ near the shock discontinuity. However, these variations have no appreciable effect on the total radiation flux, because the extent of this region is small. The discontinuity of $\frac{1}{\rho}\nabla \cdot F_R$ at point $X_{\mathcal{J}} = 0$ results from the significant broadening of the Doppler line profiles due to an abrupt increase in the atomic temperature T_a at the shock discontinuity.

Figure 1e shows plots of the total radiation flux F_R and the Lyman continuum flux F_{Ly}. Within the bulk of the shock wave, the radiation flux is directed oppositely to the gas flow ($F_R < 0$). The radiation originates in the $F_R = 0$ layer behind the shock discontinuity in the atomic hydrogen recombination region. The radiation fluxes emerging from the front and rear boundaries of the shock model are approximately (to within several percent) equal: $-F_{R1} \approx F_{RN}$.

RADIATIVE TRANSFER IN SPECTRAL LINES

In the atmospheres of pulsating stars, the ratio of the gas flow velocity to the speed of light is $U/c \lesssim 3 \times 10^{-4}$. Therefore, a clear manifestation of a moving medium is the Doppler effect in spectral lines, since the Doppler shift is comparable to the line width. To within the first order of smallness in U/c and in the approximation of a plane geometry, the radiative transfer equation in a comoving reference frame is

$$\mu \frac{\partial I_{\nu\mu}}{\partial X} - \mu^2 \frac{\nu}{c}\frac{dU}{dX}\frac{\partial I_{\nu\mu}}{\partial \nu} = \eta_\nu - \chi_\nu I_{\nu\mu}, \qquad (2)$$

where χ_ν is the total absorption coefficient, $I_{\nu\mu}$ is the specific radiation intensity, $\mu = \cos\theta$, and θ is the angle between the propagation direction of the radiation and the X axis. For brevity, we omit the designations of the functional dependence on spatial coordinate X in Eq. (2).

To solve equations of the form (2), Mihalas *et al.* (1975) suggested a method based on analysis
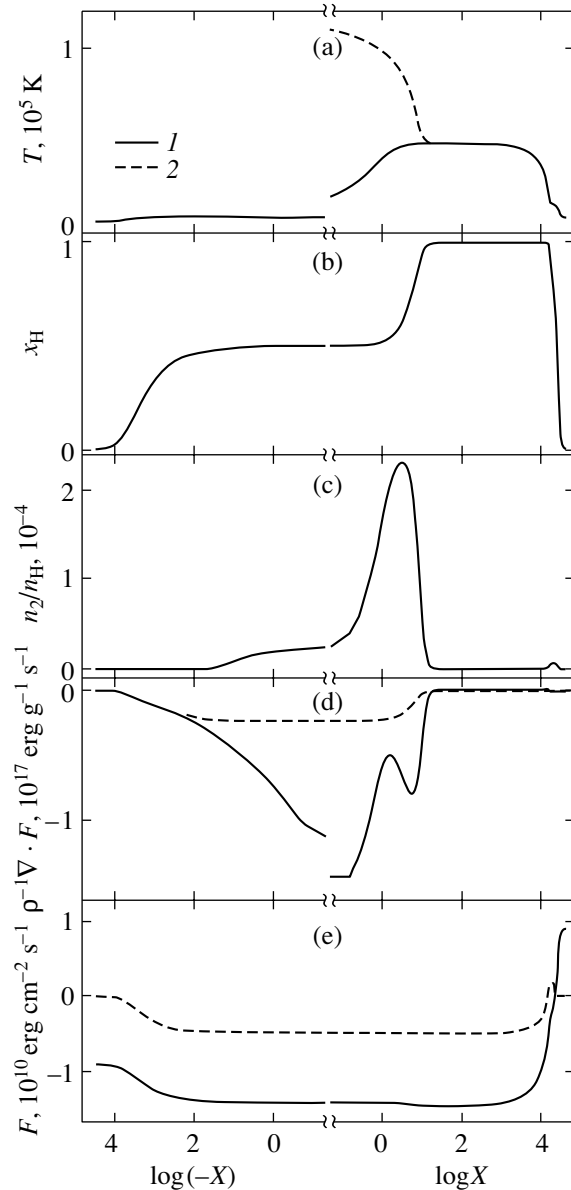
Fig. 1. The shock model with $T_1 = 6000$ K, $\rho_1 = 10^{-10}$ g cm^{-3}, and $U_1 = 70$ km s^{-1}: (a) electron temperature T_e (*1*) and atomic temperature T_a (*2*); (b) hydrogen ionization degree x_H; (c) second-level population n_2, in units of hydrogen atomic density n_H; (d) divergence of the total radiation flux (*1*) and divergence of the radiation flux in the Lyman continuum (*2*); (e) total radiation flux (*1*) and radiation flux in the Lyman continuum (*2*).

of the boundary-value problem for the spatial variable X and the initial-value problem for the radiation frequency ν. The advantages of this approach were clearly demonstrated in numerous papers devoted to radiative transfer in a medium with a monotonically changing gas flow velocity (e.g., in expanding stellar atmospheres). Unfortunately, this method loses its advantages when applied to radiative transfer in a medium with a nonmonotonic velocity field, because
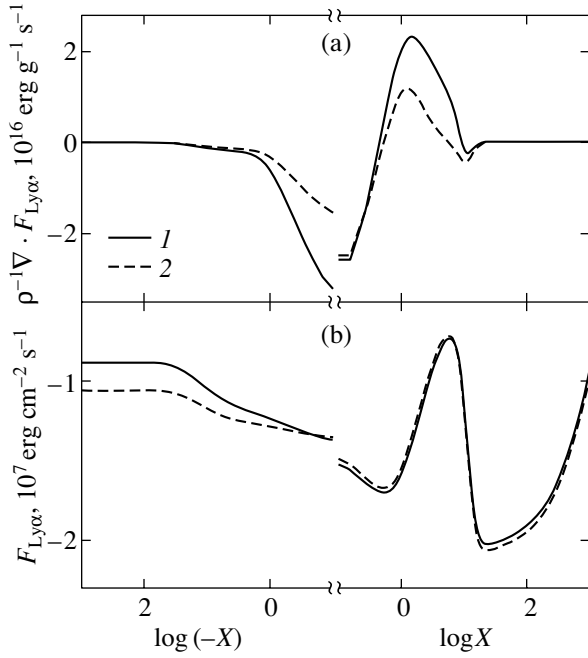
Fig. 2. The shock model with $T_1 = 6000$ K, $\rho_1 = 10^{-10}$ g cm^{-3}, and $U_1 = 70$ km s^{-1}: (a) divergence of the radiation flux in the Lyα line with the Doppler shift (*1*) and for a stationary medium (*2*); (b) radiation flux in the Lyα line with the Doppler shift (*1*) and for a stationary medium (*2*).
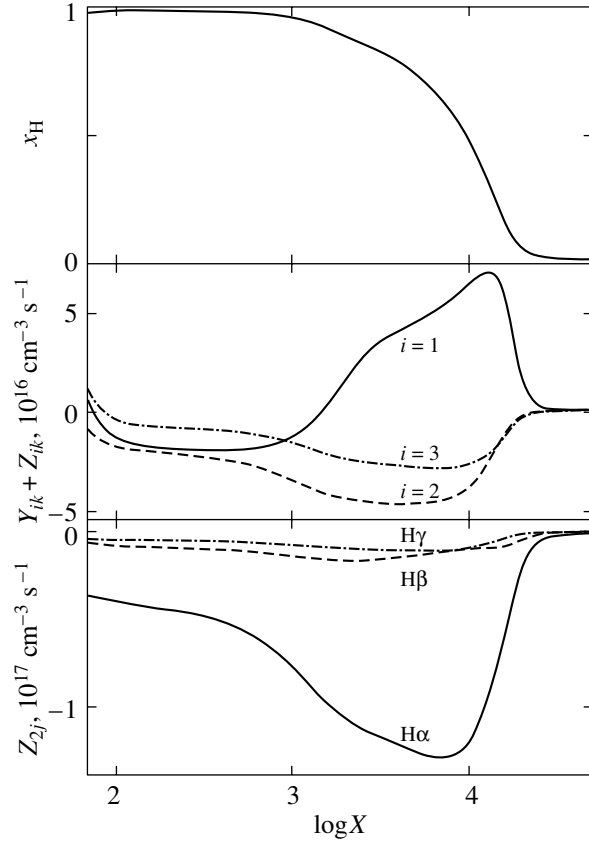

Fig. 3. Structure of the recombination zone of a radiative shock wave with $T_1 = 6000$ K, $\rho_1 = 10^{-10}$ g cm^{-3}, and $U_1 = 60$ km s^{-1}: (a) ionization degree x_H, (b) rate of ionization from the ith level, and (c) the resulting photoexcitation rate for the Hα, Hβ, and Hγ lines.

the solution becomes unstable (Mihalas 1980). Our special calculations confirmed this conclusion. As applied to a shock wave, the instability of the solution for the radiative transfer equation in a comoving reference frame turns out to be attributable to an abrupt change of the second term on the left-hand side of Eq. (2) at the shock discontinuity. For this reason, the results presented below were obtained by solving the radiative transfer equation written in the observer's reference frame.

To within terms of the first order of smallness in U/c, the transfer equation in the observer's frame has the same form as the transfer equation for a stationary medium, but with emission and absorption coefficients that depend on both the radiation frequency ν and the directional cosine μ (Mihalas 1978):

$$\mu \frac{dI_{\nu\mu}}{dX} = \eta_{\nu\mu} - \chi_{\nu\mu} I_{\nu\mu}. \qquad (3)$$

We assume that the shock wave moves toward the observer with a positive velocity U_1 and that the gas flow velocity in the observer's frame is $U_{obs} > 0$. The Doppler line profile in the approximation of a complete frequency redistribution is then given by the expression

$$\phi(\nu', \mu) = \frac{1}{\Delta\nu_D \sqrt{\pi}} \exp\left[-\frac{\nu - \nu_0(1 - \mu U_{obs}/c)}{\Delta\nu_D} \right], \qquad (4)$$

where ν' is the radiation frequency in the comoving frame,

$$\Delta\nu_D = \frac{\nu_0}{c} \left(\frac{2kT_a}{m_H} \right)^{1/2} \qquad (5)$$

is the Doppler line width on the frequency scale, and m_H is the mass of the hydrogen atom.

Since the effects of a moving medium show up most clearly at Lyα frequencies, it will suffice to consider the radiative transfer in this line to assess the role of Doppler shifts. Figure 2a shows the spatial dependences of the divergence of radiation flux

$$\nabla \cdot F_\ell = 4\pi \int\limits_{\nu_0 - \Delta\nu}^{\nu_0 + \Delta\nu} (\eta_\nu - \kappa_\nu J_\nu) d\nu \qquad (6)$$

(here, ν_0 is the frequency of the Lyα line center), calculated with allowance made for the Doppler effect and in the approximation of a stationary medium. As we see from these dependences, the Doppler shift results in stronger preshock radiative heating ($\nabla \cdot$

Parameters of the Balmer emission lines

U_1, km s^{-1}	M_1	Hα			Hβ			Hγ			U^*_{obs}, km s^{-1}
		ΔU_{obs}, km s^{-1}	$\delta\varphi$, km s^{-1}	$\log\tau_0$	ΔU_{obs}, km/s	$\delta\varphi$, km s^{-1}	$\log\tau_0$	ΔU_{obs}, km/s	$\delta\varphi$, km s^{-1}	$\log\tau_0$	
30	3.3	-9	26	-0.3	-8	26	-1.8	-7	23	-1.6	14
40	4.4	-15	40	0.3	-12	27	-0.8	-11	26	-0.9	19
50	5.5	-18	54	0.9	-17	32	-0.1	-16	30	-0.4	24
60	6.6	-20	60	1.3	-24	38	0.4	-20	34	0.0	30
70	7.7	-21	65	1.5	-23	47	0.6	-23	40	0.2	34
80	8.7	-22	71	1.7	-26	51	0.8	-26	43	0.4	38

$F_\ell < 0$ at $X < 0$) and stronger postshock radiative cooling ($\nabla \cdot F_\ell > 0$ at $X > 0$). However, the small extent of the region within which the radiation at Lyα frequencies interacts appreciably with gas makes these differences insignificant for the structure of the shock as a whole. For example, for the model shown in Fig. 2b, the Lyα fluxes calculated for stationary and moving media differ by no more than 20%, with the Lyα flux being less than $\sim 10^{-3}$ of the total flux emitted by the shock.

BALMER LINES

To describe the recombination of hydrogen atoms behind the shock discontinuity, it is convenient to use the resulting rate of ionization from the ith level

$$Y_{ik} + Z_{ik} = n_i n_e C_{ik} \left(1 - \frac{n_e}{n_i} \frac{n_i^*}{n_e^*} \right) \qquad (7)$$
$$+ n_i R_{ik} - n_e \frac{n_i^*}{n_e^*} R_{ik}^\dagger,$$

where C_{ik} is the electron impact ionization rate; R_{ik} is the photoionization rate; $(n_i^*/n_e^*)R_{ik}^\dagger$ is the rate of photorecombination to the ith level; and n_i^* and n_e^* are the density of atoms at the ith level and the electrons density, respectively, calculated using the Saha formula for the nonequilibrium electron density n_e. In Fig. 3, we clearly see from the plots of resulting ionization rate against distance from the shock discontinuity that $Y_{ik} + Z_{ik} < 0$ at $i \geq 2$; i.e., the recombination of hydrogen atoms results from electron transitions to the second or higher levels, while atoms in the ground state are ionized, which slows down the relaxation.

The contribution of individual bound−bound transitions to the formation of the radiation flux in Balmer lines can be estimated by analyzing the resulting photoexcitation rate for the transition from the lower ith level to the upper jth level:

$$Z_{ij} = n_i R_{ij} - n_j \frac{n_i^*}{n_j^*} R_{ij}^\dagger, \qquad (8)$$

where R_{ij} is the photoexcitation rate, and $(n_i^*/n_j^*)R_{ij}^\dagger$ is the rate of radiative deexcitation. As we see from Fig. 3, after the recombination to levels $i \geq 3$, electrons pass to the second level with the emission of Balmer photons. The Hα line transition has the highest intensity. The minimum of Z_{23} corresponds to the ionization degree $x_H = 0.65$ and the gas temperature $T_e = T_a \approx 1.4 \times 10^4$ K. The condition $F_\ell(H\alpha) = 0$ is also satisfied in this layer; i.e., the upstream Hα flux is equal to the downstream flux: $-F_\ell(H\alpha, \mu < 0) = F_\ell(H\alpha, \mu > 0)$. Since $Z_{12} < 0$ in the recombination region, Lyα photons are produced together with Balmer photons here.

Of greatest interest in comparing calculations with observations is the radiation flux $F_{\nu 1}$ at the front boundary of the shock model. Figure 4 shows the normalized monochromatic fluxes at the Hα, Hβ, and Hγ frequencies for shock waves with amplitudes of $U_1 = 40$, 60, and 80 km s^{-1}. For a better visualization, $F_{\nu 1}$ are shown with the opposite sign, and the negative Doppler shift corresponds to a blueshift. The dotted lines in the same figure indicate the flux profiles obtained by solving the radiative transfer equation for a stationary medium. The Doppler shifts ΔU_{obs} and the half-widths $\delta\varphi$ of the Hα, Hβ, and Hγ emission profiles are listed in the table, whose first two columns give the shock velocity U_1 and the Mach number M_1. For each of the three lines, the table gives the optical depth τ_0 of the shock model at the frequency of the line center in the absence of a Doppler shift.

As we see from Fig. 4 and the table, the widths of the emission profiles for all three lines exceed the Doppler shift. The broadest line is Hα, because an appreciable fraction of the emission in this line originates in the region of the radiative precursor. At a shock velocity $U_1 > 50$ km s^{-1}, the cooler preshock gas shows up in the Hα emission profile as a maximum with an approximately zero Doppler shift. The contribution of the radiative precursor to the emission in other Balmer lines is negligible, because the optical depth is much smaller. All of the Balmer lines are characterized by an increase in the width of the
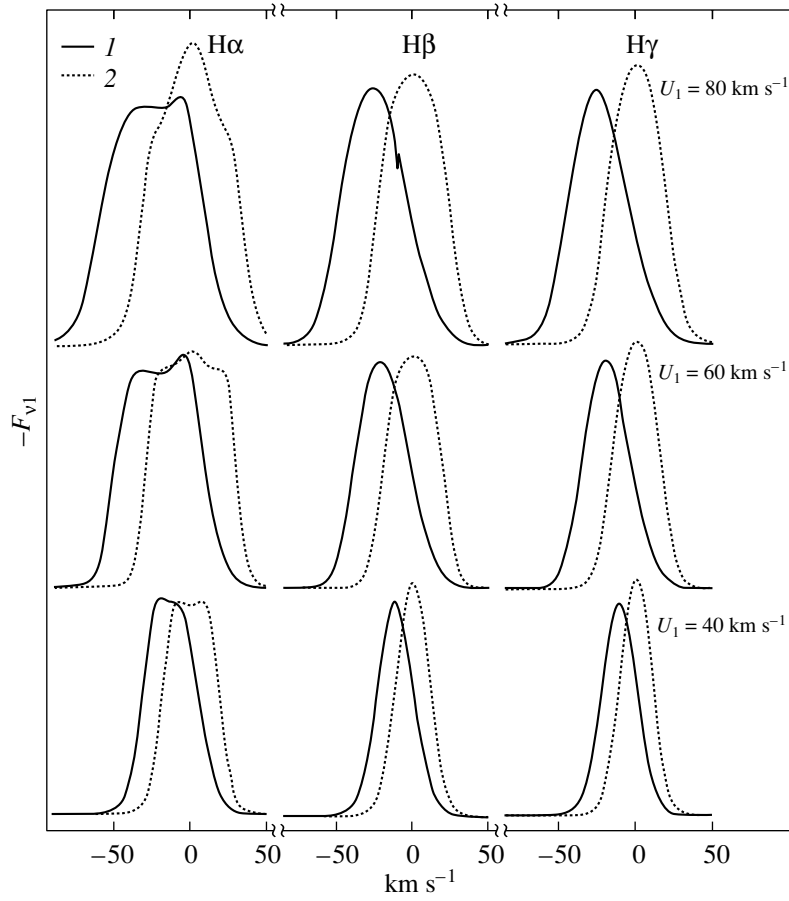
Fig. 4. Normalized emission profiles of the shock wave at Hα, Hβ and Hγ frequencies with allowance made for the Doppler shift (*1*) and in the approximation of a stationary medium (*2*) for $T_1 = 6000$ K and $\rho_1 = 10^{-10}$ g cm^{-3}.

emission profile with increasing shock velocity U_1, which is attributable to an increase in the temperature of atoms T_a^+ behind the shock discontinuity. The solution of the radiative transfer equation with an allowance made for the Doppler shift yields a larger half-width of the emission profile than that given by the solution for a stationary medium; this difference increases with shock amplitude from 3% for $U_1 = 20$ km s^{-1} to 12% for $U_1 = 80$ km s^{-1}. However, the height of the emission profile decreases simultaneously with the increase in the profile width, so the total flux at the line frequencies remains constant, to within $\sim 1\%$.

The small Doppler shift of emission lines, $\Delta U_{obs} \approx \frac{1}{3}U_1$, is attributable not only to the deceleration of the postshock gas flow. Figure 5 shows the spatial distributions of the gas flow velocity in the observer's frame, U_{obs}, for three shock models with amplitudes $U_1 = 40$, 60, and 80 km s^{-1}. The gas compression ratio at the shock discontinuity for these models is $\rho^+/\rho^- = 3.41$, 3.67, and 3.63, respectively, while the gas flow velocity behind the shock discontinuity is

$U_{obs}^+ = 28$, 43, and 57 km s^{-1}, respectively. Note that the decrease of the compression ratio ρ^+/ρ^- with increasing shock velocity at $U_1 > 60$ km s^{-1} results from an increase in the gas temperature in the region of the radiative precursor (see Fadeyev and Gillet (2000) for a discussion of this effect).

Hydrogen atoms behind the shock discontinuity are ionized under the conditions of a significant deviation from a thermal equilibrium. Therefore, the increase in gas heat capacity due to ionization is accompanied by an increase in gas density ρ and deceleration of the gas flow. At low shock velocities, this effect increases in importance with U_1. However, at $U_1 \gtrsim 70$ km s^{-1}, the role of ionization in the deceleration of the gas flow becomes unimportant, because the gas is ionized in the region of the radiative precursor. For example, at a shock velocity $U_1 = 60$ km s^{-1}, the hydrogen ionization degree behind the shock discontinuity increases within $0.18 \leq x_H \leq 0.99$, causing the gas flow velocity to decrease from $U_{obs} = 43$ km s^{-1} to $U_{obs} = 33$ km s^{-1}. For a shock wave with $U_1 = 80$ km s^{-1}, the ionization degree in
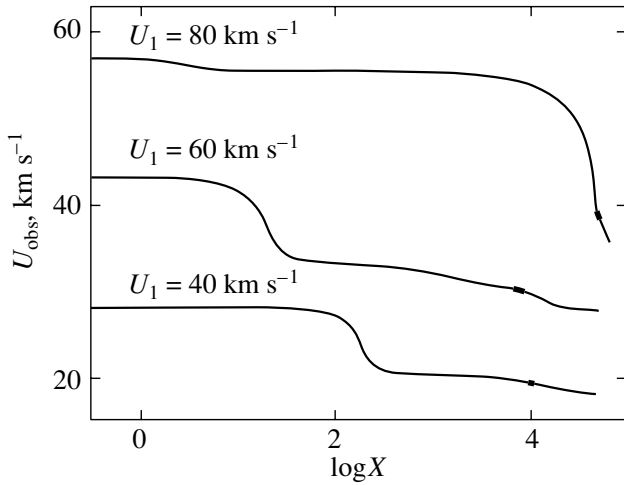
Fig. 5. The postshock gas flow velocity in the observer's reference frame for shock waves with $T_1 = 6000$ K, $\rho_1 = 10^{-10}$ g cm^{-3}, and $U_1 = 40, 60,$ and 80 km s^{-1}. The bold segment of the curve highlights the Balmer line emission region.
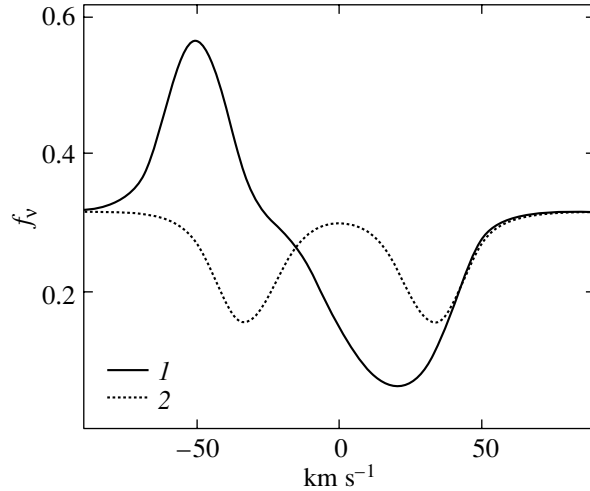
Fig. 6. Variable Eddington factor f_ν at the Hβ frequencies in the formation zone of the Balmer emission from the shock with $T_1 = 6000$ K, $\rho_1 = 10^{-10}$ g cm^{-3}, and $U_1 = 70$ km s^{-1}: (*1*) with allowance made for the Doppler shift and (*2*) in the approximation of a stationary medium.

the radiative precursor is $x_{\rm H} = 0.83$, and the subsequent ionization of the postshock gas causes the gas flow velocity to decrease from $U_{\rm obs} = 57$ to 55 km s^{-1}. The gas flow further decelerates in the atomic hydrogen recombination region, because the recombination lags behind the decrease in gas temperature. Therefore, the gas flow velocity in the Balmer emission region is much lower than the gas velocity immediately behind the shock discontinuity.

The last column of the table gives the gas flow velocities $U_{\rm obs}^*$ in the Balmer line emission region. As follows from the data in the table, at shock velocities 40 km s$^{-1} \leq U_1 \leq 80$ km s^{-1}, the Doppler shift $\Delta U_{\rm obs}$ is approximately one and a half times smaller than $U_{\rm obs}^*$. Interestingly, the solution of the radiative transfer equation for an artificially specified constant velocity field behind the shock discontinuity ($U_{\rm obs} = U_{\rm obs}^+$ at $X > 0$) also yields a ratio $U_{\rm obs}^*/\Delta U_{\rm obs} \approx 1.5$.

The difference between the Doppler shift $\Delta U_{\rm obs}$ and the gas flow velocity $U_{\rm obs}^*$ in the Balmer line emission region is attributable to the anisotropy of the radiation field. To describe the angular dependence of the radiation intensity $I_{\nu\mu}$, it is convenient to use the variable Eddington factor $f_\nu = K_\nu/J_\nu$, where J_ν and K_ν are the zero and second-order angular moments of the radiative transfer equation, respectively. The variable Eddington factor in the Hβ line is plotted against frequency in Fig. 6. For convenience, the frequency shift is given in units of radial velocity. In the continuum and in the red line wing, the Eddington factor is $f_\nu < \frac{1}{3}$, because the optical depth of the

shock wave at these frequencies is small. As a result, the radiation intensity along directions that make an angle with the normal $\mu = \pm 1$ give a larger contribution to the integrals of the angular moments.

CONCLUSIONS

The negligible effect of radiative transfer in spectral lines on the establishment of the structure of a radiative shock wave makes it possible to use the radiative transfer equation in the observer's reference frame and, thus, to circumvent the main difficulty associated with the instability of the solution for the transfer equation in a comoving reference frame. The indicators of the shock velocity U_1 are the Doppler shift $\Delta U_{\rm obs}$ and the half-width $\delta\varphi$ of a emission line, because at a fixed gas density ρ_1, these quantities are proportional to the shock velocity: $\Delta U_{\rm obs} \approx k_{\rm u}U_1$, $\delta\varphi \approx k_\varphi U_1$. At Mach numbers $M_1 \lesssim 10$ and gas densities $\rho_1 = 10^{-10}$ g cm^{-3}, the proportionality factor of the Doppler shift is $k_{\rm u} \approx \frac{1}{3}$ for all lines; the proportionality factor for the half-widths is $k_\varphi \approx 1$, $k_\varphi \approx 0.65$, and $k_\varphi \approx 0.6$ for the Hα, Hβ, and Hγ lines, respectively.

Since the coefficients $k_{\rm u}$ and k_φ presented here were obtained for an unperturbed gas density $\rho_1 = 10^{-10}$ g cm^{-3}, the dependence of these coefficients on gas density is of great importance. Figure 7 shows normalized emission profiles of the Hα, Hβ, and Hγ lines for a shock wave with a velocity $U_1 = 60$ km s^{-1} and unperturbed gas densities $\rho_1 = 10^{-10}$, 3.16×10^{-11}, and 10^{-11} g cm^{-3}. As we see from these plots,
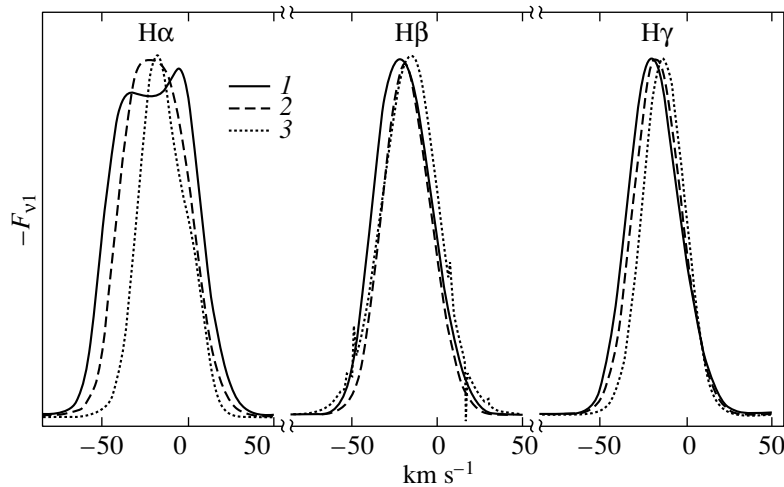
Fig. 7. Normalized emission profiles of the Hα, Hβ, and Hγ lines for a shock wave with a velocity $U_1 = 60$ km s^{-1} and unperturbed gas densities $\rho_1 = (1)\,10^{-10}, (2)\,3.16 \times 10^{-11}$, and $(3)\,10^{-11}$ g cm^{-3}.

the half-width of the Hα profile decreases with decreasing gas density, while the half-widths of the Hβ and Hγ line profiles remain unchanged. The decrease in unperturbed gas density ρ_1 also results in a reduction in the Doppler shift. Unfortunately, calculations of the structure of radiative shock waves in a partially ionized gas require much computational resources, and the determination of the dependence of k_φ and k_u on unperturbed gas density was not our goal. We will present the results of our computations of the shock emission line profiles over a wide range of unperturbed gas densities in our next paper.

REFERENCES

1. H. A. Abt, Astrophys. J. **130**, 824 (1959).
2. H. A. Abt and R. H. Hardie, Astrophys. J. **131**, 155 (1960).
3. K. M. Aggarwal, K. A. Berrington, P. G. Burke, *et al.*, J. Phys. B **24**, 1385 (1991).
4. J. Callaway, At. Data Nucl. Data Tables **57**, 9 (1994).
5. Yu. A. Fadeev, Astron. Zh. **78**, 421 (2001) [Astron. Rep. **45**, 361 (2001)].
6. Yu. A. Fadeyev and D. Gillet, Astron. Astrophys. **333**, 687 (1998).
7. Yu. A. Fadeyev and D. Gillet, Astron. Astrophys. **354**, 349 (2000).
8. Yu. A. Fadeyev and D. Gillet, Astron. Astrophys. **368**, 901 (2001).
9. Yu. A. Fadeyev, H. LeCoroller, and D. Gillet, Astron. Astrophys. **392**, 735 (2002).
10. V. G. Gorbatskiĭ, Astron. Zh. **38**, 256 (1961).
11. *Modern Numerical Methods for Ordinary Differential Equations,* Ed. by G. Hall and J. M. Watt (Clarendon, Oxford, 1976; Mir, Moscow, 1979).
12. R. P. Kraft, D. C. Camp, and W. T. Hughes, Astrophys. J. **130**, 90 (1959).
13. D. J. Lennon, P. J. F. Brown, P. L. Dufton, *et al.*, Mon. Not. R. Astron. Soc. **222**, 719 (1986).
14. D. Michalas, *Stellar Atmospheres* (Freeman, San Francisco, 1978; Mir, Moscow, 1982).
15. D. Mihalas, Astrophys. J. **238**, 1042 (1980).
16. D. Mihalas, P. B. Kunasz, and D. G. Hummer, Astrophys. J. **202**, 465 (1975).
17. K. Radhakrishnan and A. C. Hindmarsh, Technical Report No. 113 855 (Lawrence Livermore National Laboratory, 1993).
18. G. B. Rybicki and D. G. Hummer, Astron. Astrophys. **245**, 171 (1991).
19. T. T. Scholz, H. R. J. Walters, P. J. Burke, and M. P. Scott, Mon. Not. R. Astron. Soc. **242**, 692 (1990).
20. G. Wallerstein, Astrophys. J. **130**, 560 (1959).

Translated by A. Dambis